UNIVERSITY OF OKLAHOMA

GRADUATE COLLEGE

HIGH-FIDELITY MODELING AND IMPACT FOOTPRINT PREDICTION FOR VEHICLE BREAKUP ANALYSIS

A Dissertation

SUBMITTED TO THE GRADUATE FACULTY

in partial fulfillment of the requirements for the

degree of

Doctor of Philosophy

By

Lisa Ling
Norman, Oklahoma
2005

Downloaded from SHAREOK. Persistent Handle URL: https://hdl.handle.net/11244/910

UMI Number: 3179077



UMI Microform 3179077

Copyright 2006 by ProQuest Information and Learning Company.
All rights reserved. This microform edition is protected against
unauthorized copying under Title 17, United States Code.

ProQuest Information and Learning Company
300 North Zeeb Road
P.O. Box 1346
Ann Arbor, MI 48106-1346

HIGH-FIDELITY MODELING AND IMPACT FOOTPRINT PREDICTION FOR VEHICLE BREAKUP ANALYSIS

A DISSERTATION APPROVED FOR THE

SCHOOL OF AEROSPACE AND MECHANICAL ENGINEERING

BY

_____

Dr. Dan Tuckness

_____

Dr. Yunjun Xu

_____

Dr. David Miller

_____

Dr. Harold Stalford

_____

Dr. Sesh Commuri

© Copyright by Lisa Ling 2005
All Rights Reserved.

Acknowledgments

I am very grateful to my mentors, Dr. Angus McRonald and Peter Jaffe, for giving me the opportunity to learn under their direction and guidance. With great patience, they have allowed me to delve into their wealth of knowledge and experience for my benefit; it was like having unlimited access to goldmines. I would also like to thank my bosses, Dr. Ahmed Salama and Dr. Larry Reinhart, for giving me the opportunity to work on vehicle breakup analysis for various projects and for supporting my pursuit in the Ph.D. degree. Their understanding and constant encouragement have made my research work an enjoyable experience. I am also thankful to have the support and employment from the Jet Propulsion Laboratory / California Institute of Technology (JPL/CIT).

I am very appreciative of my advisor at the University of Oklahoma, Dr. Dan Tuckness, for his guidance and attention throughout my Ph.D. program which began at the University of Texas in Arlington. I would also like to thank my committee members for reviewing my research work carefully and ensuring a level of quality.

Last but not least, I would like to thank my family for being so wonderfully patient and accommodating of my irregular work schedule during the last few months as a result of my attempt to finish the dissertation. Their support and pride in my achievements make all the hard work worthwhile, and I cannot ask for a better family.

Table of Contents

1. INTRODUCTION 1

2. DEVELOPMENT OF NEW DYNAMICS MODELING AND CAPABILITIES 8

2.1 COORDINATE SYSTEMS 8
2.2 3-DOF TRAJECTORY PROPAGATION 9
2.3 NON-ARBITRARY ENTRY CONDITIONS IN V-GAMMA MAP 12
2.3.1 Applications of V-Gamma Map 12
2.3.2 Modeling of Inertial-Fixed Thrust 15
2.3.3 Outcome of Steady Misaligned Burn 16
2.3.4 Entry Condition for Delayed Reentry 17
2.3.5 Validation of Non-Arbitrary Entry Conditions 21
2.4 PANEL CODE FOR HYPERSONIC AERODYNAMIC COEFFICIENTS 24
2.4.1 Calculation of Hypersonic Aerodynamic Coefficients 26
2.4.2 Modeling of Triangular Panels 26
2.4.3 Adaptation to Axi-Symmetric Body 30
2.4.4 Validation of Panel Code 31
2.4.5 Test Case 1: Sharp-Nose, Circular Cone 32
2.4.6 Test Case 2: A Hypersonic Vehicle 33
2.5 CALCULATIONS OF FAILURE CRITERIA 37
2.5.1 Aeroshell 38
2.5.2 Thermal Blanket 39
2.5.3 Solar Array 39
2.5.4 Propellant Tanks 40
2.5.4.1 Burst Pressure 41
2.5.4.2 Burnout Flux 42
2.6 SENSITIVITY ANALYSIS 43
2.7 FOOTPRINT DETERMINATION 45
2.8 MODELING OF LOCAL WINDS 49

3. RESULTS OF NEW DYNAMICS MODELING AND CAPABILITIES 52

3.1 CASE STUDY: MARS EXPLORATION ROVER MISSION 53
3.2 PREDICTIONS OF IMPACT POINTS IN SUBORBITAL REENTRIES 54
3.3 PREDICTION OF IMPACT POINTS IN OUT-OF-ORBIT REENTRIES 57
3.3.1 V-Gamma Map 58
3.3.2 Circular Orbit Decay 59
3.3.3 Delayed Elliptic 60
3.3.4 Powered Reentry 61
3.4 SENSITIVITY ANALYSIS AND FOOTPRINT CALCULATION 61
3.5 PREDICTION OF IMPACT FOOTPRINT WITH EFFECTS OF WINDS 63

4. CONCLUSIONS AND FUTURE WORK 65

APPENDIX A. VEHICLE BREAKUP ANALYSIS FOR AEROSPACE NUCLEAR SAFETY 68

APPENDIX B. VEHICLE BREAKUP ANALYSIS FOR PLANETARY PROTECTION 70

APPENDIX C. VEHICLE BREAKUP ANALYSIS FOR DEBRIS ANALYSIS 72

C.1 History of Reentries 72
C.2 Debris Analysis in the Global Scene 75

APPENDIX D. VEHICLE BREAKUP ANALYSIS WITH ENGINEERING JUDGMENT 77

D.1 Determine Failure Scenarios from Mission Timeline and Launch Trajectory 77
D.2 Set Assumptions to Bound Failure Scenarios 81
D.3 Determine Spacecraft Configuration and Select Thermal/Force Nodes 84
D.4 Collect Information on Node Physical and Material Properties 86
D.5 Make Assumptions for Missing Data Based on Engineering Judgment 88
D.6 Set Exposure Factors 89
D.7 Determine Failure Criteria 90
D.8 Determine Expected Sequence of Failure 93
D.9 Determine Ballistic Coefficients of Various Spacecraft Configurations 95
D.10 Predict Vehicle Breakup and Outcome of Nuclear Component 96
D.11 Perform Sensitivity Analysis and Calculate Impact Footprint 98

APPENDIX E. COORDINATE TRANSFORMATION MATRICES 100

APPENDIX F. EQUATIONS OF MOTION FOR 3-DOF TRAJECTORY PROPAGATION 106

F.1 Air-Relative Motion 106
F.2 Inertial Motion 108
F.3 Relationship Between Inertial and Relative Vectors 110
F.4 Dynamics 111
F.5 Equations of Motion 112
F.6 Transformation of Vehicle State to Rotating Frame 113
F.7 Inertial State to Air-Relative State in Spherical Coordinates 114
F.8 Air-Relative State to Inertial State in Spherical Coordinates 115
F.9 Inertial State in Cartesian Coordinates to Air-Relative State in Spherical Coordinates 116

APPENDIX G. MER DATA FOR VEHICLE BREAKUP ANALYSIS 118

G.1 Task Description 118
G.2 Launch Vehicle and Spacecraft Configuration 118
G.3 Mission Timeline 120
G.4 Assumptions and Considerations 121
G.5 Reentry Scenarios 123
G.6 Thermal Nodes 125
G.6.1 Cruise Stage Thermal Nodes 125

G.6.2 Launch Vehicle and Entry Vehicle Thermal Nodes 128
G.7 FAILURE CRITERIA 130
G.7.1 Failure Criteria for Cruise Stage Nodes 131
G.7.2 Failure Criteria for Aeroshell 131
G.7.3 Failure Criteria for Entry Spacecraft 132
G.8 EXPOSURE FACTORS 133
G.8.1 Suborbital Reentry Exposure Factors 133
G.8.2 Out-of-Orbit Reentry Exposure Factors 134
G.9 EXPECTED SEQUENCE OF FAILURES AND VEHICLE PROPERTIES UPDATES 135

APPENDIX H. REFERENCES 139

APPENDIX I. ACRONYMS 147

APPENDIX J. SYMBOLS 151

List of Tables

TABLE 1. NEW FUNCTIONS AND IMPROVEMENTS IN ANALYSIS TOOL 6
TABLE 2. BURN SEQUENCE FOR TEST CASE 21
TABLE 3. COMPARISON OF V, GAMMA, AND TIME AT ENTRY OR END OF LAST BURN 22
TABLE 4. COMPARISON OF ENTRY TIME, LATITUDE, LONGITUDE, AND AZIMUTH FOR DELAYED ENTRY 23
TABLE 5. COMPARISON OF ENTRY ANGLE-OF-ATTACK FOR POWERED ENTRY 24
TABLE 6. ROOT MEAN SQUARES OF DIFFERENCES IN AERODYNAMIC COEFFICIENTS 37
TABLE 7. PARAMETRIC BIASES IN SENSITIVITY ANALYSIS 43
TABLE 8. IMPACT POINTS FROM SENSITIVITY ANALYSIS 44
TABLE 9. CONFIDENCE INTERVALS 47
TABLE 10. EXAMPLE WIND PROFILE FROM NOAA WEBSITE 63
TABLE 11. INADVERTENT EARTH REENTRIES OF NUCLEAR POWERED PAYLOADS 68
TABLE 12. MISSIONS WITH UNSUCCESSFUL MARS EDL 70
TABLE 13. PAST REENTRIES OF SATELLITES 74
TABLE 14. THRUST CALCULATION 111
TABLE 15. MISSION TIMELINES 121
TABLE 16. PROPERTIES OF CRUISE STAGE THERMAL NODES 126
TABLE 17. LAUNCH VEHICLE AND ENTRY VEHICLE THERMAL NODES 128
TABLE 18. FAILURE INTEGRATED HEATING FOR ENTRY VEHICLE IN SUBORBITAL REENTRY 132
TABLE 19. FAILURE INTEGRATED HEATING FOR ENTRY AND LAUNCH VEHICLES IN OUT-OF-ORBIT REENTRY 133
TABLE 20. EXPOSURE FACTORS FOR SUBORBITAL REENTRIES 134
TABLE 21. EXPOSURE FACTORS FOR OUT-OF-ORBIT REENTRIES 134
TABLE 22. EXPECTED SEQUENCE OF FAILURES AND VEHICLE PROPERTIES UPDATES IN SUBORBITAL REENTRY 135
TABLE 23. NODE MASSES FOR UPDATES 136
TABLE 24. EXPECTED SEQUENCE OF FAILURES AND VEHICLE PROPERTIES UPDATES IN OUT-OF-ORBIT REENTRY AT ENTRY ANGLE-OF-ATTACK OF 0º 137
TABLE 25. EXPECTED SEQUENCE OF FAILURES AND VEHICLE PROPERTIES UPDATES IN OUT-OF-ORBIT REENTRY AT ENTRY ANGLE-OF-ATTACK OF 90º 137
TABLE 26. EXPECTED SEQUENCE OF FAILURES AND VEHICLE PROPERTIES UPDATES IN OUT-OF-ORBIT REENTRY AT ENTRY ANGLE-OF-ATTACK OF 180º 138

List of Illustrations

FIGURE 1. PROCESS OF PERFORMING VEHICLE BREAKUP ANALYSIS 7
FIGURE 2. COMPARISON OF (A) ALTITUDE, (B) RELATIVE VELOCITY, AND (C) RELATIVE FLIGHT PATH ANGLE VS TIME FOR VALIDATION OF TRAJECTORY PROPAGATION 11
FIGURE 3. EXAMPLE OF V-GAMMA MAP 14
FIGURE 4. DEFINITIONS OF VARIABLES AND COORDINATE SYSTEMS 27
FIGURE 5. COMPARISON OF C_N IN SHARP-NOSE, CIRCULAR CONE TEST CASE 32
FIGURE 6. COMPARISON OF C_A IN SHARP-NOSE, CIRCULAR CONE TEST CASE 33
FIGURE 7. COMPARISON OF C_Y IN SHARP-NOSE, CIRCULAR CONE TEST CASE 33
FIGURE 8. HYPERSONIC VEHICLE 34
FIGURE 9. COMPARISONS OF (A) C_N, (B) C_M, AND (C) C_A FOR HYPERSONIC VEHICLE WITH 0º FLAP DEFLECTION ANGLE 35
FIGURE 10. COMPARISONS OF C_N AND C_A FOR HYPERSONIC VEHICLE WITH 10º FLAP DEFLECTION ANGLE 36
FIGURE 11. COMPARISON OF C_A FOR HYPERSONIC VEHICLE WITH 20º FLAP DEFLECTION ANGLE 36
FIGURE 12. COMPARISON OF C_A FOR HYPERSONIC VEHICLE WITH 30º FLAP DEFLECTION ANGLE 36
FIGURE 13. COORDINATE SYSTEM FOR FOOTPRINT DETERMINATION 45
FIGURE 14. 3-SIGMA FOOTPRINT 49
FIGURE 15. RELATIVE, WIND, AND AERODYNAMIC VELOCITY VECTORS 51
FIGURE 16. INTEGRATED HEATING VS TIME OF FTS ACTIVATION IN SUBORBITAL REENTRIES 55
FIGURE 17. (A) VEHICLE ALTITUDE WITH SEQUENCE OF NODE FAILURES, (B) AIR-RELATIVE SPEED, AND (C) GROUND TRACK AT FTS ACTIVATION OF 571.073 SEC 56
FIGURE 18. INDEPENDENT VEHICLE BREAKUP ANALYSIS USING LEGACY SOFTWARE 57
FIGURE 19: (A) V-GAMMA MAP FOR THE MER-A MISSION, (B) RELATIVE PROBABILITIES FOR THE MER-A MISSION 59
FIGURE 20. 3-σ IMPACT FOOTPRINT 63
FIGURE 21. GEOSYNCHRONOUS VIEW OF OBJECT POPULATION 72
FIGURE 22. (A) DELTA 2 SECOND STAGE STAINLESS STEEL PROPELLANT TANK LANDED IN GEORGETOWN, TX, (B) DELTA 2 THIRD STAGE TITANIUM MOTOR CASING LANDED IN SAUDI ARABIA 73
FIGURE 23. COMBINED FAILURE CRITERIA 93
FIGURE 24. ROTATING AND SPHERICAL NAVIGATION COORDINATE SYSTEMS 100
FIGURE 25. ANGLE-OF-ATTACK, SIDESLIP, AND BANK 102
FIGURE 26. EULER ANGLES: ROLL, PITCH, AND YAW 103
FIGURE 27. ORBITAL ELEMENTS 104
FIGURE 28. DEFINITIONS OF LONGITUDE 104
FIGURE 29. AZIMUTH AND FLIGHT PATH ANGLE 113
FIGURE 30. DELTA II 7925 LAUNCH VEHICLE CONFIGURATION 119
FIGURE 31. MER SPACECRAFT CONFIGURATION 120
FIGURE 32. CRUISE STAGE THERMAL NODES 125

FIGURE 33. (A) AEROSHELL AND (B) LANDER AND ROVER THERMAL NODES IN SUBORBITAL REENTRY 129
FIGURE 34. ENTRY AND LAUNCH VEHICLE THERMAL NODES IN OUT-OF-ORBIT REENTRY 130

ABSTRACT

For decades, vehicle breakup analysis had been performed for space missions that used nuclear heater or power units in order to assess aerospace nuclear safety for potential launch failures leading to inadvertent atmospheric reentry. Such pre-launch risk analysis is imperative to assess possible environmental impacts, obtain launch approval, and for launch contingency planning. In order to accurately perform a vehicle breakup analysis, the analysis tool should include a trajectory propagation algorithm coupled with thermal and structural analyses and influences. Since such a software tool was not available commercially or in the public domain, a basic analysis tool was developed by Dr. Angus McRonald prior to this study. This legacy software consisted of low-fidelity modeling and had the capability to predict vehicle breakup, but did not predict the surface impact point of the nuclear component.

Thus the main thrust of this study was to develop and verify the additional dynamics modeling and capabilities for the analysis tool with the objectives to (1) have the capability to predict impact point and footprint, (2) increase the fidelity in the prediction of vehicle breakup, and (3) reduce the effort and time required to complete an analysis. The new functions developed for predicting the impact point and footprint included 3-degrees-of-freedom trajectory propagation, the generation of non-arbitrary entry conditions, sensitivity analysis, and the calculation of impact footprint. The functions to increase the fidelity in the prediction of vehicle breakup included a panel code to calculate the hypersonic aerodynamic coefficients for an arbitrary-shaped body and the modeling of local winds. The function to reduce the effort and time required to complete an analysis included the calculation of node failure criteria. The derivation and

development of these new functions are presented in this dissertation, and examples are given to demonstrate the new capabilities and the improvements made, with comparisons between the results obtained from the upgraded analysis tool and the legacy software wherever applicable.

1. Introduction

For decades, vehicle breakup analysis had been performed for space missions that used nuclear heater or power units to assess aerospace nuclear safety in the event of a launch failure leading to inadvertent atmospheric reentry (see Appendix A). Such pre-launch risk analysis is imperative to assess environmental impact, obtain launch approval, and for launch contingency planning. Work devoted to this area had been ongoing since 1959 [1] and had been well-documented [2-13]. In more recent years, vehicle breakup analysis has also been on the agenda of planetary exploration missions to address planetary protection issues, e.g. contamination of Martian soil by Earth microorganisms (see Appendix B). Another application of vehicle breakup analysis is in debris analysis (see Appendix C), where considerable attention was gained due to the 2003 Shuttle Columbia accident. Each area of application of vehicle breakup analysis has slightly different objectives, thus requiring different capabilities in the analysis tools. In this document, the research work presented is applicable to the vehicle breakup analysis performed for aerospace nuclear safety, specifically those conducted at the Jet Propulsion Laboratory (JPL) for launch approval.

Vehicle breakup analyses at JPL are performed at the request of the project (Aerospace Nuclear Safety Engineer) in support of the risk assessments undertaken by the Department of Energy for NASA spacecraft that are planning to use radioisotopes for onboard electrical power (e.g., a Radioisotope Thermoelectric Generator, RTG) or heat (e.g., a Light Weight Radioisotope Heater Unit, LWRHU). The risk assessment early in the project is provided for the Environmental Impact Statement (EIS) completed by NASA. The final risk assessment, completed later in the project for the DOE Safety

Analysis Report (SAR), is a critical element in the process of getting launch approval from the President of the United States. The vehicle breakup analysis for the final risk assessment is submitted to the Interagency Nuclear Safety Review Panel (INSRP) for review. INSRP consists of representatives from NASA, the Department of Defense (the Air Force), the Department of Energy, and the Environmental Protection Agency. Reference [4] gives a complete roadmap for obtaining launch approval.

Vehicle breakup analysis performed for risk assessment and hazard evaluation provides an estimate of both the vehicle breakup characteristics and the impact point of the General Purpose Heat Source (GPHS) modules carried inside the RTG or the LWRHU for various failure scenarios during launch prior to Earth escape. Given the nominal ascent trajectory and burn sequence while in the parking orbit, various failure scenarios can be analyzed. Typically in a failure during ascent, the spacecraft does not have enough energy to be captured into orbit and will fall back in a suborbital reentry. Failures occurring during most of the ascent in a launch from Cape Canaveral, Florida, to achieve posigrade orbit will result in impact in the Atlantic Ocean. However, for a few seconds late in the ascent prior to achieving orbit, a failure leading to suborbital reentry may result in impact on Africa. After capturing into orbit, a failure occurring while in the parking orbit such as a steady misaligned burn (SMB, where the vehicle maintains a constant wrong heading in space during the burn and the intermediate staging), an incomplete burn, or no burn may lead to out-of-orbit reentry. An example of a failure scenario is the failure to ignite which would eventually lead to reentry due to orbit decay. Another example is an SMB which would propel the spacecraft into a specific orbit depending on the thrust misalignment, with an out-of-orbit reentry as a possible outcome

of the SMB. Given the onboard fuel, the envelope of reentry conditions consisting of entry speeds (V) and flight path angles (Gamma) can be determined and plotted on a V-Gamma map.

The GPHS module and LWRHU are designed to survive harsh environments, whereas their responses to these environments as part the spacecraft become uncertain. It is thus highly desirable for the GPHS module or LWRHU to be released from the spacecraft during an inadvertent Earth reentry. Therefore, the main objectives of the vehicle breakup analysis for launch approval and contingency planning are to (1) predict vehicle breakup and release of the GPHS modules from the RTG and/or the LWRHU, (2) predict nominal impact point and impact conditions of the GPHS modules and/or the LWRHU, or the vehicle component containing them, and (3) determine uncertainty in impact point prediction in terms of impact footprint. Past missions where vehicle breakup analyses were performed for launch approval include Voyager [14], Galileo, Ulysses [15], Cassini, and Mars Exploration Rover (MER). Future missions where vehicle breakup analyses could be required include Mars Science Laboratory (MSL) and missions to Europa or other outer planets or their moons. Examples of JPL internal documents generated for previous vehicle breakup analyses can be found in Ref. [16-28].

The basic functions required to perform vehicle breakup analysis include trajectory simulation, coupled with thermal and structural analyses and influences. Many high-fidelity analysis tools are available in the public domain or on the commercial market for performing the trajectory simulation, thermal analysis, and structural analysis as separate functions. Examples of software tools include the Program to Optimize Simulated Trajectories (POST) [30] and Atmospheric-Entry, Powered-Landing simulator

(AEPL) [31] for trajectory simulation; Systems Improved Numerical Differencing Analyzer/Gaski (SINDA/G) [32] and Langley Aerothermodynamic Upwind Relaxation Algorithm (LAURA) [33] for thermal analysis; and NASA Structural Analysis computer program (NASTRAN) [34], ANSYS [35], and Integrated Modeling of Optical Systems (IMOS) [36] for structural analysis. However, there was no known, accessible analysis tool which combined the functions for trajectory propagation, thermal analysis, and structural analysis to meet the specific needs of vehicle breakup analysis for applications in aerospace nuclear safety. Thus, a basic analysis tool was developed by Dr. Angus McRonald prior to this study. This legacy software consisted of low-fidelity modeling and was used to perform vehicle breakup analysis and predict the outcome of the RTG/LWRHU. However, it did not predict the surface impact point and footprint of the RTG/LWRHU or the component carrying the RTG/LWRHU, and such predictions would have been provided by another organization, e.g. Air Force Space Command. The legacy software propagated the trajectory by integrating the coupled differential equations for the spacecraft's planar translational motion, with the option for a ballistic fall back (zero thrust) or a constant body-fixed thrust with decreasing fuel mass; node temperatures are calculated by modeling the applicable convective, conductive, and radiative heat transfer; and common g-load is calculated based on non-gravitational, perturbing acceleration. Two pre-processors were developed: "V-Gamma Map" calculates the envelope of out-of-orbit reentry speeds and flight path angles resulting from steady misaligned burns while in the parking orbit; "Newtonian Code" (a panel code) calculates the aerodynamic coefficients of an axi-symmetric body in hypersonic flow.

The objectives of this study are to develop and verify new dynamics modeling and capabilities for the analysis tool to (1) have the capability to predict impact point and footprint, (2) increase the fidelity in the prediction of vehicle breakup, and (3) reduce the effort and time required to complete an analysis. The new functions needed to predict the impact point and footprint included 3-degrees-of-freedom (3-DOF) trajectory propagation, the generation of non-arbitrary entry conditions for the V-Gamma map, sensitivity analysis, and the calculation of impact footprint. The functions to increase the fidelity in the prediction of vehicle breakup included a panel code to calculate the hypersonic aerodynamic coefficients for an arbitrary-shaped body and the modeling of local winds. The function to reduce the effort and time required to complete an analysis included the calculation of node failure criteria. A summary of the new functions and the resulting improvements is given in Table 1. Note that the functions for predicting the impact point and footprint also aid in reducing the effort and time required to complete an analysis and allow rapid response during an actual launch contingency since the need for another organization to provide this capability would no longer be required. The synthesis of these new development and capabilities to produce a powerful analysis tool is an important new contribution to the vehicle breakup analysis performed for aerospace nuclear safety. This dissertation presents the development and verification of the new functions discussed above, and examples are given using the vehicle breakup analysis performed for the Mars Exploration Rover (MER) mission to demonstrate the improvements made. Comparisons between the results obtained from the upgraded analysis tool and the legacy software are also given wherever applicable.

Table 1. New Functions and Improvements in Analysis Tool

Improvement	Functions		Comments
	Legacy Software	Upgraded Tool	
Capability to predict impact point and footprint	2-DOF, planar translational motion	3-DOF translational motion	2-DOF simulation yields only altitude and range for position. 3-DOF simulation is needed to produce position vector for impact point prediction.
	V-γ map produces entry V and γ	V-γ map produces non-arbitrary entry condition	V and γ together yield only an arbitrary point in the air, thus can only predict range relative to the arbitrary entry point. Non-arbitrary entry point is needed for propagation to predict a specific impact point.
	N/A	Sensitivity analysis	Sensitivity analysis needed to produce dispersed impact points for the calculation of footprint.
	N/A	Calculation of footprint	Produces impact footprint based on sensitivity analysis.
Increase fidelity in predictions from breakup analysis	Panel code for axi-symmetric body	Panel code for arbitrary-shaped body	Vehicle configurations most likely not axi-symmetric as components break up during reentry. Accuracy in aerodynamics is compromised if vehicle can only be modeled as axi-symmetric.
	N/A	Modeling of local winds	Local winds may cause dispersion in impact point and thus enhance accuracy of footprint.
Reduce effort and time required to complete an analysis	N/A	Calculation of node failure criteria	Calculation of node failure criteria based on integrated heating was done by hand before implementation into upgraded tool, thus time-consuming.

The process of performing vehicle breakup analysis using the upgraded system is described in Figure 1 for a single-case run. The general methodology in performing vehicle breakup analysis does not change with the implementation of the new dynamics modeling and capabilities, although the results from the analysis become more complete,

more accurate, and are obtained in shorter amount of time. A detailed discussion on the process of performing vehicle breakup analysis is given in Appendix D.

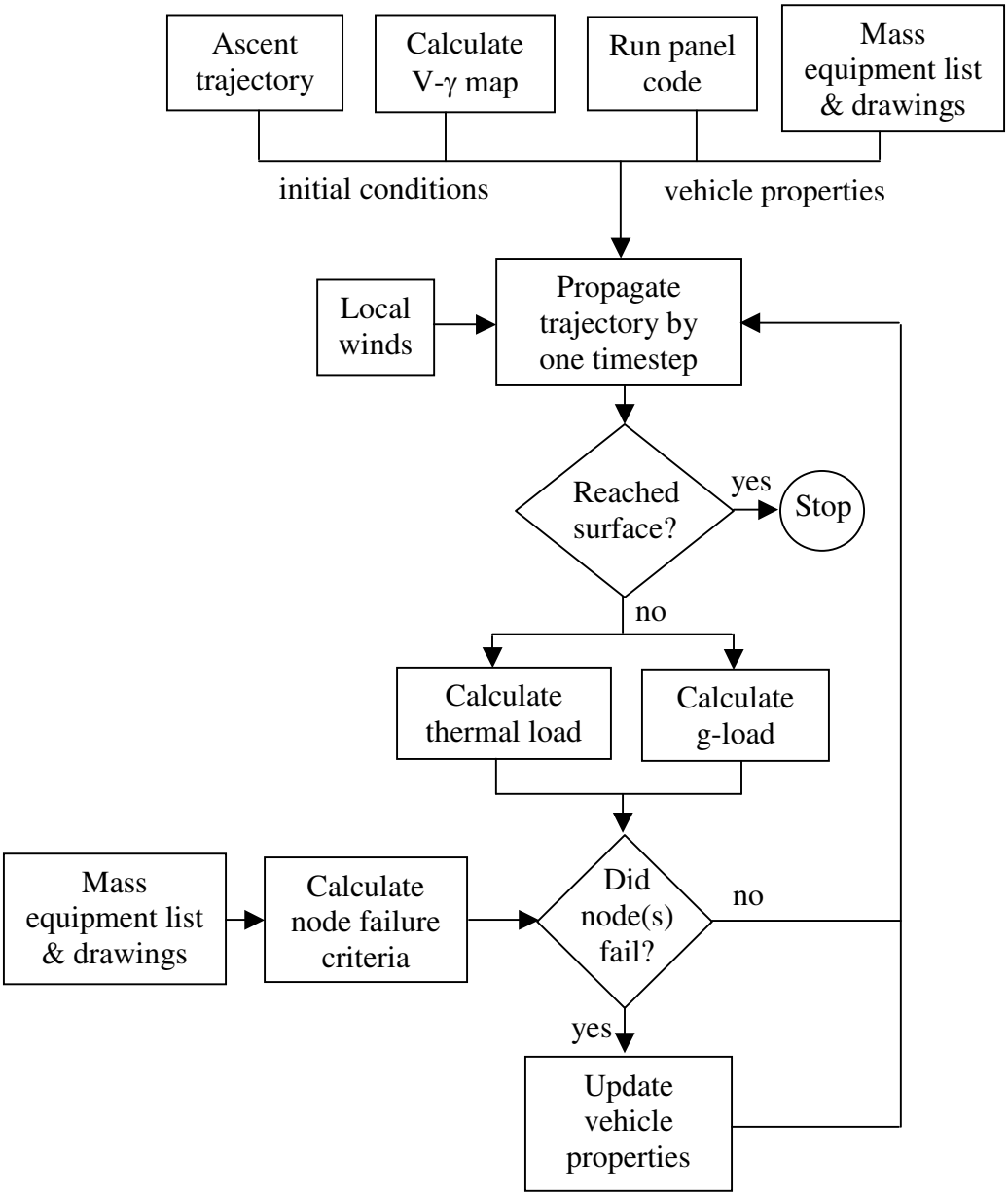


Figure 1. Process of Performing Vehicle Breakup Analysis

2. Development of New Dynamics Modeling and Capabilities

The new dynamics modeling and capabilities for the analysis tool are listed below and are discussed in the following sections.

- 3-DOF trajectory propagation
- Non-arbitrary entry conditions in V-Gamma map
- Panel code for arbitrary-shaped body
- Modeling of local winds
- Sensitivity analysis
- Calculation of impact footprint
- Node failure criteria.

2.1 Coordinate Systems

All coordinate systems employed are defined by a set of three ortho-normal basis functions. In the following sections, the symbol $\vec{x}_a^{\,b}$ denotes a vector x as observed in the a-frame and projected onto b-frame coordinates (referenced to a-frame and expanded in terms of b-frame base vectors). The definitions of the various reference frames are given below:

1) Inertial frame ($\hat{e}_x^I$, $\hat{e}_y^I$, $\hat{e}_z^I$): non-rotating, geocentric frame. The z-axis is along the Earth axis of rotation and points towards the North Pole. The x-z plane contains the spacecraft at trajectory initiation (t=0).

2) Rotating frame ($\hat{e}_x^R$, $\hat{e}_y^R$, $\hat{e}_z^R$): rotating, geocentric frame. The axes of the rotating and inertial frames are identical at simulation initialization. The rotating frame then drifts from the inertial frame at Earth's angular rate.

3) Navigation or REN frame ($\hat{e}_r^n$, $\hat{e}_\theta^n$, $\hat{e}_\phi^n$): moving frame centered at the spacecraft center-of-gravity (c.g.). The r, θ, and ϕ axes are radial, due East, and due North tangent to the local meridian, respectively. The θ and ϕ axes lie in the local horizontal plane, and the r-axis is upwards along the local vertical normal to the geoid.

4) Velocity frame ($\hat{e}_x^v$, $\hat{e}_y^v$, $\hat{e}_z^v$): moving frame centered at the spacecraft c.g. Also known as the stability axes. The x-axis is along the spacecraft air-relative velocity vector. The y-axis remains horizontal locally, and the z-axis points downwards.

5) Body frame ($\hat{e}_x^b$, $\hat{e}_y^b$, $\hat{e}_z^b$): moving frame centered at the spacecraft c.g. A special case is the principal axes where the moment of inertia tensor is a diagonal matrix. The x-axis is along the axis of aerodynamic symmetry (zero lift line) and points towards the nose. The z-axis points down in the plane of geometric symmetry.

6) Orbit frame ($\hat{e}_x^o, \hat{e}_y^o, \hat{e}_z^o$): time-dependent, geocentric frame. The x-axis extends through the perigee, and the z-axis is along the angular momentum vector normal to the orbit plane.

The matrices for transforming between the various reference frames are given in Appendix E.

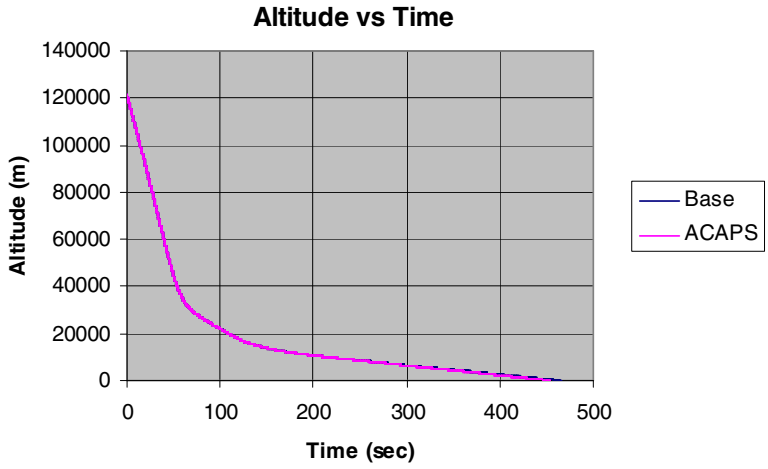
2.2 3-DOF Trajectory Propagation

The derivation of the kinematics and dynamics to formulate the equations of motion for 3-DOF trajectory propagation is given in Appendix F. Validation of the propagator is performed by comparing the trajectories generated by the upgraded analysis

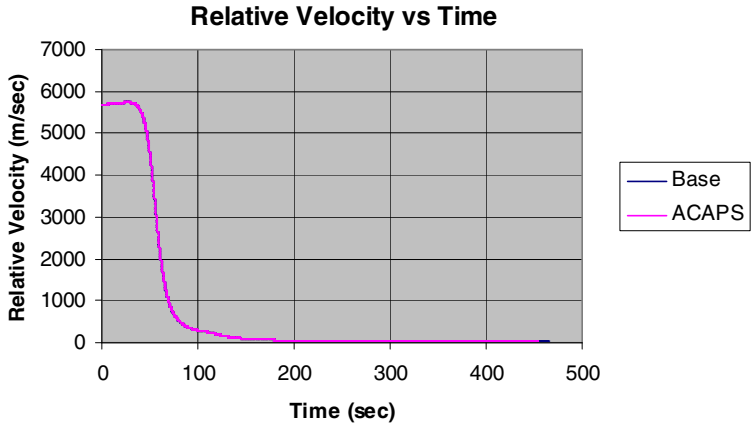
tool and ACAPS, a formal software used for aerocapture studies [37]. The initial conditions and vehicle characteristics for the test case were:

Altitude	= 121.86 km
Relative speed	= 5681.27 m/sec
Relative flight path angle	= -14.97 deg
Latitude	= -41.64 deg
Longitude	= 270.73 deg
Azimuth	= 95.19 deg
Mass	= 1883.0 kg
C_D	= 1.55
A_{ref}	= 11.04 m^2

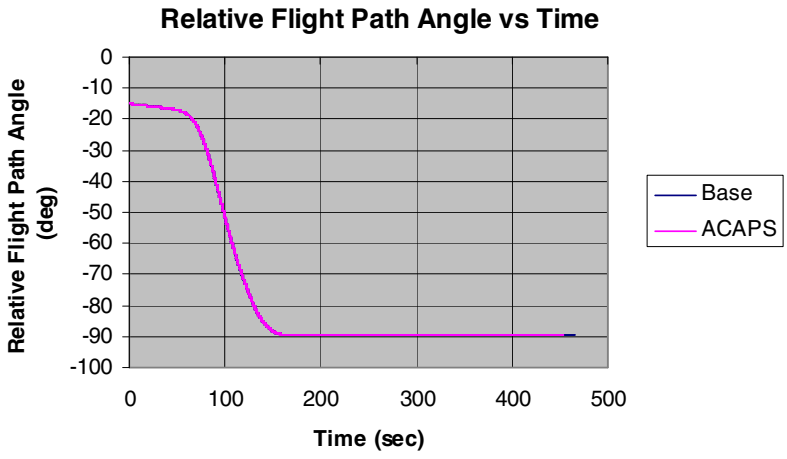
The comparisons of the time histories of the altitude, relative velocity, and relative flight path angle are given in Figure 2. Note that "Base" in the plots denotes the upgraded analysis tool.



(a)



(b)



(c)

Figure 2. Comparison of (a) Altitude, (b) Relative Velocity, and (c) Relative Flight Path Angle vs Time for Validation of Trajectory Propagation

2.3 Non-Arbitrary Entry Conditions in V-Gamma Map

To determine the initial entry condition for trajectory propagation in an out-of-orbit reentry resulting from an SMB while in the parking orbit, the legacy software generates the speed and flight path angle at the entry altitude, without the calculation of the entry latitude, longitude, and azimuth. This results in an arbitrary entry condition, thus only ground track relative to the arbitrary entry point can be predicted. In order to predict potentialimpact point s of the radioisotope power system, e.g. in terms of latitude and longitude, a non-arbitrary entry condition is needed. To attain this added capability, the modeling of inertial-fixed thrust in an SMB and the determination of a non-arbitrary entry condition in an out-of-orbit reentry were developed.

2.3.1 Applications of V-Gamma Map

A spectrum of reentry conditions consisting of entry speeds, V, and flight path angles, Gamma, can be derived from the assumptions of (1) SMB in the execution of the parking orbit burn sequence, and (2) an otherwise nominal, time-delayed sequence of burns while in the parking orbit. The possible outcomes of the SMB consist of the following categories [39]:

1) Hyperbolic escape (HE): The spacecraft has reached hyperbolic speed and is not on a path that enters the atmosphere.

2) Orbit decay reentry (DEL): The perigee of the final orbit is above the atmosphere, so that reentry occurs after a period of orbit decay.

3) Powered reentry (PWE): The reentry occurs while the burns are in progress, and the spacecraft has not separated from the launch vehicle.

4) Prompt reentry (ELP): The burns have finished prior to reentry but the vehicle is then on a downward path approaching a perigee within the atmosphere.

5) Delayed reentry (ELD): The vehicle is on an upward path at the end of the burns and will reenter the atmosphere after passing though an apogee.

6) Prompt hyperbolic reentry (HP): The vehicle has an escape speed but will reenter the atmosphere and may exit and fall into the HES or ELD categories.

7) Circular Orbit Decay (COD): The spiral case of COD is due to failed burns from parking orbit. It is a single point at near circular orbit speed with near zero flight path angle.

The envelope of reentry conditions in prompt, delayed, and powered reentries is plotted on a V-Gamma map. An example of a V-Gamma map is given in Figure 3. The hyperbolic escape category will not appear on the V-Gamma map since it does not lead to reentry. In the orbit decay reentry category, typically the initial elliptical orbit will eventually decay into a circular orbit, and then continues as a COD which is represented by a single point on the V-Gamma map. The entry point and time of entry of an orbit decay reentry are arbitrary, thus only the impact point relative to the assumed entry point can be predicted.

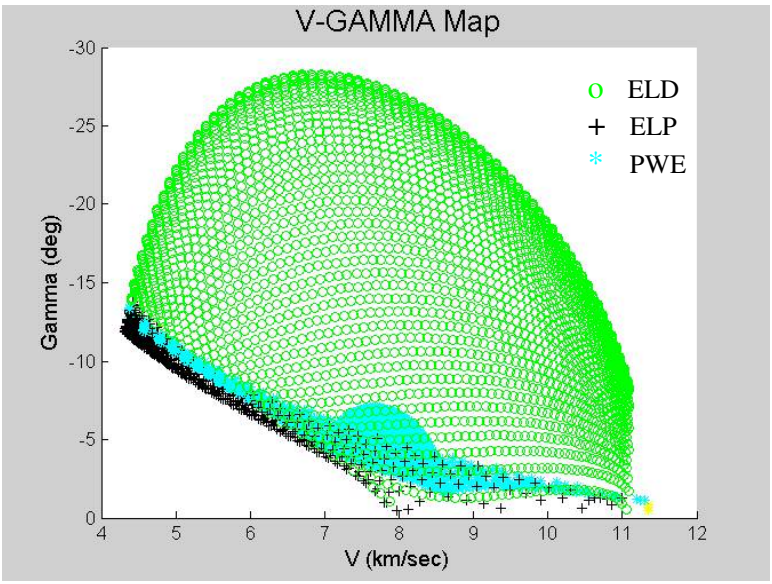


Figure 3. Example of V-Gamma Map

The points within the V-Gamma map are not restricted to the SMB failure scenario; for example, the outcomes of partial burns and no burn are also points within the V-Gamma map. Therefore, a given V-Gamma pair within the map may correspond to multiple failure scenarios, and thus the entry point is not unique. However, the points about the V-Gamma map (on the boundary of the V-Gamma map) are restricted to the SMB failure scenario. Although the SMB may not be a highly probable failure scenario, it does provide an envelope which encompasses everywhere that the vehicle can get to, given the onboard fuel. For each point about the V-Gamma map consisting of the powered, prompt, or delayed entry category, a non-arbitrary entry condition can be determined and associated with it is a specific impact point which can be predicted through trajectory propagation with breakup analysis. Thus, by analyzing a set of "cardinal points" which is fairly distributed about the V-Gamma map to form an entry ellipse, a corresponding bounding impact footprint can be determined. This bounding

footprint also envelops the impact points of the various failure scenarios corresponding to the points within the V-Gamma map.

2.3.2 Modeling of Inertial-Fixed Thrust

The thrust misalignment in a SMB is assumed fixed in the inertial frame. Thus, the modeling of inertial-fixed thrust was developed for propagating a SMB in the burn sequence executed while in the parking orbit. The thrust is assumed to be along the body x-axis:

$$\vec{F}^{b}_{thrust} = F_{thrust}\hat{e}^{b}_{x} \tag{1}$$

where F_{thrust} is the thrust force and $\vec{F}^{b}_{thrust}$ is the thrust vector in body frame coordinates. The thrust misalignment is defined by the cone and clock angles, which are offsets between the body and velocity frames. The cone angle is measured in the sideslip plane with 0º as the nominal burn, and the clock angle is about the body x-axis such that a 90º cone and 90º clock yield an upward thrust. The thrust vector is time-invariant in the inertial frame, obtained by:

$$\vec{F}^{I}_{thrust} = C^{I}_{v}(0)C^{v}_{b}(0)\vec{F}^{b}_{thrust} \tag{2}$$

where: $\vec{F}^{I}_{thrust}$ = thrust in inertial frame coordinates

$C^{I}_{v}(0)$ = matrix for transforming from velocity frame to inertial frame at the start of the burn sequence

$C^{v}_{b}(0)$ = matrix for transforming from body frame to velocity frame at the start of the burn sequence by setting $\alpha = 0$, β = cone, and δ = clock

The thrust vector is transformed from the inertial frame to the velocity frame coordinates at every timestep as a forcing function in the equations of motion:

$$\vec{F}^{v}_{thrust}(t) = C^{v}_{I}(t)\vec{F}^{I}_{thrust} \tag{3}$$

2.3.3 Outcome of Steady Misaligned Burn

Given the pair of cone and clock angles, the burn sequence is simulated by numerical integration of the equations of motion. Aerodynamic drag is not considered for the exo-atmospheric trajectory, and the J_2 gravitation model is used. At the end of the last burn, the semi-major axis (a), eccentricity (e), and radius of perigee (r_p) are obtained by [48]:

$$a = \frac{r\mu_E}{2\mu_E - rv_I^2} \tag{4}$$

$$e = \sqrt{1 - \frac{\left(rv_I \cos\gamma_I\right)^2}{a\mu_E}} \tag{5}$$

$$r_p = a(1-e) \tag{6}$$

where: μ_E = gravitational-mass constant of Earth

r = spacecraft position radius

v_I = inertial speed

γ_I = inertial flight path angle

The outcome of the SMB is then determined by the following:

1. The outcome is a powered entry if entry occurs before the end of the last burn.
2. The outcome is a hyperbolic escape if $a < 0$ or $e > 1$.
3. The outcome is an orbit decay if it is not a hyperbolic escape and the perigee is above the atmosphere.
4. The outcome is a delayed entry if it is not a hyperbolic escape or orbit decay, and $\gamma_I > 0$.

5. The outcome is a prompt entry if it is not a hyperbolic escape or orbit decay, and $\gamma_I < 0$.

Continuing from the end of the last burn, the next course of action is dependent on the category of the SMB outcome as described below:

1. For prompt and powered entries, the trajectory propagation by numerical integration of the equations of motion continues until the reentry altitude is reached and the entry condition is obtained.
2. For hyperbolic escape and orbit decay categories, the trajectory propagation terminates and only end-of-burn condition is determined.
3. For a delayed entry, the time to reentry relative to the start of the burn sequence may be prolonged, making numerical integration of the equations of motion impractical. Therefore, Keplerian motion is assumed, and the reentry condition is obtained by orbital mechanics.

The determination of entry condition for delayed entry is given in the next subsection.

2.3.4 Entry Condition for Delayed Reentry

At the end of the burn sequence in a delayed reentry, the semi-latus rectum (p) is:

$$p = a(1 - e^2) \tag{7}$$

By the definition of delayed entry, the current true anomaly (f) is:

$$f = \cos^{-1}\left(\frac{p - r}{er}\right), \qquad 0 < f \leq \pi \tag{8}$$

The true anomaly at entry interface (f_{EI}), or EI, is:

$$f_{EI} = \cos^{-1}\left(\frac{p - r_{EI}}{er_{EI}}\right), \qquad \pi < f_{EI} < 2\pi \tag{9}$$

The inertial flight path angle at EI (γ_{I_EI}) is:

$$\gamma_{I_EI} = \tan^{-1}\left(\frac{e\sin f_{EI}}{1+e\cos f_{EI}}\right) \tag{10}$$

γ_{I_EI} is negative. The inertial speed at EI (v_{I_EI}) is:

$$v_{I_EI} = \sqrt{\mu_E\left(\frac{2}{r_{EI}} - \frac{1}{a}\right)} \tag{11}$$

Given the position and velocity vectors in inertial frame coordinates ($\vec{r}^{\,I}$ and $\vec{v}_I^{\,I}$), the angular momentum vector ($\vec{H}^I$) is calculated:

$$\vec{H}^I = \vec{r}^{\,I} \times \vec{v}_I^{\,I} \tag{12}$$

The inclination is obtained by [48]:

$$i = \cos^{-1}\left(\frac{H_z}{\left|\vec{H}\right|}\right) \tag{13}$$

where H_Z is the z-component of $\vec{H}^I$, and $\left|\vec{H}\right|$ is the magnitude of the angular momentum. To capture the correct sign and angle, the longitude of the ascending node is obtained using [48]:

$$\sin\Omega_{LAN} = sign(H_z)\frac{H_x}{\left|\vec{H}\right|\sin i}$$

$$\cos\Omega_{LAN} = -sign(H_z)\frac{H_y}{\left|\vec{H}\right|\sin i}$$

where H_X and H_Y are the x and y components of $\vec{H}^I$. This yields the following:

$$\Omega_{LAN} = \tan^{-1}\left(\frac{\sin\Omega_{LAN}}{\cos\Omega_{LAN}}\right) \tag{14}$$

The longitude of the ascending node is between 0º and 360º. To capture the correct sign and angle, the argument of periapsis is obtained using [48]:

$$\sin(\omega_{AOP} + f) = \frac{r_z^I}{r \sin i}$$

$$\cos(\omega_{AOP} + f) = \sec\Omega_{LAN}\left(\frac{r_x^I}{r} + \frac{r_z^I}{r \sin i}\sin\Omega_{LAN}\cos i\right)$$

where r_x^I and r_z^I are the x and z components of the spacecraft position vector in the inertial frame coordinates. This yields the following:

$$\omega_{AOP} = \tan^{-1}\left(\frac{\sin(\omega_{AOP} + f)}{\cos(\omega_{AOP} + f)}\right) - f \tag{15}$$

The argument of periapsis is between 0º and 360º. The position vector at EI in orbit frame coordinates ($\vec{r}_{EI}^{\,o}$) is:

$$\vec{r}_{EI}^{\,o} = r_{EI}\cos f_{EI}\hat{e}_x^o + r_{EI}\sin f_{EI}\hat{e}_y^o \tag{16}$$

The position vector at EI in inertial coordinates is obtained by transformation:

$$r_{EI,x}^I\hat{e}_x^I + r_{EI,y}^I\hat{e}_y^I + r_{EI,z}^I\hat{e}_z^I = C_o^I\vec{r}_{EI}^{\,o}$$

where $r_{EI,x}^I$, $r_{EI,y}^I$, and $r_{EI,z}^I$ are the x, y, and z components of $\vec{r}_{EI}^{\,I}$. Another expression for the position vector in inertial frame coordinates is:

$$\vec{r}_{EI}^{\,I} = r_{EI}\cos\phi_{EI}\cos\Theta_{EI}\hat{e}_x^I + r_{EI}\cos\phi_{EI}\sin\Theta_{EI}\hat{e}_y^I + r_{EI}\sin\phi_{EI}\hat{e}_z^I$$

Thus, the latitude at entry is obtained by:

$$\phi_{EI} = \sin^{-1}\left(\frac{r_{EI,z}^I}{r_{EI}}\right) \tag{17}$$

The celestial longitude at entry is obtained by:

$$\Theta_{EI} = \tan^{-1}\left(\frac{r^I_{EI,y}}{r^I_{EI,x}}\right) \tag{18}$$

To obtain the azimuth, the velocity vector at entry is first obtained:

$$\vec{v}^{\,o}_{I_EI} = v_{I_EI}\left(\frac{\vec{H}\times\vec{r}^{\,o}_{EI}}{\left|\vec{H}\times\vec{r}^{\,o}_{EI}\right|}\right) \tag{19}$$

The inertial velocity vector is transformed to the inertial frame coordinates by:

$$U_{EI}\hat{e}^I_x + V_{EI}\hat{e}^I_y + W_{EI}\hat{e}^I_z = C^I_o\vec{v}^{\,o}_{I_EI} \tag{20}$$

where U_{EI}, V_{EI}, and W_{EI} are the x, y, and z components of the inertial velocity vector at entry interface in the inertial frame coordinates. Transforming to the inertial velocity frame coordinates using Equation (79), the azimuth at entry interface (ψ_{I_EI}) is obtained from the second component:

$$\psi_{I_EI} = \tan^{-1}\left[\frac{-U_{EI}\,\mathrm{s}\Theta_{EI} + V_{EI}\,\mathrm{c}\Theta_{EI}}{-U_{EI}\,\mathrm{s}\phi_{EI}\,\mathrm{c}\Theta_{EI} - V_{EI}\,\mathrm{s}\phi_{EI}\,\mathrm{s}\Theta_{EI} + W_{EI}\,\mathrm{c}\phi_{EI}}\right] \tag{21}$$

The mean orbit rate (n) is:

$$n = \sqrt{\frac{\mu_E}{a^3}}$$

The eccentric anomaly (E) is:

$$E = \cos^{-1}\left(\frac{a-r}{ae}\right)$$

The entry time relative to the current time (t_{EI}) is obtained from:

$$\frac{dE}{dt} = \frac{n}{1-e\cos E}$$

$$t_{EI} = \frac{E_{EI} - E - e(\sin E_{EI} - \sin E)}{n} \tag{22}$$

The terrestrial longitude at EI (θ_{EI}) is calculated using:

$$\theta_{EI} = \Theta_{EI} - \Omega t_{EI} \tag{23}$$

where Ω is the Earth's rate of rotation.

2.3.5 Validation of Non-Arbitrary Entry Conditions

The burn sequence in the test case consisted of two burns separated by a coast period. Staging is not simulated explicitly in the original V-Gamma map but is done in the new software. Thus, the conditions of the staging in the test case are set to those at the start and end of the second burn to be consistent with the original V-Gamma map. The burn sequence is described in Table 2.

Table 2. Burn Sequence for Test Case

Event	Time (sec)	Mass (kg)
Start of burn 1 (Isp = 313.9 sec)	0.0	16800
End of burn 1	158.3	11700
First staging	230.3	7251
Start of burn 2 (Isp = 292.5 sec)	230.3	7251
End of burn 2	317.3	2800
Second staging	317.3	2800

The vehicle state at the start of the first burn is given below:

Altitude = 180.0 km

Relative velocity = 7373.9 m/sec

Latitude = 28.0 deg

Longitude = 0.0 deg

Relative flight path angle = 0.0

Relative azimuth = 90.0 deg

A range of 0º to 180º for the cone angle and a range of -90º to 90º for the clock angle were analyzed at incremental stepsizes of 2º, resulting in 8281 pairs of cone and clock angles. For validation, the resulting V, Gamma, and time were compared with those calculated from the original V-Gamma map software and are given in Table 3 for selected sample pairs of cone and clock angles. For prompt, delayed, and powered entries, the V, Gamma, and time at entry are compared. For the hyperbolic escape and orbit decay categories, the V and Gamma at the end of the last burn are compared.

Table 3. Comparison of V, Gamma, and Time at Entry or End of Last Burn

Cone (deg)	Clock (deg)	Category	V (km/s)		Gamma (deg)		Time (sec)	
			Original VG	New VG	Original VG	New VG	Original VG	New VG
154	-76	PWE	6.96	6.95	-6.32	-6.31	172.7	174.0
166	20	PWE	5.48	5.50	-8.84	-8.72	282.5	286.5
94	-12	PWE	8.38	8.36	-3.75	-3.74	295.6	299.0
140	32	ELP	5.10	5.22	-10.90	-10.43	496.5	493.5
150	50	ELP	4.38	4.57	-13.99	-13.11	488.7	475.5
118	12	ELP	6.83	6.82	-4.78	-4.79	568.5	555.0
134	32	ELD	5.44	5.54	-11.45	-11.12	594.6	590.0
120	18	ELD	6.59	6.60	-6.79	-6.68	677.6	664.6
152	80	ELD	4.10	4.33	-17.96	-17.18	534.0	532.4
22	-82	HE	11.83	11.57	3.25	2.96	N/A	N/A
12	66	HE	11.39	11.16	14.04	13.31	N/A	N/A

32	8	HE	11.17	10.95	10.92	10.32	N/A	N/A
46	-36	DEL	11.29	11.06	0.12	-0.04	N/A	N/A
92	-4	DEL	8.76	8.64	-0.63	-0.70	N/A	N/A
100	4	DEL	8.08	8.00	1.04	0.89	N/A	N/A

Note: VG denotes V-Gamma map.

The other state variables for a non-arbitrary entry point including the time, latitude, longitude, and azimuth calculated from orbital mechanics for delayed entry were validated for selected sample pairs of cone and clock angles by strictly propagating the trajectory until the entry altitude is reached, and the results are given in Table 4.

Table 4. Comparison of Entry Time, Latitude, Longitude, and Azimuth for Delayed Entry

Cone (deg)	Clock (deg)	Time (sec)		Latitude (deg)		Longitude (deg)		Azimuth (deg)	
		New VG	Propagate	New VG	Propagate	New VG	Propagate	New VG	Propagate
140	52	657.17	657.0	29.32	28.74	34.17	34.18	88.80	88.75
124	20	605.64	605.5	32.27	32.24	37.61	37.60	81.06	80.48
126	26	672.40	672.5	32.37	32.26	40.28	40.30	83.43	83.02
132	34	654.30	654.5	31.31	31.13	37.09	37.12	83.76	83.32
130	48	857.18	857.0	31.70	29.96	45.17	45.17	91.61	91.81
128	40	826.54	826.5	32.21	31.23	45.66	45.69	89.40	89.43
120	14	560.72	561.0	32.23	32.23	36.29	36.31	79.71	79.09

The entry angle-of-attack for powered reentry was validated for selected sample pairs of cone and clock angles against the original V-Gamma map and presented in Table 5.

Table 5. Comparison of Entry Angle-of-Attack for Powered Entry

Cone (deg)	Clock (deg)	Angle-of-Attack (deg)	
		Original VG	New VG
176	52	157.50	157.60
58	-64	42.24	42.23
166	8	150.63	150.86
86	-74	69.83	69.83
178	80	157.89	157.39
110	-18	95.67	96.39
160	20	142.49	143.17

The differences in the comparisons shown in Table 3 to Table 5 are due to differences in the approach for trajectory propagation. In the original V-Gamma map software, numerical integration of the equations of motion is performed only during the burn periods; the point mass gravitation model is used; and Keplerian motion is assumed during the periods of no thrust, e.g. the coast periods. The approach for trajectory propagation in the new V-Gamma map software is described in the Section 2.3.3. The propagation method numerically integrates the equations of motion until entry altitude is reached, and the J_2 gravitation model is used.

2.4 Panel Code for Hypersonic Aerodynamic Coefficients

Vehicle breakup typically occurs during the hypersonic regime of the reentry, and the vehicle may change into various configurations as its components fail or break off during the breakup sequence. Therefore, it is necessary to determine the hypersonic aerodynamic properties of various vehicle configurations and components for atmospheric trajectory propagation and breakup analysis. A panel code developed as part

of the legacy software system generated hypersonic aerodynamic coefficients for an axi-symmetric body based on Newtonian theory for hypersonic flow. However, the various configurations of the vehicle during the breakup sequence are most likely not axi-symmetric. Therefore, to increase the fidelity in the modeling of aerodynamics for the trajectory propagation and breakup predictions, a panel code employing triangular panels was developed to calculate the hypersonic aerodynamic force and moment coefficients as functions of angle-of-attack, sideslip angle, and bank angle for an arbitrary-shaped body.

Newtonian theory assumes that in hypersonic flow the shock wave wraps around the vehicle like a glove [51]. When particles in the flow impact the vehicle, the normal momentum is transferred to the surface, but the tangential momentum is preserved [49]. Typically, the force and moment coefficients generated based on Newtonian theory for hypersonic flow will contain prediction errors due to simplification in the modeling of fluid dynamics. However, compared to the highly-accurate wind tunnels and computational fluid dynamics (CFD) which are costly and time-consuming, the prediction errors from the panel code are tolerable considering the savings in cost and time where the efficiency is multiplied by the number of vehicle configurations encountered in the breakup sequence. Therefore, in application to vehicle breakup analysis, the panel code is a less expensive and favorable alternative to wind tunnels and CFD for generating hypersonic aerodynamic coefficients.

Typically, existing panel codes employ rectangular or quadrilateral panels and are useful for relatively simple shapes; e.g. an axi-symmetric shape or body of planar symmetry. An example of a panel code employing quadrilateral panels is the Aerodynamic Preliminary Analysis System II [50]. Since vehicle breakup analyses often

assume simple but odd-shaped bodies for the various vehicle configurations, the modeling of rectangular/quadrilateral panels may pose a challenge for the user to set up the coordinates carefully in order to satisfy the requirement that the four vertices of each rectangular/quadrilateral panel need to be co-planar. This led to the development of the panel code employing triangular panels to allow easy problem setup. Since the three vertices of a triangular panel are always co-planar, the user can define coordinates to simply outline the profile and cross-section of an arbitrary-shaped body. With the flexibility in using triangular panels, the cross-sections along the centerline of the body do not need to be parallel to each other; a cross-section does not need to be normal to the centerline; and a cross-section does not need to be planar, e.g. part of the cross-sectional area can exhibit a deflection angle or include an appendage or a chamfer.

2.4.1 Calculation of Hypersonic Aerodynamic Coefficients

From Newtonian theory for hypersonic flow, the pressure coefficient (C_P) for a surface exposed to the flow is [49]:

$$C_p = C_{p,\max} \cos^2 \theta \tag{24}$$

where $C_{p,max}$ is the maximum pressure at the stagnation point and θ is the angle between the unit vector inward normal to the surface and the velocity vector. $C_{p,max}$ is 2 in Newtonian theory and approximately 1.84 in modified Newtonian theory.

2.4.2 Modeling of Triangular Panels

A body of arbitrary shape at an angle-of-attack (α) and the coordinate systems are illustrated in Figure 4.

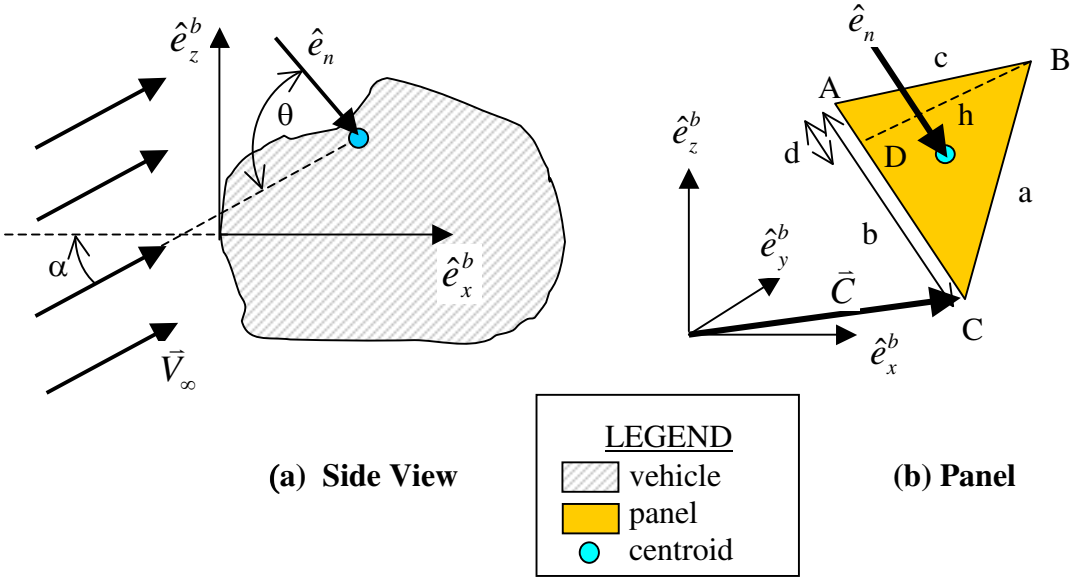


Figure 4. Definitions of Variables and Coordinate Systems

For the particular coordinate systems defined in Figure 4, the matrix (C_v^b) to transform from the velocity frame ($\hat{e}_x^v, \hat{e}_y^v, \hat{e}_z^v$) to the body frame ($\hat{e}_x^b, \hat{e}_y^b, \hat{e}_z^b$) with ϕ-β-α rotation is:

$$C_v^b = \begin{bmatrix} \cos\alpha\cos\beta & \begin{pmatrix}\sin\beta\cos\alpha\cos\phi \\ -\sin\alpha\sin\phi\end{pmatrix} & \begin{pmatrix}-\sin\beta\cos\alpha\sin\phi \\ -\sin\alpha\cos\phi\end{pmatrix} \\ -\sin\beta & \cos\beta\cos\phi & -\cos\beta\sin\phi \\ \sin\alpha\cos\beta & \begin{pmatrix}\sin\beta\sin\alpha\cos\phi \\ +\sin\phi\cos\alpha\end{pmatrix} & \begin{pmatrix}-\sin\beta\sin\alpha\sin\phi \\ +\cos\alpha\cos\phi\end{pmatrix} \end{bmatrix} \tag{25}$$

where α is the angle-of-attack, β is the sideslip angle, and ϕ is the bank angle. Note that the matrix to transform from body to velocity frame (C_b^v) is:

$$C_b^v = \left(C_v^b\right)^T$$

In the velocity frame, the freestream velocity vector ($\vec{V}_\infty$) is:

$$\vec{V}_\infty = V_\infty \hat{e}_x^v$$

Transforming to the body frame, the freestream velocity vector is then:

$$\vec{V}_\infty = V_\infty \left(\cos\alpha \cos\beta \hat{e}_x - \sin\beta \hat{e}_y + \sin\alpha \cos\beta \hat{e}_z \right) \tag{26}$$

A panel is defined by the three vertices A(x_A, y_A, z_A), B(x_B, y_B, z_B), and C(x_C, y_C, z_C), which form the vectors $\vec{A}$, $\vec{B}$, and $\vec{C}$ with respect to the origin as seen in Figure 4. The inward normal unit vector ($\hat{e}^n$) of the panel is calculated by:

$$\vec{n} = \overrightarrow{AB} \times \overrightarrow{AC}$$

$$\hat{e}^n = \frac{\vec{n}}{|\vec{n}|} \tag{27}$$

where: $\overrightarrow{AB}$ = vector from point A to point B ($\overrightarrow{AB} = \vec{B} - \vec{A}$)

$\overrightarrow{AC}$ = vector from point A to point C ($\overrightarrow{AC} = \vec{C} - \vec{A}$)

$\vec{n}$ = vector inward normal to panel surface

Let $a = \left|\overrightarrow{BC}\right|$, $b = \left|\overrightarrow{AC}\right|$, and $c = \left|\overrightarrow{AB}\right|$, where $\overrightarrow{BC}$ is the vector from point B to point C ($\overrightarrow{BC} = \vec{C} - \vec{B}$). Then, the area of the panel is obtained by:

$$d = \frac{c^2 + b^2 - a^2}{2b}$$

$$h = \sqrt{c^2 - d^2}$$

$$area = \frac{bh}{2} \tag{28}$$

From Figure 4, the centroid of the panel relative to the origin ($\vec{r}_{centroid}$) is calculated by:

$$\overrightarrow{AD} = \frac{d}{b}\left(\overrightarrow{AC}\right)$$

$$\vec{D} = \vec{A} + \overrightarrow{AD}$$

$$\overrightarrow{DB} = \vec{B} - \vec{D}$$

$$\overrightarrow{Dh'} = \frac{\overrightarrow{DB}}{3}$$

$$\overrightarrow{Ab'} = \left(\frac{b+d}{3b}\right)\overrightarrow{AC}$$

$$\vec{r}_{centroid} = \vec{A} + \overrightarrow{Ab'} + \overrightarrow{Dh'} = x_{centroid}\hat{e}_x^b + y_{centroid}\hat{e}_y^b + z_{centroid}\hat{e}_z^b \tag{29}$$

The cosine of the angle between the velocity and normal unit vectors (cos θ) is:

$$\cos\theta = \frac{\vec{V}_\infty \bullet \hat{e}_n}{\left|\vec{V}_\infty\right|\left|\hat{e}_n\right|} = \hat{V}_\infty \bullet \hat{e}_n \tag{30}$$

From Equations (24) and (30), C_p can be obtained for each panel. The pressure coefficient as given in Equation (24) describes the inward normal force per unit area acting upon the centroid of the panel and non-dimensionalized by the freestream dynamic pressure. At a panel, the force coefficients outward normal (C_N), tangential (C_A), and outward from the side (C_Y) relative to the body centerline are:

$$\left\{C_{A_i} \quad C_{Y_i} \quad C_{N_i}\right\} = \frac{1}{A_{ref}} C_{p_i} area_i \hat{e}_{n_i} \begin{Bmatrix} \hat{e}_x^b \\ \hat{e}_y^b \\ \hat{e}_z^b \end{Bmatrix}^T \tag{31}$$

where A_{ref} is the reference area and i is the index of the panel. The pitching (C_m), yawing (C_n), and rolling (C_l) moment coefficients from each panel are:

$$\vec{r}'_{centroid_i} = \left(x_{centroid_i} - x_{cg}\right)\hat{e}_x^b + \left(y_{centroid_i} - y_{cg}\right)\hat{e}_y^b + \left(z_{centroid_i} - z_{cg}\right)\hat{e}_z^b$$

$$\left\{C_{l_i} \quad C_{m_i} \quad C_{n_i}\right\} = \frac{1}{l}\vec{r}'_{centroid} \times \left\{C_{A_i} \quad C_{Y_i} \quad C_{N_i}\right\} \tag{32}$$

where: (x_{cg}, y_{cg}, z_{cg}) = coordinates of the center of gravity (c.g.) relative to the origin

l = reference length

$\vec{r}'_{centroid}$ = centroid of panel relative to the c.g.

The force and moment coefficients for the body (C_A, C_Y, C_N, C_l, C_m, C_n) are then obtained by summing up the contributions at the centroid of all the panels. For example,

$$C_N = \sum_i C_{N_i} \tag{33}$$

The lift (C_L), drag (C_D), and side force (C_S) coefficients normal and tangential to the velocity vector are obtained by:

$$\begin{Bmatrix} C_D \\ C_S \\ C_L \end{Bmatrix} = C_b^v \begin{Bmatrix} C_A \\ C_Y \\ C_N \end{Bmatrix} \tag{34}$$

Note that the drag coefficient of a randomly tumbling body can be obtained by taking the average of the drag coefficients at all orientations; e.g. by sweeping across the angle-of-attacks, sideslip angles, and bank angles, and taking the average of the resultant drag coefficients.

The panel code does not take into consideration the shadowing of the forward part onto the back part in the vehicle [51]. For example, the presence of a "valley" in the vehicle shape will result in a higher drag prediction near zero angle-of-attack.

2.4.3 Adaptation to Axi-Symmetric Body

For an axi-symmetric body, the profile is given by n-pairs of coordinates $(x, r)_j$, where j = 1, 2, …, n. Thus, conversion to $(x, y, z)_{j,k}$ coordinates is necessary, where k =

1, 2, … m+1, and m is the number of panels in the x_j-th cross-section. For example, given 10 pairs of (x, r) coordinates for an axi-symmetric body and each cross-section consists of 120 panels, a conversion would yield 10 x 121 = 1210 points in the input array of (x, y, z) coordinates. The conversion is:

$$\begin{aligned} x_{j,k} &= x_j \\ y_{j,k} &= -r_j \sin[(k-1)\Delta\lambda] \\ z_{j,k} &= r_j \cos[(k-1)\Delta\lambda] \end{aligned} \tag{35}$$

where:

$$\Delta\lambda = \frac{2\pi}{m} \tag{36}$$

Note that for an axi-symmetric body, the determination of the aerodynamic coefficients can be simplified by reducing the angle-of-attack and sideslip angle to just one angle, represented by the total angle-of-attack.

2.4.4 Validation of Panel Code

Given the (x, y, z) coordinates for the vertices of the triangular panels for an arbitrary-shaped body, the hypersonic aerodynamic coefficients as functions of angle-of-attack, sideslip angle, and bank angle are calculated by the panel code. The coefficients include: lift, drag, and velocity-frame side-force coefficients (C_L, C_D, C_S); normal, axial, and body-frame side-force coefficients (C_N, C_A, C_Y); and rolling, pitching, and yawing moment coefficients (C_l, C_m, C_n).

Two test cases are analyzed for the validation of the panel code and are presented in the following subsections. The first test case is an axi-symmetric, sharp-nose, circular cone, where the aerodynamic coefficients were predicted using Newtonian theory and documented in Ref. [52]. The second test case is a non-axisymmetric hypersonic vehicle

consisting of a spherically blunted cone with a slice parallel with the axis of the vehicle, and a flap is attached. The aerodynamic coefficients obtained from wind tunnel data are provided in Ref. [53].

For a blunt body, the total drag is mostly due to pressure drag. As the body becomes more slender, the contribution of drag due to skin friction and base drag to the overall drag increases. Therefore, Newtonian theory works better for objects such as a sharp cone [54], and a $C_{p,max}$ of 2 is used in the panel code for the two test cases.

2.4.5 Test Case 1: Sharp-Nose, Circular Cone

The first test case examined for the verification of the panel code was an axi-symmetric, sharp-nose, circular cone with a half angle of 30º and a flat base. The test data were obtained from Table XXI of Ref. [52] where C_N, C_A, and C_Y as functions of angle-of-attack and sideslip angle were obtained based on Newtonian theory. Excellent comparisons were produced, and the comparisons of the aerodynamic coefficients are given in Figure 5 through Figure 7. Note that "Beta" is the sideslip angle, "Test" denotes the test data from Ref. [52], and "Panel" denotes the data obtained from the panel code.

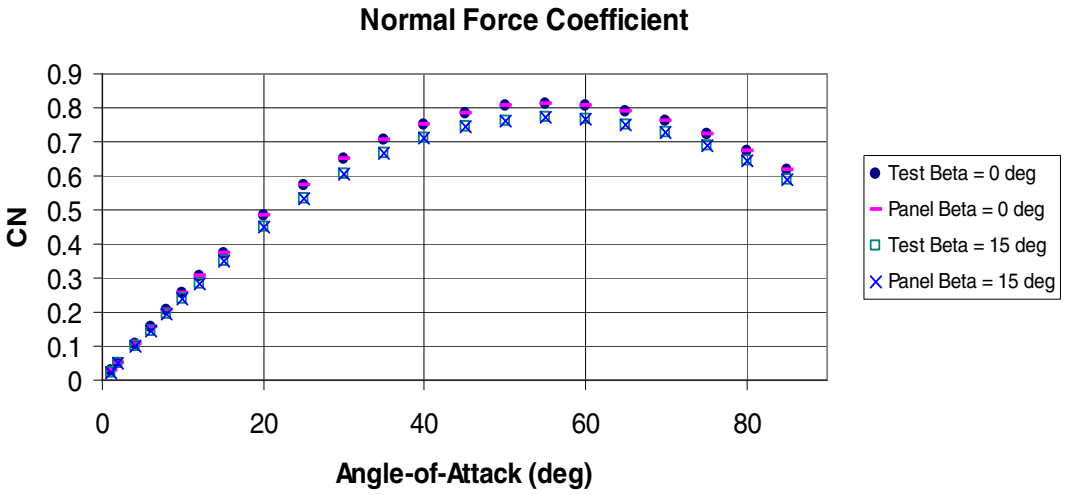


Figure 5. Comparison of C_N in Sharp-Nose, Circular Cone Test Case

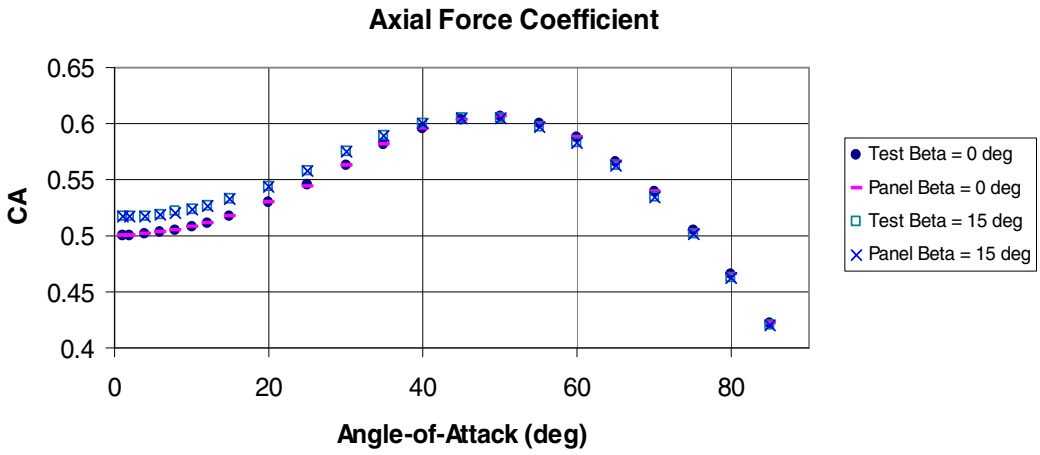


Figure 6. Comparison of C_A in Sharp-Nose, Circular Cone Test Case

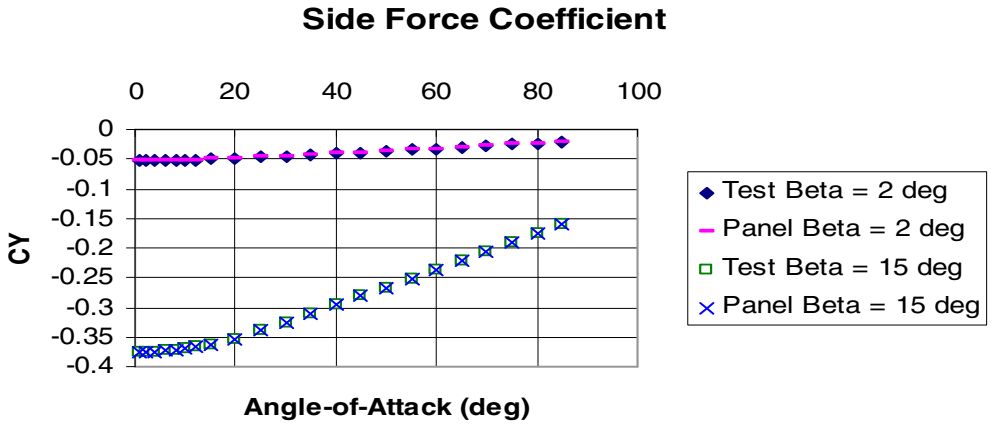


Figure 7. Comparison of C_Y in Sharp-Nose, Circular Cone Test Case

2.4.6 Test Case 2: A Hypersonic Vehicle

The second test case was a non-axisymmetric hypersonic vehicle of planar symmetry as shown in Figure 8. The vehicle consisted of a spherically blunted cone with a slice parallel with the axis of the vehicle, and a flap is attached. The flap can be deflected at 0º, 10º, 20º, or 30º. The reference area was 11.525 in^2; the reference length was 4 in; and the c.g. was at half the body length.

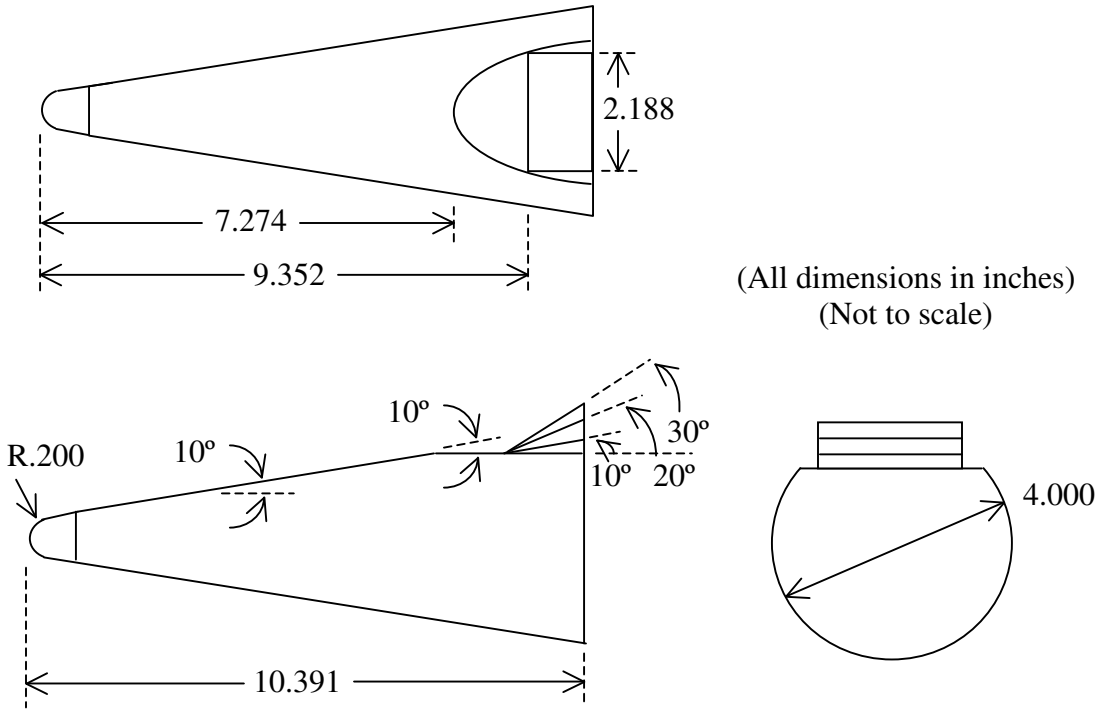


Figure 8. Hypersonic Vehicle

Wind tunnel data as a function of the angle-of-attack were provided in Ref. [53] for the following:

1. C_N, C_A, and C_m for a flap deflection angle (δ) of 0º
2. C_N and C_A for $\delta = 10º$
3. C_A for $\delta = 20º$
4. C_A for $\delta = 30º$

The aerodynamic coefficients generated from the panel code are compared with the wind tunnel data and plotted in Figure 9 through Figure 12. Ref. [53] defined its angle-of-attack as "positive when slice is on windward side", which yields the opposite sign as the angle-of-attack defined in Figure 4. Therefore, in the outputs of the panel code, the angle-of-attack, C_N, and C_m were multiplied by -1 to adjust for this difference in

sign. Note that the panel code was able to correctly determine the non-zero pitching moment at zero angle-of-attack in Figure 9 resulting from the slice in the cone.

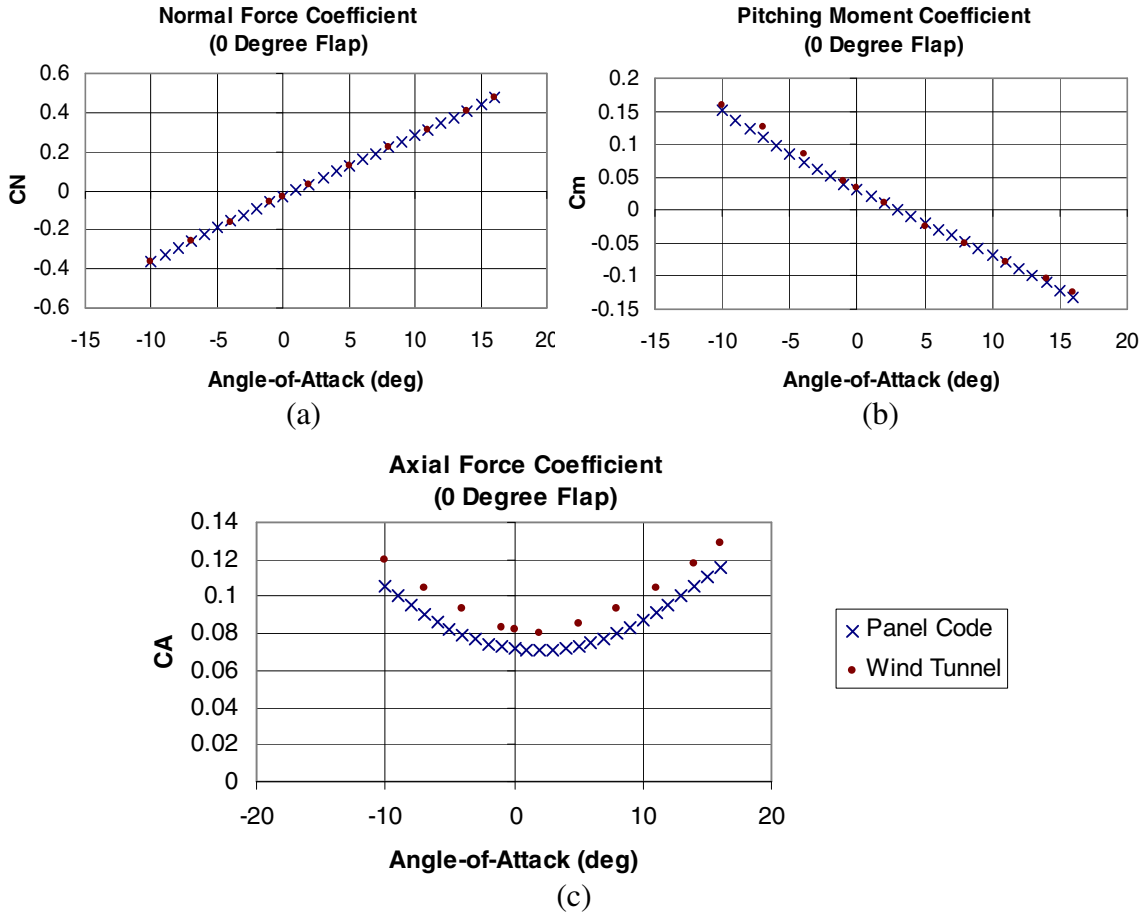


Figure 9. Comparisons of (a) C_N, (b) C_m, and (c) C_A for Hypersonic Vehicle with 0º Flap Deflection Angle

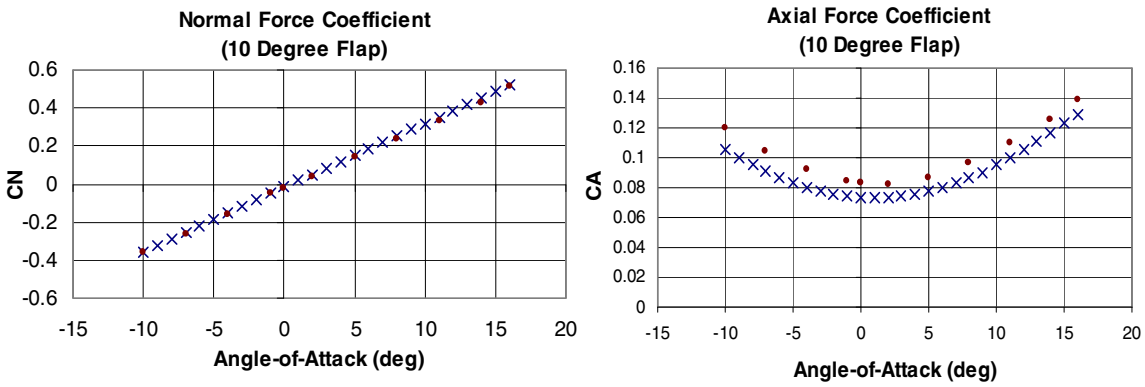


Figure 10. Comparisons of C_N and C_A for Hypersonic Vehicle with 10º Flap Deflection Angle

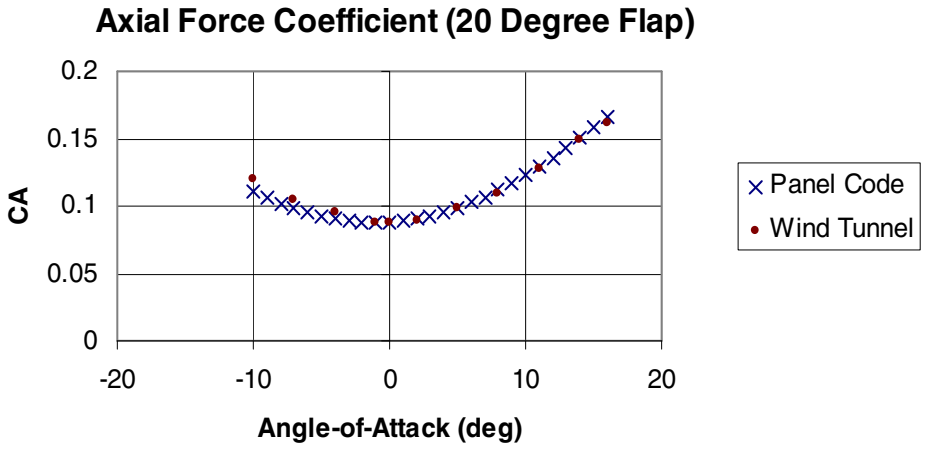


Figure 11. Comparison of C_A for Hypersonic Vehicle with 20º Flap Deflection Angle

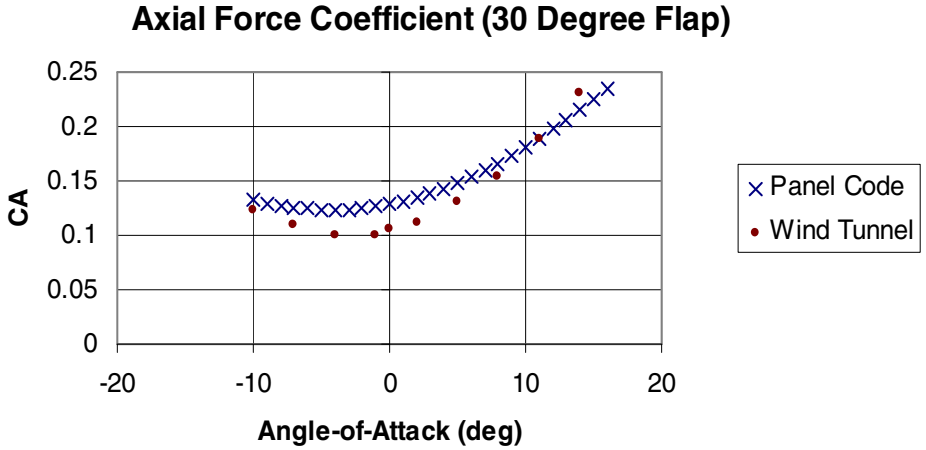


Figure 12. Comparison of C_A for Hypersonic Vehicle with 30º Flap Deflection Angle

The root mean squares of the differences between the aerodynamic coefficients generated from the panel code and the wind tunnel are given in Table 6. The differences are mostly due to simplification in the modeling of fluid dynamics in Newtonian theory used in the panel code.

Table 6. Root Mean Squares of Differences in Aerodynamic Coefficients

Flap Deflection Angle	C_A	C_N	C_m
0º	0.012	0.003	0.007
10º	0.011	0.012	N/A
20º	0.004	N/A	N/A
30º	0.018	N/A	N/A

2.5 Calculations of Failure Criteria

In general, the failure integrated heating per unit area (ΔQ_{fail} in J/cm^2) for a component is:

$$\Delta Q_{fail} = \frac{mc\Delta T}{A_{flow}(HF)(EF)} + \Delta Q_{rad} \tag{37}$$

where c is the material specific heat (kJ/(kg·K)) and ΔT is the rise temperature from current condition to node failure (K); e.g., melting or zero strength temperature subtract 273 K. The radiative cooling, ΔQ_{rad}, is approximated by:

$$\Delta Q_{rad} = -\sigma\varepsilon(0.65T_{melt})^4 \Delta t_{heatup\ phase} \tag{38}$$

where $\Delta t_{heatup\ phase}$ is the time duration of the heatup phase; σ is the Stefan-Boltzman constant; ε is the emissivity; and T_{melt} is the melting temperature. For example, the failure integrated heating for a hollow cylinder is calculated by:

$$\Delta Q_{fail} = \frac{c\Delta T \rho (r_{outer}^2 - r_{inner}^2)}{2r_{outer}(HF)(EF)} + \Delta Q_{rad} \tag{39}$$

where: ρ = material density (g/cm^3)

r_{outer} = outer radius of hollow cylinder (cm)

r_{inner} = inner radius of hollow cylinder (cm)

For a good conductor or a spinning cylinder subject to constant exposure to the flow, the conductive heating term (first term) on the right-hand-side is multiplied by π.

The failure criteria for specific spacecraft components are given in the following subsections. Before the implementation of the calculation of failure criteria into the upgraded analysis tool, the failure criteria were calculated by hand. Verification of the calculation of failure criteria was done by comparing with the hand-calculations, and therefore not presented here.

2.5.1 Aeroshell

The failure criteria for the aeroshell may be provided. If unavailable, the failure criteria can be calculated based on the design margin. A heatshield (H/S) is generally designed to 100% margin on the nominal entry heating, with 22% on the backshell (B/S) and 60% on the shoulder. The failure integrated heating values are thus:

$$\begin{aligned}
\Delta Q_{fail_H/S} &= \frac{2Q_{nom}}{EF} + \Delta Q_{rad} \\
\Delta Q_{fail_B/S} &= \frac{0.22\ \Delta Q_{fail_H/S}}{EF} + \Delta Q_{rad} \\
\Delta Q_{fail_shoulder} &= \frac{0.6\ \Delta Q_{fail_H/S}}{(HF)(EF)} + \Delta Q_{rad}
\end{aligned} \tag{40}$$

where Q_{nom} is the nominal entry heating (J/cm^2). The shoulder radius is usually about 0.1 of the nose radius and assumes a heating factor for cylindrical geometry. If the vehicle flying side-on is tumbling always side-on, the exposure factor is $1/\pi$. If the vehicle is tumbling nose over tail, two places on the shoulder each see the flow about 1/4 of the time. To obtain the general failure criteria for flying side-on, a factor of π is assumed.

2.5.2 Thermal Blanket

The thermal blanket typically consists of an outer layer, e.g. Kapton; multiple interior layers, e.g. Mylar and Dacron net; and an inner layer, e.g. Kapton. The failure heating rate is based on the radiation equilibrium for a surface normal to the flow in hypersonic, free-molecular flow:

$$q_{fail} = (EF)\sigma\varepsilon\Delta T^4 \tag{41}$$

Note that this failure criterion is only for the outer layer of the thermal blanket. However, the interior layers are assumed to fail quickly due to their low zero strength temperatures. The inner layer also fails quickly as the heat flux continues to increase. Therefore, the q_{fail} calculated above is assumed to be the failure criterion of the thermal blanket. The vehicle's attitude, e.g. flying forward/backward or tumbling, is modeled by the exposure factor. The thermal blanket is expected to fail quickly, and thus radiative cooling is assumed negligible.

2.5.3 Solar Array

The solar array is typically a sandwich consisting of graphite epoxy (GE) facesheets (FS) with an interior aluminum honeycomb core. When the two facesheets fail, the honeycomb core loses support and breaks apart. Therefore, the failure of the

solar array occurs when the 2 facesheets fail. The total failure integrated heating for the 2 facesheets depends on the vehicle's attitude. If the vehicle is flying forward/backward, the facesheet facing the flow has an exposure factor of 1 and needs to fail first before the aft facesheet becomes partially exposed to the air flowing through the honeycomb core. This partial exposure is modeled by the exposure factor for the aft facesheet and is dependent on the density/porosity of the honeycomb core, e.g. typical EF = 1/3 or 1/4. Therefore, the total failure integrated heating is:

$$\Delta Q_{fail} = \left(\frac{c\rho d\Delta T}{HF} + \Delta Q_{rad} \right)_{front\ FS} + \left(\frac{c\rho d\Delta T}{(HF)(EF)} + \Delta Q_{rad} \right)_{aft\ FS} \tag{42}$$

(flying forward/backward)

where d is the thickness of the facesheet. For a tumbling vehicle, the facesheets are in a timeshare for exposure to the flow and will fail at about the same time, instead of consecutively as in flying forward/backward. Therefore, the total failure integrated heating is:

$$\Delta Q_{fail} = \frac{c\rho d\Delta T}{(HF)(EF)} + \Delta Q_{rad} \tag{43}$$

(tumbling)

2.5.4 Propellant Tanks

A propellant tank typically has a gas side and a liquid fuel side, separated by a thin diaphragm. The gas and liquid are typically helium (He) and hydrazine (N2H4). Whether the tank fails first on the gas side or liquid side depends on the vehicle's attitude. The failure integrated heating of the gas side of the tank is:

$$\Delta Q_{fail} = \frac{c\rho d\Delta T}{(HF)(EF_{gas\ side})} + \Delta Q_{rad} \tag{44}$$

(gas side)

where d is the thickness of the tank. Note that for a tumbling vehicle, the g-load is assumed to be relatively small and does not distort the diaphragm to a great extent.

Two scenarios are considered for the failure of the liquid side: failure due to burst pressure and failure due to burnout flux. These are discussed in the following subsections. Note that the calculation of burnout flux is also given in Ref. [41].

2.5.4.1 Burst Pressure

The vapor pressure of the liquid is:

$$vapor\ pressure\ of\ \ liquid = \exp\left(C_1 + \frac{C_2}{T} + C_3 \ln T + C_4 T^{C_5} \right) \tag{45}$$

where vapor pressure is in Pa, T is temperature in K, and C_1 through C_5 are liquid-dependent coefficients obtained from handbooks. As the gas heats up, the gas pressure increases proportionally:

$$gas\ pressure = \left(\frac{T}{T_{operating}} \right) P_{operating} \tag{46}$$

where $T_{operating}$ and $P_{operating}$ are the operating temperature and pressure. The $T_{operating}$ is typically assumed to be near room temperature at 293 K, and $P_{operating}$ is provided. The total pressure in the tank is then:

$$total\ pressure = vapor\ pressure\ of\ \ liquid + gas\ pressure \tag{47}$$

The tank burst pressure (P_{burst}) at room temperature (T_{room}) is provided. The tank failure pressure for a given temperature is then based on the percentage of room temperature tensile yield strength of the tank material (≤ 1) obtained from handbooks:

$$P_{fail} = (\%\ T_{room}\ \ tensile\ yield\ \ strength) P_{burst} \tag{48}$$

Tank failure occurs when the total pressure exceeds the tank failure pressure:

$$T_{fail} = T \text{ at which total pressure} > P_{fail} \tag{49}$$

The heat required to heat the liquid from the operating temperature comes from the heat supplied by the airflow and is given in terms of the reference integrated heating:

$$\Delta Q_{fail} = \left[(mc)_{tank} + (mc)_{liquid} \right] \frac{(T_{fail} - T_{operating})}{EF_{liquid\ side} HF_{tank} A_{flow}} + \Delta Q_{rad} \tag{50}$$

where m is mass, and A_{flow} is the tank surface area normal to the flow, e.g. πr_{tank}^2 for a spherical tank.

2.5.4.2 Burnout Flux

Another failure scenario is for the liquid propellant tank to burn through once the convective heat flux exceeds the burnout flux. The convective heat flux applied to the tank is transferred to the liquid propellant by nucleate boiling [55]. As the external heat flux rises and the nucleate boiling limit is exceeded, the liquid can no longer serve as a heat sink. Thus, heating is absorbed by the tank wall, and subsequently tank failure occurs.

The liquid propellant is sufficient to keep the tank cool, until a critical heat flux is reached when a vapor volume is formed inside, allowing the tank temperature to increase locally to the melt condition. The burnout flux ($q_{burnout}$) is calculated by:

$$q_{burnout} = \frac{\pi h_{fg} \rho_v}{24} \left(1 \times 10^7 \sigma_{fg} g_{Earth} gload \frac{\rho_l - \rho_v}{\rho_v^2} \right)^{1/4} \sqrt{1 + \frac{\rho_v}{\rho_l}} \tag{51}$$

where: h_{fg} = enthalpy of vaporization

ρ_v = density of saturated vapor

σ_{fg} = surface tension of liquid-vapor

g_{Earth} = Earth's gravitational acceleration

gload = perturbing acceleration normalized to g_{Earth}

ρ_l = density of saturated liquid

After exceeding the burnout heat flux, a vapor volume forms inside the tank at the stagnation point, and the tank wall is quickly heated to a point where it fails under the internal pressure, and the liquid quickly spills out. Therefore, the tank failure heat flux is:

$$q_{fail} = \frac{q_{burnout}}{\left(HF_{\text{tank}}\right)\left(EF_{liquid\ side}\right)} \tag{52}$$

2.6 Sensitivity Analysis

For sensitivity analysis, parametric biases are applied to the variables listed in Table 7, with examples of their uncertainties attained from engineering judgment based on past experience in vehicle breakup analysis. The impact footprint is then determined from the latitudes and longitudes of the surface impact points as described in Sec. 2.7.

Table 7. Parametric Biases in Sensitivity Analysis

Parameter	Examples of Uncertainties (at t = 0 sec)
Relative flight path angle	± 0.1 deg
Relative speed	± 0.1%
L/D	± 0.03
Mass	± 1%
C_D	± 10%
A_{ref}	± 10%
Side Force	L/D = 0.03 with bank angle at ± 45 deg

The sensitivity analysis was performed by using a script file set up with an automated sequence of runs covering the range of uncertainties listed in Table 7. It was verified by comparing the results obtained by running each dispersed case individually and as part of the sensitivity analysis. The initial condition and vehicle characteristics for the test case were:

Altitude	= 124.97 km
Relative speed	= 10757.36 m/sec
Relative flight path angle	= -8.305 deg
Latitude	= 44.395 deg
Longitude	= 238.104 deg
Azimuth	= 121.505 deg
Mass	= 205.17 kg
C_D	= 1.09
A_{ref}	= 1.767 m^2

The results obtained from the individual runs and from the sensitivity analysis were identical, and the dispersed impact points for the test case are given in Table 8.

Table 8. Impact Points from Sensitivity Analysis

Case	Impact Latitude (deg)	Impact Longitude (deg)
Nominal	40.520	245.784
γ_{EI} +0.1°	40.451	245.903
γ_{EI} -0.1°	40.586	245.669
V_{EI} +0.1%	40.518	245.788
V_{EI} -0.1%	40.522	245.780
L/D = 0.03	40.351	246.070

L/D = -0.03	40.646	245.560
Mass +1%	40.516	245.791
Mass -1%	40.524	245.776
C_D +10%	40.562	245.711
C_D -10%	40.474	245.864
A_{ref} +10%	40.562	245.711
A_{ref} -10%	40.474	245.864
δ = 45° and L/D = 0.03	40.367	245.933
δ = -45° and L/D = 0.03	40.451	246.018
Local winds	40.518	245.807

2.7 Footprint Determination

An impact ellipse is determined from surface impact points obtained from a parametric/sensitivity analysis or Monte Carlo run. The set of impact points expressed in latitude and longitude is transformed to an x'-y' coordinate system as shown in Figure 13:

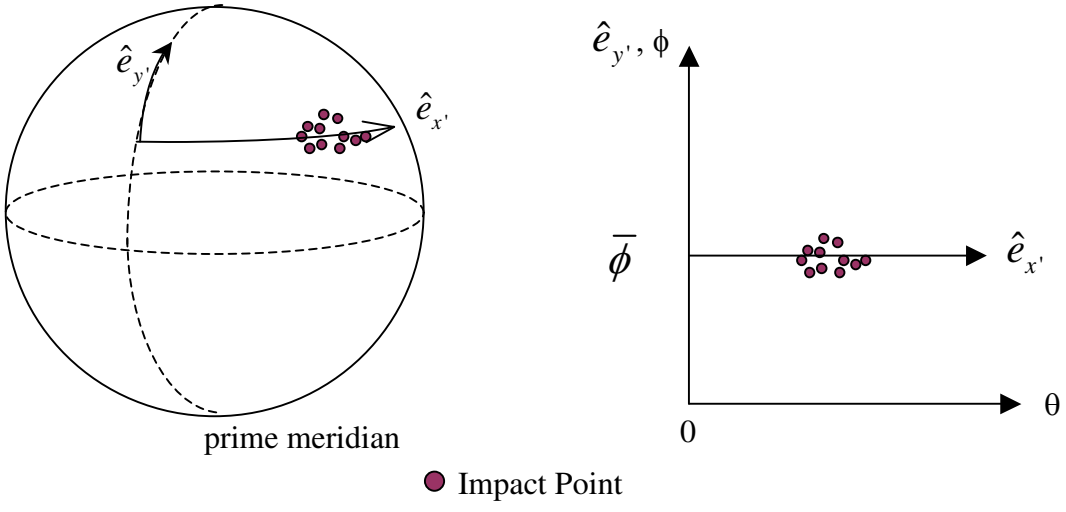


Figure 13. Coordinate System for Footprint Determination

The *i*-th impact point expressed in (x', y') is obtained by: [56]

$$\begin{aligned} x_i^{'} &= \theta_i r_{planet} \cos(\bar{\phi}) \\ y_i^{'} &= (\phi_i - \bar{\phi}) r_{planet} \end{aligned} \tag{53}$$

where the mean latitude for n samples ($\bar{\phi}$) is calculated by:

$$\bar{\phi} = \frac{\sum \phi}{n} \tag{54}$$

Similarly, the means for the set of x' coordinates ($\overline{x'}$) and y' coordinates ($\overline{y'}$) are calculated. The standard deviation for the set of x' coordinates ($\sigma_{x'}$) using the nonbiased or n-1 method is:

$$\sigma_{x'} = \sqrt{\frac{n\sum x'^2 - \left(\sum x'\right)^2}{n(n-1)}} \tag{55}$$

Similarly, the standard deviation for the set of y' coordinates is calculated. The correlation coefficient (C_{corr}) is calculated by:

$$C_{corr} = \frac{\sum\left(x' - \overline{x'}\right)\left(y' - \overline{y'}\right)}{n\sqrt{\frac{\sum\left(x' - \overline{x'}\right)^2}{n}}\sqrt{\frac{\sum\left(y' - \overline{y'}\right)^2}{n}}} \tag{56}$$

Note that the 2 x 2 covariance matrix is formed by: [56]

$$\begin{bmatrix} \sigma_{x'} & C_{corr}\sigma_{x'}\sigma_{y'} \\ C_{corr}\sigma_{x'}\sigma_{y'} & \sigma_{y'} \end{bmatrix}.$$

The 1-σ semi-major axis is obtained by: [56]

$$sma_{1\sigma} = \sqrt{\frac{\sigma_{x'}^2 + \sigma_{y'}^2}{2}} + \sqrt{\frac{\left(\sigma_{x'}^2 - \sigma_{y'}^2\right)^2}{4} + \left(C_{corr}\sigma_{x'}\sigma_{y'}\right)^2} \tag{57}$$

The 1-σ semi-minor axis is obtained by: [56]

$$smi_{1\sigma} = \sqrt{\sigma_{x'}^2 + \sigma_{y'}^2 - sma_{1\sigma}^2} \tag{58}$$

The n-σ semi-major and semi-minor axes are obtained by:

$$\begin{aligned} sma_{n\sigma} &= n\left(sma_{1\sigma}\right) \\ smi_{n\sigma} &= n\left(smi_{1\sigma}\right) \end{aligned} \tag{59}$$

Various confidence intervals are given in Table 9. [56]

Table 9. Confidence Intervals

n	Confidence Interval
0.4590	10 %
1.1774	50 %
2.146	90 %
2.4478	95 %
3.03516	99 %

The angle between the semi-major axis and the x' axis (ϑ) is: [56]

$$\vartheta = 90° - \tan^{-1}\left(\frac{C_{corr}\sigma_x\sigma_y}{sma_{1\sigma}^2 - \sigma_x^2}\right) \tag{60}$$

The azimuth is calculated by: [56]

$$if \begin{cases} \vartheta > 90°, & \psi = 270° - \vartheta \\ else, & \psi = 90° - \vartheta \end{cases} \tag{61}$$

In a coordinate system with the origin at the center of the footprint, the j-th (h, k) coordinates of the footprint along the semi-major and semi-minor axes are obtained using the equation for an ellipse:

For $-sma \le h_j \le sma$,

$$k_j = \pm\sqrt{smi^2\left(1-\frac{h_j^2}{sma^2}\right)} \tag{62}$$

The (h, k) coordinates of the footprint are transformed to the (x', y') coordinates by: [56]

$$\begin{Bmatrix} x_j' \\ y_j' \end{Bmatrix} = \begin{bmatrix} \cos\vartheta & -\sin\vartheta \\ \sin\vartheta & \cos\vartheta \end{bmatrix} \begin{Bmatrix} h_j \\ k_j \end{Bmatrix} + \begin{Bmatrix} \overline{x'} \\ \overline{y'} \end{Bmatrix} \tag{63}$$

The (x', y') coordinates of the footprint are transformed back to latitude and longitude by:

$$\begin{aligned} \phi_j &= \frac{y_j'}{r_{planet}} + \overline{\phi} \\ \theta_j &= \frac{x_j'}{r_{planet}\cos\overline{\phi}} \end{aligned} \tag{64}$$

The impact footprint is calculated automatically at the end of a sensitivity analysis using the dispersed impact points obtained. To verify the calculation of the footprint, the dispersed impact points from a sensitivity analysis (Table 8) were imported to another software [56] used in conjunction with the AEPL program [31] for the determination of footprint. The footprints obtained were identical and shown in Figure 14.

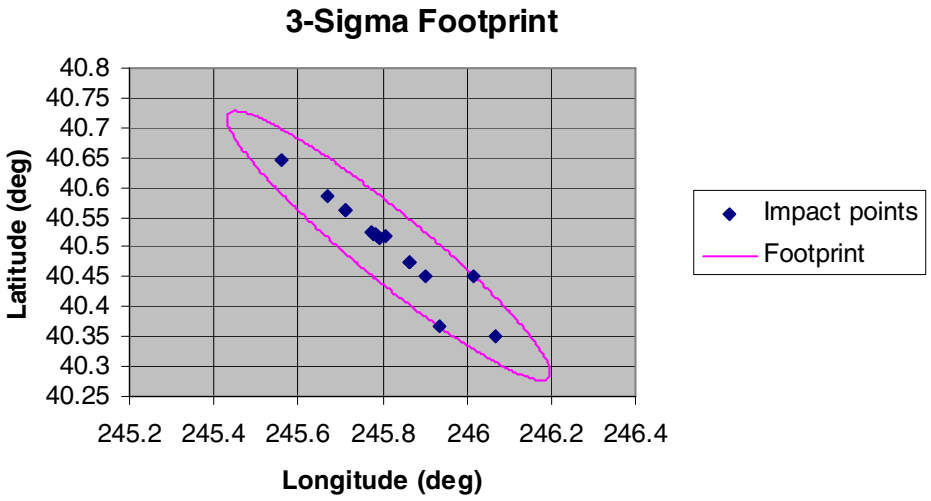


Figure 14. 3-Sigma Footprint

2.8 Modeling of Local Winds

To enhance the accuracy of the footprint prediction, the effects of wind are added in the trajectory propagation. During an actual launch contingency, the real-time local wind profiles obtained from the website of the Air Resources Laboratory of the National Oceanic and Atmospheric Administration (ARL of NOAA) [43] would be used in lieu of synthetic wind models. The effects of local winds produce both downrange and crossrange variations in the prediction of impact point and are included in the sensitivity analysis for the generation of impact footprint.

The vehicle velocity vector expressed in the navigation frame is:

$$\dot{\vec{r}}_R^{\,n} = v_R(\sin\gamma_R \hat{e}_r^{\,n} + \sin\psi_R \cos\gamma_R \hat{e}_\theta^{\,n} + \cos\psi_R \cos\gamma_R \hat{e}_\phi^{\,n})$$

where: $\dot{\vec{r}}_R^{\,n}$ = relative velocity vector of vehicle in navigation frame

v_R = relative speed of vehicle

γ_R = relative flight path angle of vehicle

ψ_R = relative azimuth due north of vehicle

The relative velocity describes the motion of the vehicle with respect to the rotating atmosphere and is the same as the aerodynamic velocity in the absence of local winds.

In a NOAA wind profile, the wind velocity is assumed to be in the local horizontal plane, and the flight path angle of the wind is zero ($\gamma_{wind} = 0^o$). Therefore, the wind velocity in the navigation frame ($\dot{\vec{r}}^n_{wind}$) is:

$$\vec{v}^n_{wind} = \dot{\vec{r}}^n_{wind} = v_{wind}(\sin\psi_{wind}\hat{e}_\theta{}^n + \cos\psi_{wind}\hat{e}_\phi{}^n) \tag{65}$$

where v_{wind} is the wind speed. The wind velocity projected onto the spacecraft velocity frame ($\vec{v}^v_{wind}$) is:

$$\vec{v}^v_{wind} = C^v_n \vec{v}^n_{wind} \tag{66}$$

The spacecraft relative velocity in the velocity frame ($\dot{\vec{r}}_R{}^v$) is:

$$\dot{\vec{r}}_R{}^v = v_R \hat{e}_x{}^v \tag{67}$$

Thus, the aerodynamic velocity ($\vec{v}^v_{aero}$) is:

$$\vec{v}^v_{aero} = \dot{\vec{r}}_R{}^v + \vec{v}^v_{wind} \tag{68}$$

The aerodynamic speed is then:

$$v_{aero} = \left|\vec{v}^v_{aero}\right| \tag{69}$$

Note that there exists an aerodynamic velocity frame ($\hat{e}^a_x, \hat{e}^a_y, \hat{e}^a_z$) such that:

$$\vec{v}^a_{aero} = v_{aero}\hat{e}^a_x$$

The aerodynamic velocity vector is illustrated in Figure 15.

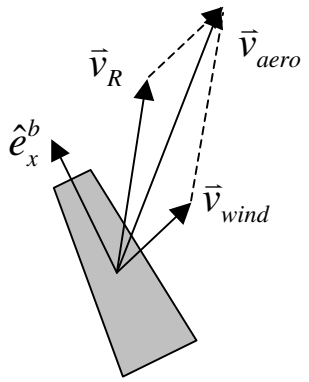


Figure 15. Relative, Wind, and Aerodynamic Velocity Vectors

The aerodynamic velocity vector in the body frame is obtained by:

$$\vec{v}_{aero}^{\,b} = C_v^b \vec{v}_{aero}^{\,v} = v_{aero,x}^b \hat{e}_x^b + v_{aero,y}^b \hat{e}_y^b + v_{aero,z}^b \hat{e}_z^b \tag{70}$$

where $v_{aero,x}^b$, $v_{aero,y}^b$, and $v_{aero,z}^b$ are the three components of the aerodynamic velocity in the body frame. The angle-of-attack of the spacecraft relative to the aerodynamic velocity (α_a) is:

$$\alpha_a = \tan^{-1} \frac{v_{aero,z}^b}{v_{aero,x}^b} \tag{71}$$

The sideslip angle of the spacecraft relative to the aerodynamic velocity (β_a) is:

$$\beta_a = \sin^{-1} \frac{v_{aero,y}^b}{v_{aero}} \tag{72}$$

The bank angle of the spacecraft relative to the aerodynamic velocity (δ_a) is:

$$\delta_a = \tan^{-1} \frac{v_{aero,y}^b}{v_{aero,z}^b} \tag{73}$$

The Mach number based on aerodynamic velocity is:

$$M_a = \frac{v_{aero}}{v_{sound}}$$

where v_{sound} is the speed of sound. The aerodynamic lift (L) and drag (D) forces are then calculated based on v_{aero}, M_a, α_a, β_a, and δ_a. For example,

$$\begin{aligned} L &= \frac{1}{2}\rho_\infty v_{aero}^2 A_{ref} C_L(M_a, \alpha_a, \beta_a, \delta_a) \\ D &= \frac{1}{2}\rho_\infty v_{aero}^2 A_{ref} C_D(M_a, \alpha_a, \beta_a, \delta_a) \end{aligned} \tag{74}$$

where ρ_∞ is the freestream atmospheric density and A_{ref} is the reference area.

The modeling of local winds would be the most effective in application to a 6-DOF trajectory simulation. However, the initial implementation of the modeling of local winds was done in a 3-DOF trajectory simulation for translational motion of the spacecraft. A test case was not available to verify the modeling of local winds. A simulation run was made for the Mars Exploration Rover (MER) case study and is presented later in Section 3.5.

3. Results of New Dynamics Modeling and Capabilities

A case study is discussed in this section using the Mars Exploration Rover Mission to demonstrate the improvements made to vehicle breakup analysis for applications in aerospace nuclear safety as a result of the new dynamics modeling and capabilities developed for the upgraded analysis tool. Comparison with results from the legacy software is given wherever applicable.

3.1 Case Study: Mars Exploration Rover Mission

NASA's twin robot geologists, MER-A and MER-B, were launched on June 10 and July 7, 2003, respectively, in search of answers about the history of waters on Mars. The two rovers were delivered in landing craft to separate sites on Mars in January 2004.

MER-A was launched using a Delta II 7925 launch vehicle, and since MER-B required more energy to get to Mars, a Delta II 7925 H was used. After the boost stage (Stage I), two more stages were used to inject the spacecraft into a trajectory to Mars. Stage II fired twice, once to insert the vehicle-spacecraft stack into a low Earth orbit, and then again to provide the required proper Mars alignment and velocity for the third stage and MER. The purpose of Stage III/Star 48 was to provide the majority of the velocity change needed to leave Earth and then inject the spacecraft into a trajectory for Mars.

Embedded within the rovers were LWRHUscontaining plutonium dioxide fuel to provide heat by radioactive decay [57]. In the unlikely event of a mission failure during launch before the spacecraft began the interplanetary cruise to Mars, atmospheric reentry of the spacecraft was possible. Therefore, contingency plans were required for rapid response with the ultimate goal of retrieving the LWRHU modules for environmental protection. To achieve this objective, knowledge of the LWRHU impact footprint was required. The footprint was generated by trajectory propagations with the simulation of vehicle breakup based on thermal and structural analyses, performed within a range of uncertainties.

Pre-launch vehicle breakup analysis and footprint predictions were performed to facilitate and expedite response in case of a contingency during launch. The objectives of the pre-launch vehicle breakup analysis included: (1) Determine whether the LWRHU

modules were released from the spacecraft during an accidental atmospheric reentry and (2) predict the impact footprint of the LWRHUs or the component containing the LWRHUs. A wide scope of possible reentry scenarios was investigated including suborbital reentries resulting from failure during the ascent and out-of-orbit reentries resulting from failure while in the parking orbit.

Information on the spacecraft, launch vehicle, thermal nodes, exposure factors, failure criteria, etc, required to perform vehicle breakup analysis are given in Appendix G.

3.2 Predictions of Impact Points in Suborbital Reentries

Suborbital reentries were analyzed for the following FTS activation times:

1. Low speed (ocean impact): 100, 150, 220.8, 261, 293, 400, 450, 500, 550, and 560 sec
2. High speed (land impact): 571.073 sec

The vehicle state vectors at the times of FTS activation obtained from the ascent trajectories [58] were used as the initial conditions of the spacecraft ballistic trajectories.

In the ten cases analyzed for low speed suborbital reentry, the detonation of the launch vehicle during ascent would release the spacecraft into a ballistic trajectory. For FTS activation times of 220.8 sec and earlier, the spacecraft did not reach an altitude above the atmosphere before beginning its descent trajectory. In these cases, heating during the ascent portion of the trajectories were also considered in the integration of heating rate. For FTS activation times of 261 sec and greater, the spacecraft had enough energy to temporarily exit the atmosphere during which the ascent heating was assumed to have dissipated, and thus only heating during the post-reentry descent were considered

in the integration of heating rate. Figure 16 shows the integrated heating versus FTS activation time where (1) ascent heating was considered without breakup analysis, (2) only descent heating was considered without breakup analysis, and (3) only descent heating was considered with breakup analysis (with restarts).

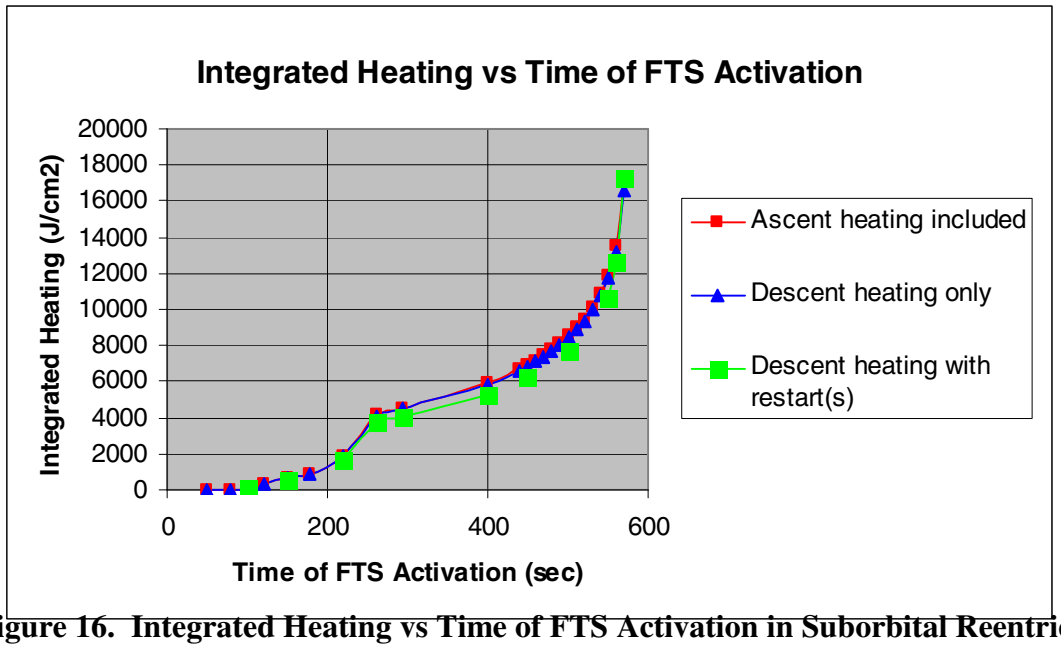
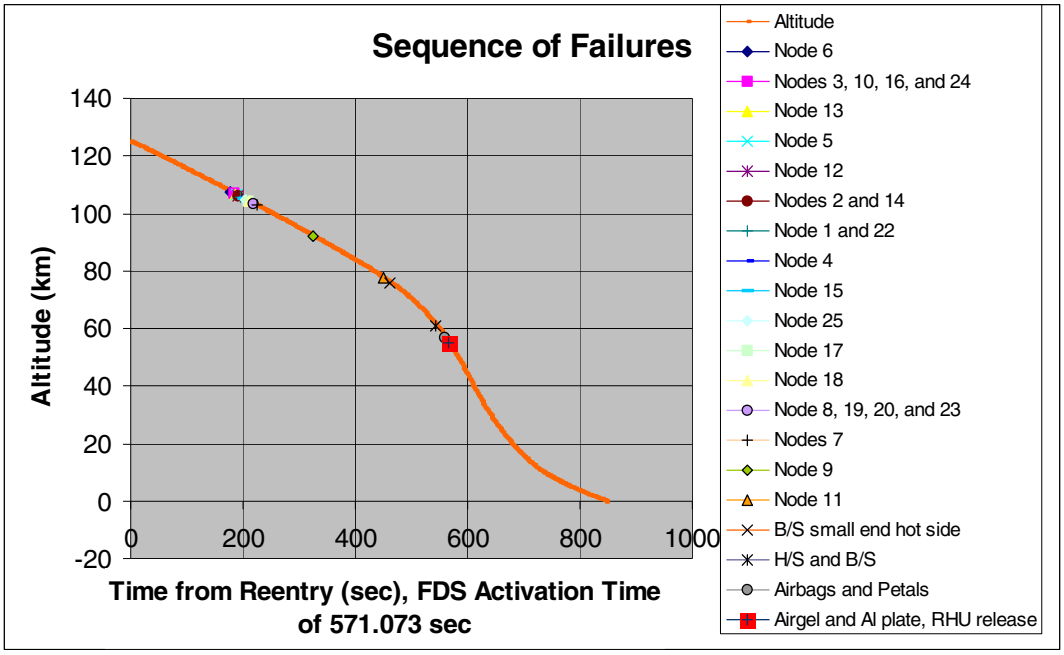
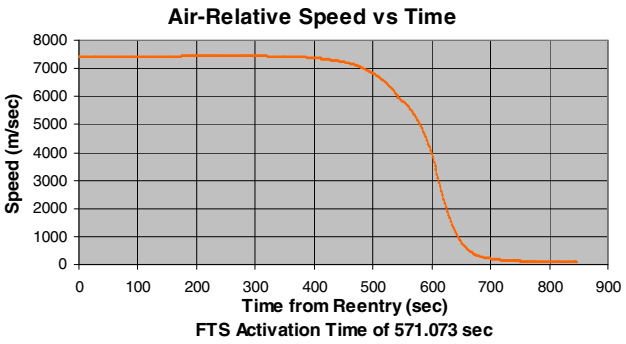


Figure 16. Integrated Heating vs Time of FTS Activation in Suborbital Reentries

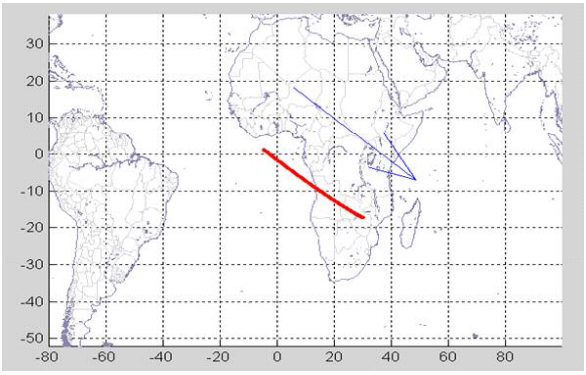
For the suborbital reentry resulting from an FTS activation time of 571.073 sec, the altitude with the sequence of node failures, air-relative speed, and ground track of the spacecraft obtained using the upgraded analysis tool are given in Figure 17. All the nodes failed, and the LWRHU modules were released. The ground impact point of the LWRHU modules was at latitude of -17.39° and longitude of 30.24°, or the northern part of Zimbabwe, Africa. The results of the suborbital reentries at the other FTS activation times are provided in Ref. [65].



(a)



(b)

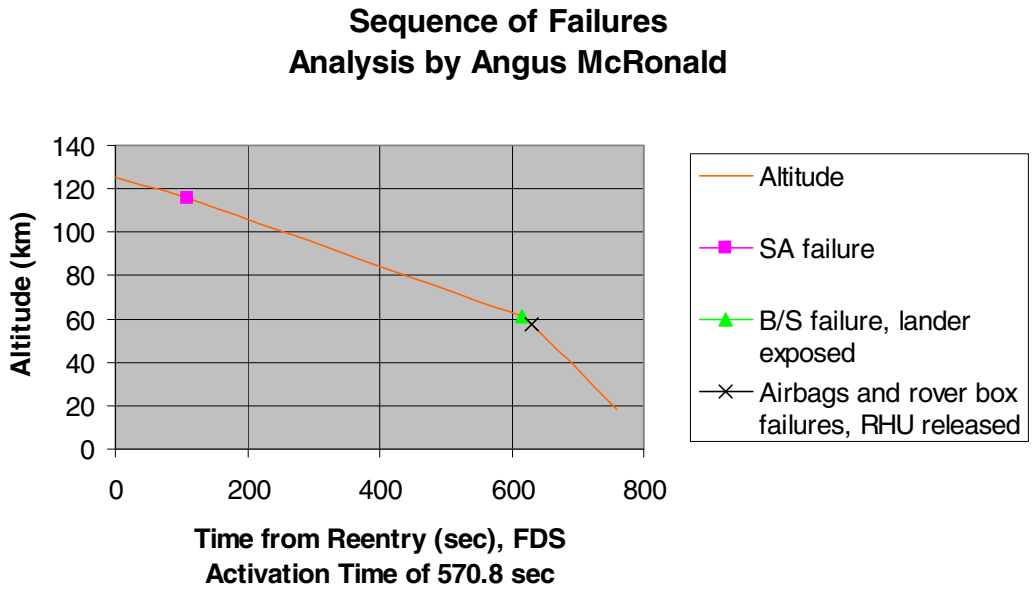


(c)

Figure 17. (a) Vehicle Altitude with Sequence of Node Failures, (b) Air-Relative Speed, and (c) Ground Track at FTS Activation of 571.073 sec

An independent vehicle breakup analysis using the legacy software was performed by Dr. Angus McRonald for MER-A suborbital reentry at FTS activation time of 570.8 sec. The initial condition was based on an older version of the ascent trajectory. The same thermal nodes and failure criteria were adopted in the vehicle breakup analyses performed using the legacy software and the upgraded analysis tool. The sequence of

failures plotted on the altitude time history obtained using the legacy software is given in Figure 18.



Note: Initial condition based on old ascent trajectory
SA is the solar array substrate, or CS Node 10

Figure 18. Independent Vehicle Breakup Analysis Using Legacy Software

The failure times and LWRHU release time produced from the legacy software and the upgraded analysis tool were in close agreement. The differences were due to small differences in the initial conditions based on slightly different ascent trajectories, slightly different FTS activation times, and the software programs. The legacy software did not predict impact point, thus comparisons of impact points from the legacy software and the upgraded analysis tool could not be made.

3.3 Prediction of Impact Points in Out-of-Orbit Reentries

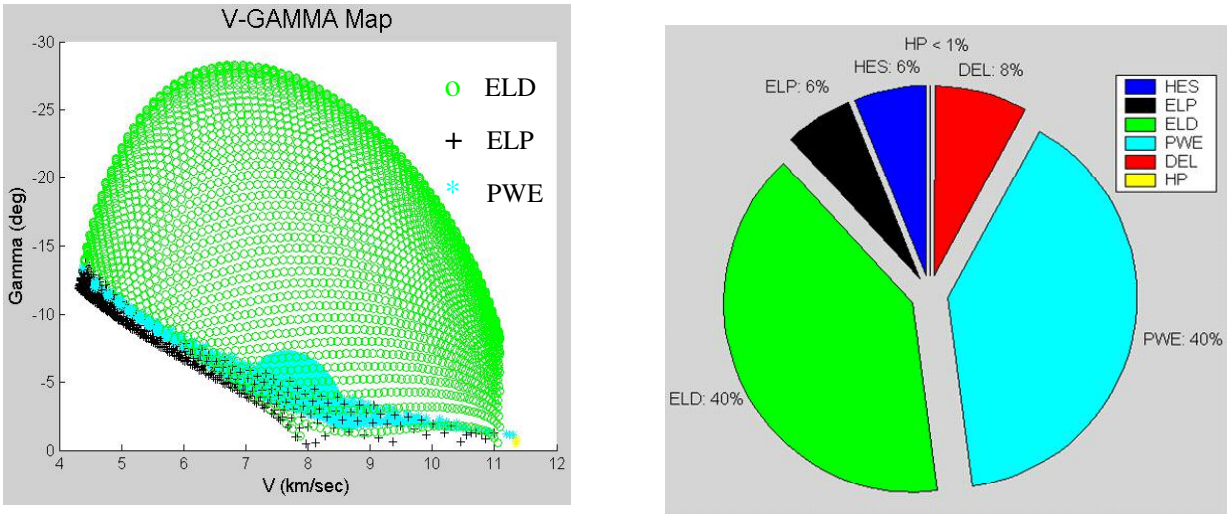
In the vehicle breakup analysis of out-of-orbit entry, the entry conditions and the probabilities of the various types of reentry were obtained from the V-Gamma Map.

Specific cases of out-of-orbit entry were then selected for detailed analysis. In particular, two cases of COD, one delayed elliptic, and one powered entry were analyzed.

The V-Gamma map in the legacy software system provided only entry speed and flight path angle. Thus, the impact point cannot be predicted, and only range relative to the arbitrary entry point can be estimated.

3.3.1 V-Gamma Map

In the vehicle breakup analysis, the V-Gamma Map was used as a pre-processor to provide the initial speed and flight path angle for accidental out-of-orbit reentries, and points about the V-Gamma Map were considered in order to bound the possible reentry scenarios. The V-Gamma Map plots for MER-A and MER-B were similar, thus only MER-A plots for the launch day considered in this analysis are presented. The possible entry speeds and flight path angles for the various classes of reentry trajectories are given in the V-Gamma Map as shown in Figure 19(a). The relative probabilities of the different classes of trajectories are given in the pie graph as shown in Figure 19(b). The departure plane map for the various classes of trajectories as functions of cone and clock angles is given in Ref. [65].



(a) (b)

Figure 19: (a) V-Gamma Map for the MER-A Mission, (b) Relative Probabilities for the MER-A Mission

3.3.2 Circular Orbit Decay

In COD, the time and point of atmospheric reentry would not be accurately predictable until the entry neared. The entry window based on tracking data would then be provided by the Air Force Space Command. For analysis purposes, arbitrary entry points were used for COD. Thus, only ranges, not impact points, were predicted. The initial condition is listed below:

Altitude = 125 km

v_I = 7803 m/sec (v_R = 7385.5 m/sec)

γ_I = -0.2º (γ_R = -0.2113º)

Latitude = 28.3º

Longitude = 0º

Azimuth = 90º

The entry vehicle consisted of the Aeroshell and Cruise Stage. Entry angles-of-attack of 0º and 90º were analyzed. In both cases, all the nodes failed, and the LWRHU modules

were released. For α_{EI} = 0º, the range from entry to surface impact was 6838 km, and 7292 km for α_{EI} = 90º. Thus, a difference of 450 km in range was observed between the two entry orientations.

3.3.3 Delayed Elliptic

A case of delayed elliptic entry was selected at cone and clock angles of 140º and 60º. The initial condition was obtained by propagating with cone and clock angles of 140º and 60º:

Altitude	=	122.68 km
v_I	=	4945.94 m/sec (v_R = 4605.9 m/sec)
γ_I	=	-16.84º (γ_R = -18.13º)
Latitude	=	-25.89º
Longitude	=	39.74º
Azimuth	=	124.79º

For this case, atmospheric entry occurred at 677.12 sec from the beginning of the Stage II restart burn, or 84 sec after the jettison of Stage III. The entry angle-of-attack was 154.36º and assumed to be 180º for simplicity. The entry vehicle consisted of the Aeroshell and Cruise Stage.

The entry flight path angle of –16.84º was relatively steep. Thus, a g-load failure criterion of 30 gees with no heating was also evaluated. The maximum g-load for this reentry was 22.72 gees, and vehicle breakup due to g-load was not assumed. All the CS nodes except for Nodes 9 and 11 failed. The Aeroshell remained intact. The ocean impact point of the Aeroshell with CS Nodes 9 and 11 still attached was at latitude of -27.24º and longitude of 41.98º, off the east coast of Africa.

3.3.4 Powered Reentry

A case of powered entry was selected at cone and clock angles of 90º and -15º. The initial condition was obtained by propagating with cone and clock angles of 90º and -15º:

Altitude = 124.998 km

v_I = 7916.26 m/sec (v_R = 7532.27 m/sec)

γ_I = -1.78º (γ_R = -1.87º)

Latitude = -16.54º

Longitude = 25.25º

Azimuth = 123.23º

For this case, atmospheric entry occurred at 221.44 sec from the beginning of the Stage II restart burn. The nominal post-entry burn time of Stage III was 83.819 sec, and the nominal time to jettison Stage III post-entry was 371.679 sec. The entry angle-of-attack was 78.66º and assumed to be 90º for simplicity. The entry vehicle consisted of the Aeroshell, Cruise Stage, LVA2, and Stage III. The entry mass corresponding to the entry time was 3234.26 kg.

All the nodes failed, and the LWRHU modules were released. The ground impact point of the LWRHU modules was at latitude of -21.62º and longitude of 34.40º, or east coast of Mozambique, Africa.

3.4 Sensitivity Analysis and Footprint Calculation

To generate a footprint, the parametric biases given in Table 7 were applied to the nominal run. To obtain the impact footprint, the array of latitudes and longitudes at surface impact from the parametric analysis without simulations of vehicle breakup was

processed. The following initial condition and vehicle characteristics were used to generate the footprint:

Radius	=	6543489.0 m
Longitude	=	297.71 deg
Latitude	=	24.39 deg
Relative speed	=	6751.99 m/s
Azimuth	=	106.68 deg
Relative flight path angle	=	0.424 deg
Mass	=	1913.93 kg
A_{ref}	=	3.92 m^2
C_D	=	1.25

The 3-sigma (3-σ) impact ellipse is shown in Figure 20 and had the following dimensions:

Semi-major axis	=	76.14 km
Semi-minor axis	=	5.23 km
Azimuth	=	117.2 deg

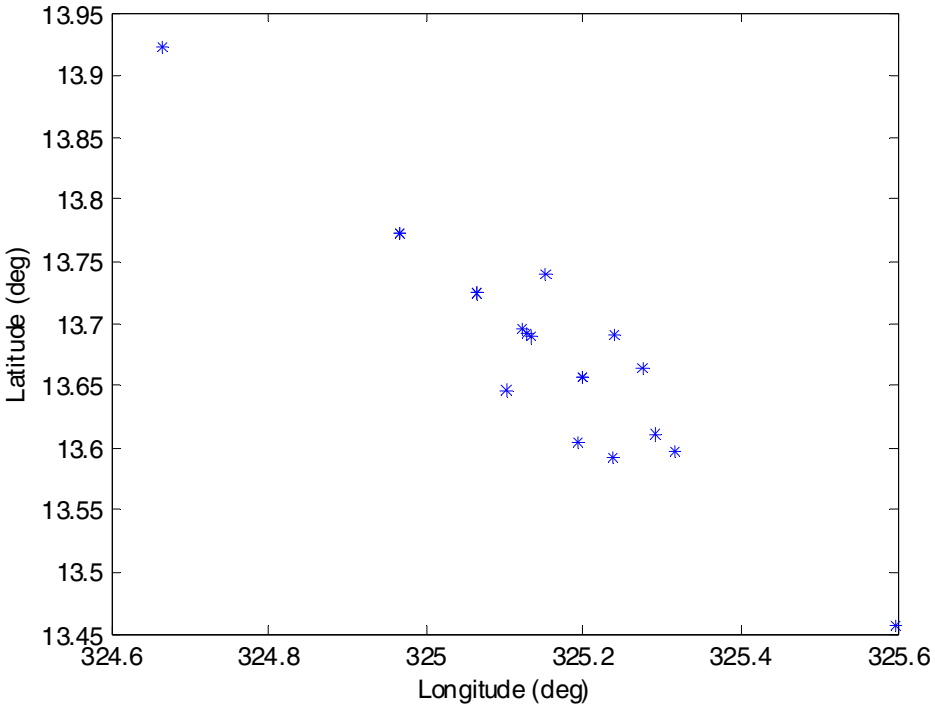


Figure 20. 3-σ Impact Footprint

The legacy software does not predict impact footprint, thus comparisons between the legacy software and the upgraded analysis tool were not made.

3.5 Prediction of Impact Footprint with Effects of Winds

An example wind profile downloaded from the NOAA website is given in Table 10.

Table 10. Example Wind Profile from NOAA Website

PRES	TMPC	DWPC	HGHT	DRCT	SPED
1009.00	14.40	12.30	93.00	180.00	.50
1000.00	15.40	12.40	163.00	200.00	2.10
983.45	16.18	12.01	305.00	260.00	6.70
958.00	17.40	11.40	528.05	270.97	7.07
948.81	16.68	11.46	610.00	275.00	7.20
925.00	14.80	11.60	826.00	285.00	6.70
915.40	14.38	11.53	914.00	290.00	6.70
882.88	12.93	11.27	1219.00	300.00	4.10
850.00	11.40	11.00	1539.00	310.00	3.10
820.89	10.00	9.68	1829.00	305.00	2.10
791.35	8.53	8.29	2134.00	280.00	2.60
777.00	7.80	7.60	2286.23	275.03	3.10
762.74	6.95	6.77	2438.00	270.00	3.60
734.85	5.23	5.09	2743.00	260.00	4.60
707.99	3.52	3.41	3048.00	245.00	6.20

700.00	3.00	2.90	3141.00	245.00	6.20
655.51	-.03	-.26	3658.00	245.00	7.70
630.68	-1.80	-2.12	3962.00	250.00	7.20
606.71	-3.59	-3.99	4267.00	255.00	6.70
561.48	-7.16	-7.72	4877.00	280.00	10.30
540.14	-8.94	-9.58	5182.00	290.00	10.30
500.00	-12.50	-13.30	5790.00	285.00	8.80
480.16	-14.27	-15.52	6096.00	280.00	7.20
444.00	-17.70	-19.80	6687.96	255.76	7.68
442.92	-17.83	-19.94	6706.00	255.00	7.70
400.00	-23.30	-25.60	7460.00	265.00	10.30
391.16	-24.53	-26.90	7620.00	270.00	11.80
324.00	-34.90	-37.90	8968.08	274.40	15.94
315.86	-36.55	-39.49	9144.00	275.00	16.50
300.00	-39.90	-42.70	9500.00	280.00	17.50
251.95	-50.05	-53.61	10668.00	280.00	23.70
250.00	-50.50	-54.10	10720.00	280.00	24.20
201.00	-61.65	-64.85	12098.48	285.00	32.40
200.00	-61.90	-65.10	12130.00	285.00	32.40
198.00	-62.43	-65.63	12192.00	285.00	32.40
197.00	-62.70	-65.90	12223.33	285.00	31.40
170.96	-60.51	-64.65	13106.00	270.00	20.10
155.00	-59.00	-63.79	13716.00	300.00	22.10
150.00	-58.50	-63.50	13920.00	300.00	20.10
140.51	-60.72	-66.08	14326.00	300.00	12.90
125.00	-64.70	-70.70	15052.22	296.04	13.69
121.24	-64.10	-70.10	15240.00	295.00	13.90
114.00	-62.90	-68.90	15618.30	293.40	12.59
107.00	-65.50	-71.50	16006.99	291.76	11.24
100.00	-64.90	-70.90	16420.00	290.00	9.80

where: PRES = pressure (millibar)

TMPC = temperature (ºC)

DWPC = dew point temperature (ºC)

HGHT = altitude (m)

DRCT = direction of wind where 0º is due North (deg)

SPED = wind speed (knots)

Trajectory propagations were performed with the following initial condition and vehicle characteristics, with and without the effects of the wind profile:

Radius = 6503138.0 m

Longitude = 25.25 deg

Latitude = -16.54 deg

Relative speed = 7532.27 m/sec

Azimuth	=	123.23 deg
Relative flight path angle	=	-1.87 deg
Mass	=	3234.26 kg
A_{ref}	=	3.92 m^2
C_D	=	1.25

A difference of approximately 100 meters in range was observed between the simulations with and without the example wind profile, both without the simulation of vehicle breakup. The legacy software does not have the modeling of local winds, thus comparisons between the legacy software and the upgraded analysis tool were not made.

4. Conclusions and Future Work

Vehicle breakup analysis for applications in aerospace nuclear safety had been performed for decades using a legacy software which provided functions for trajectory propagation coupled with thermal and structural analyses and influences. New dynamics modeling and capabilities for the analysis tool have been developed with the objectives to (1) have the capability to predict impact point and footprint, (2) increase the fidelity in the prediction of vehicle breakup, and (3) reduce the effort and time required to complete an analysis. The derivation and verification of these new functions were presented in this dissertation, which included the following:

- Functions to provide the capability to predict impact point and footprint:
  - 3-DOF trajectory propagation for spacecraft translational motion
  - Sensitivity analysis
  - Impact footprint calculation
  - V-Gamma map with non-arbitrary entry points

- Functions to increase the fidelity in the prediction of vehicle breakup:
  - Panel code for the calculation of hypersonic aerodynamic coefficients for an arbitrary-shaped body
  - Modeling of local winds
- Function to reduce the effort and time required to complete an analysis:
  - Node failure criteria calculations

A case study using the Mars Exploration Rover mission was given to demonstrate an improved and more complete vehicle breakup analysis provided by the upgraded analysis tool, and comparisons with results obtained using the legacy software were given wherever applicable. Detailed discussions on the various applications of vehicle breakup analysis, the process of performing vehicle breakup analysis with engineering judgment for contingency planning and launch approval, and some standard derivations of coordinate transformation matrices and 3-DOF equations of motion were given in the appendices.

Future work to further improve the fidelity and facilitate the performance of vehicle breakup analysis includes:

1. Implement Monte Carlo analysis to improve the modeling of uncertainties
2. Incorporate temperature dependence in material properties, e.g. emissivity
3. Automate loading of properties for common materials from database, e.g. aluminum, titanium, stainless steel, copper, graphite epoxy, etc.
4. Improve modeling for thermal analysis
5. Improve modeling for structural analysis

6. Utilize computational fluid dynamics (CFD) to take “snapshots” of the flow field to determine heating and exposure factors for various flight conditions
7. Implement or utilize method(s) to determine aerodynamic coefficients of vehicle in flight regimes below hypersonic

Appendix A. Vehicle Breakup Analysis for Aerospace Nuclear Safety

There have been three U.S. and four known USSR/Russian inadvertent reentries of nuclear powered spacecraft in the history of the space programs, thus demonstrating the need to perform pre-launch vehicle breakup analysis for risk assessment and contingency planning. As seen in Table 11 [1], unrecoverable vehicle malfunction leading to reentry can occur during launch prior to Earth escape, and there were cases that resulted in the release of radioactive fuel. In the first U.S. inadvertent reentry in 1964, the RTG was designed to burn up and disperse its nuclear fuel in the upper atmosphere during accidental reentry, and it performed as planned. Subsequently, the RTGs had been designed for full fuel containment, and as seen in the next 2 accidental reentries, the objective was achieved.

Table 11. Inadvertent Earth Reentries of Nuclear Powered Payloads

Mission	Date	Failure	Result	Nuclear Contamination
Transit 5BN-3 (US for navigation)	Apr 12, 1964	Failure to achieve orbit. Launched by Thorad-DSV2A Able-Star rockets	SNAP-3 RTG burned up during reentry	1800 curies of Pu-238 released in upper atmosphere [1, p. 57]
Nimbus B (US for meteorology)	May 18, 1968	Thorad-SLV2G Agena-D launch vehicle failure. Activation of flight destruct system	RTG recovered intact. Its nuclear fuel later used on Nimbus 3.	Radioactivity not released
LEM 7 (US manned lunar lander of Apollo 13)	Apr 17, 1970	Lunar landing aborted. Apollo 13 spacecraft returned to Earth	RTG undamaged, but lost, during Earth reentry of jettisoned lunar module	No radioactivity measured
Kosmos 556 (USSR for surveillance)	1973	Failure to reach orbit	Reactor burned up during reentry	*Radioactivity measured

Kosmos 954 (USSR for surveillance)	1978	Failure to boost reactor into safe orbit	Reactor burned up over Canada during reentry.	*Radioactivity polluted 124,000 km^2 ground area
Kosmos 1402 (USSR for surveillance)	Jan 23, 1983	Failure to boost reactor into safe orbit	Reactor core burned up over south Atlantic during reentry.	*Radioactivity released
Mars 8 (Russian Mars 96 mission)	Nov 17, 1996	Failure to insert into Mars cruise trajectory	Reentered. Crashed within presumed area covering Pacific Ocean, Chile, Bolivia	Outcome of RTG unknown

* Amount of release not known to author

Mission-ending failures prior to Earth escape are typically due to a malfunction of the launch vehicle. (Spacecraft failures are also considered, but do not contribute significantly to the overall launch-phase failure probability.) Guidance failures, insufficient thrust, failure to ignite a motor, inadvertent payload fairing (PLF) separation, failure to separate the PLF, and explosions of solid or liquid propellant motors are typical contributors. For example, of the 311 launches in the Delta family from 1960 to 2004, 16 were failures or partial failures [38]. The last failure occurred in 1999. On the basis that launch vehicles are not 100% reliable and inadvertent reentries of nuclear power systems have occurred with the release of radioactive material, the necessity of considering inadvertent reentry events as possible contributors to the nuclear risk assessment of these types of space missions is thus well demonstrated. Hence, NASA works to pro-actively assess risks associated with launch and to address all off-nominal reentry scenarios in a lengthy process throughout a mission's life span.

Appendix B. Vehicle Breakup Analysis for Planetary Protection

Aside from aerospace nuclear safety, another application of vehicle breakup analysis is in the planetary protection of the destination planet in a planetary exploration mission, e.g. a mission to Mars. Past track record where two-thirds of all international missions to Mars have failed [67] demonstrates the challenge in landing a spacecraft successfully on Mars. Examples are given in Table 12 of missions which made it far enough to begin EDL, but failed during EDL. Although none of these failed missions used nuclear power system, they serve to illustrate the possibility of planetary contamination if appropriate categorization were not specified and enforced for missions with nuclear-powered payloads.

Table 12. Missions with Unsuccessful Mars EDL

Mission	Date	Failure
Mars 2 (USSR)	Nov 27, 1971	Crash landed due to failure of braking rockets [68]
Mars 6 (USSR)	Mar 12, 1974	Lander failure during EDL [68]
Mars Polar Lander (US)	Dec 3, 1999	Lost spacecraft during EDL [69]
Beagle 2 (UK)	Dec 19, 2003	Lost communication with lander [70]

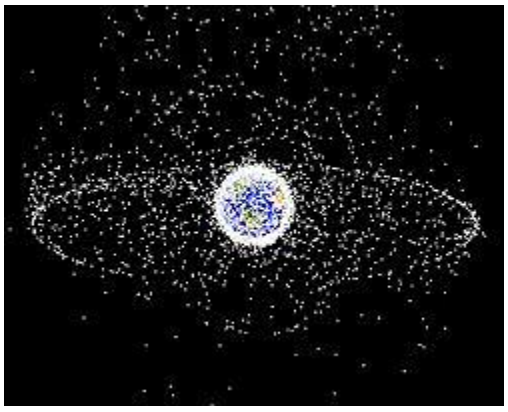
Scientists have discovered Earth microorganisms that are unusually resistant to radiation and desiccation, which would have a decent chance of surviving the interplanetary cruise and to live on the surface of, for example, Mars [71]. Microbes have been found to exist in inhospitable conditions on Earth such as in the Antarctic, miles underground in hot geysers, and in the decontaminated Spacecraft Assembly Facility at JPL, which serves as a portal for the microbes to travel to other planets. In harsh environments, certain microbes have been discovered to draw their nourishment from sulfur, manganese, iron,

petroleum, and even appeared to thrive on aluminum and titanium. Microbes are constantly evolving and adapting to the surrounding conditions. In the case of an unsuccessful entry, descent, and landing (EDL) upon arrival at the destination planet, favorable impact condition in icy regions by an isotopic system may create a liquid-water environment suitable for Earth microorganisms to thrive with the nuclear component as the perennial heat source. Hence, the difficulty in performing EDL at the destination planet and the survivability of microbes in harsh environment make it essential to perform vehicle breakup analysis at JPL for the predictions of impact points and conditions for various EDL failure scenarios. Dependent on the potential contamination as determined by vehicle breakup and impact analyses, NASA then specifies the proper categorization of the mission, to impose an appropriate level of requirements on the spacecraft's organic cleanliness and heat sources for planetary protection.

Appendix C. Vehicle Breakup Analysis for Debris Analysis

C.1 History of Reentries

Of the growing number of man-made hardware orbiting Earth (see Figure 21 [42]), approximately 100 to 200 large objects reenter the Earth atmosphere each year [72]. An atmospheric reentry may be uncontrolled or controlled. An uncontrolled reentry can occur due to orbit decay. If the spacecraft debris survives to reach the Earth surface, the location of the debris footprint is usually random, but may be predictable. For spacecraft of enormous mass, a controlled reentry is necessitated to target the debris footprint towards an uninhabited region, usually located in the ocean, to minimize hazard to humans, properties, and the environment. An uncontrolled reentry can also be due to an unsuccessful launch, e.g. the Shuttle Challenger accident, resulting in the fallback of debris, or a controlled Earth-return reentry that went awry, e.g. the Genesis sample-return mission or the Shuttle Columbia accident.



(Note the high concentration in low Earth orbit and larger population in northern hemisphere. Approximately 95% are debris, e.g. not functional satellites)

Figure 21. Geosynchronous View of Object Population

The majority of the Earth reentries are uncontrolled reentries of rocket bodies, typically launch vehicle upper stage engines and motors (see Figure 22 [42]). Uncontrolled reentries often draw public concern due to the possible associated hazard placed on humans, properties, and the environment. For example, Salyut 7, a Soviet space station with a mass of 40,000 kg, impacted the Andes Mountains in an uncontrolled reentry on February 7, 1991 [73]. In 1978, a Soviet defense satellite went out of control, and its inadvertent reentry left radioactive debris in the Canadian Arctic [73]. Fortunately, there was no report of injury in both cases.



(a) (b)

Figure 22. (a) Delta 2 Second Stage Stainless Steel Propellant Tank Landed in Georgetown, TX, (b) Delta 2 Third Stage Titanium Motor Casing Landed in Saudi Arabia

Examples of relatively recent reentries of satellites are given in Table 13 [72].

Table 13. Past Reentries of Satellites

Satellite	Nationality	Date of Reentry
Raduga	Soviet	May 6, 2004
FWS	China	Dec 18, 2003
Osumi	Japan	Aug 1, 2003
Oko constellation	Soviet	Feb 28, 2002 Feb 4, 2003
OV1	US	Nov 30, 2002
Yantar	Russia	Sep 23, 2002
TUBSAT-N	Germany	Apr 22, 2002
Hete	US	Apr 7, 2002
SIMPLESAT	US	Jan 30, 2002
SROSS C2	India	Jul 12, 2001
ASCA	Japan	Mar 2, 2001

Perhaps the most well-known controlled reentry is that of the Russian Mir Space Station. With a docked Progress M1-5 spacecraft, the total mass of 143,000 kg reentered the Earth atmosphere on Mar 23, 2001 [73]. The 6000 x 500 km footprint was aimed in the South Pacific Ocean between New Zealand and Chile, with a nominal impact point at 47º south latitude and 140º west longitude. Three deorbit burns were performed for the controlled reentry. The first 2 burns were nominal, but the final braking maneuver was an overburn, resulting in a reentry earlier than planned. During the reentry, the station's solar batteries, antennas, and insulation broke away at below 90 km in altitude. The modules became separated 2 minutes later at approximately 74.1 km. Sightings of 5 pieces of the station which were the modules streaking through the sky followed by sonic boom were reported by observers in Fiji island. The actual debris footprint was shifted,

covering just south of Fiji to the upper left corner of the planned impact footprint. There was no report of injury.

Another notable reentry of an enormous spacecraft is the July 11, 1979 reentry of the Skylab space station, with a mass of 69,000 kg [74]. Just before reentry, Skylab was set to tumble end-over-end to reduce the drag to a known level, which made prediction of the impact footprint possible. In the actual reentry, Skylab started to break up later than predicted, shifting the 7400 x 185 km debris footprint to the east by hundreds of kilometers. Debris scattered mostly over the Indian Ocean. The sparsely settled ranch country southeast of Perth in western Australia was showered with pieces of debris, and residents reported hearing sonic booms and whirring noises. However, there was no report of injury or property damage. It was determined later that the error in the breakup prediction was caused by a miscalculation of drag during tumbling by 4%.

C.2 Debris Analysis in the Global Scene

The European Conference on Space Debris was started by the International Academy of Astronautics (IAA) to specifically address the debris and vehicle breakup issues. Numerous organizations worldwide are devoted to monitoring space debris and performing reentry analysis. Selected examples of organizations are provided below.

- The ***NASA Orbital Debris Program Office*** is based in Houston, TX at the Johnson Space Center, and is the lead NASA center for orbital debris research [42]. Its charter is "to conduct measurements of the environment and to develop the technical consensus for adopting mitigation measures to protect users of the orbital environment". Two software tools are used to analyze the reentry survivability of spacecraft components. The Debris Assessment Software (DAS)

is a conservative, lower-fidelity software, and the Object Reentry Survival Analysis Tool (ORSAT) program is a more accurate, higher-fidelity software.

- The ***Center for Orbital and Reentry Debris Studies (CORDS)*** at the Aerospace Corporation was established "to recognize the increasing significance of orbital debris and reentry hazards to space missions" [72]. The company collected over 30 – 40 years of reentry data and developed accurate models and simulation tools for reentry analysis.
- The ***European Space Operations Centre (ESOC)*** of the European Space Agency (ESA) in Darmstadt, Germany, uses the DISCOS database to track all space debris [75].
- The ***Japan Aerospace Exploration Agency (JAXA)*** is conducting research on solutions to the problem of space debris and to enhance the durability of components to endure the severe environment of outer space [76].

Appendix D. Vehicle Breakup Analysis with Engineering Judgment

For reference, the process of performing vehicle breakup analysis and the engineering judgment involved are described in the steps listed below.

D.1 Determine Failure Scenarios from Mission Timeline and Launch Trajectory

The mission timeline specifies major events that occur prior to Earth escape. The launch vehicles commonly used for space exploration include the Delta family and Atlas family. The launch vehicles typically consist of multiple stages, and the major events specified in the timeline include the start and cut-off of burns, jettison of components, spin-up, etc. The launch vehicle's onboard computer has contingency procedures for various failures, but for an unrecoverable vehicle malfunction during ascent, the launch vehicle also has multiple destruct systems to terminate the flight. Each flight termination system (FTS) may have a different method of trigger and operating window. The post-FTS spacecraft configuration may depend on which FTS was activated as well as the time of activation. Note that an unrecoverable vehicle malfunction may not be observable or detected until all the destruct systems have been disabled late in the ascent, resulting in no FTS. An unrecoverable vehicle malfunction can lead to a fallback trajectory due to insufficient energy for the vehicle to be captured into orbit, e.g. suborbital reentry, or a reentry from failure to achieve escape velocity for insertion into interplanetary cruise, e.g. out-of-orbit reentry.

In a launch from Cape Canaveral due east, a majority of ballistic fallbacks prior to parking orbit insertion would lead to impact in the Atlantic Ocean. Only a small subset occurring near the end of the ascent would lead to impact on Africa or even the Indian

Ocean. The cases leading to impact in Africa are of particular interest for the obvious reason of public safety concerns. During the last few seconds at the end of the ascent before engine cut-off, the vehicle achieves orbital energy, and thereafter the destruct systems are disabled and accidental reentry would be out-of-orbit.

For the analysis of out-of-orbit reentries, a spectrum of reentry conditions can be derived from the assumptions of (1) steady misaligned burns, or SMB, where the thrust misalignment is defined by the cone and clock angles, and (2) an otherwise nominal, time-delayed sequence of burns while in parking orbit. The cone angle is measured in the yaw plane with 0º as the nominal burn, and the clock angle is about the roll axis such that a yaw of 90º and roll of 90º would yield a vertically upward thrust. The burn sequence is specified by the initial conditions of the parking orbit, the engine specific impulse (Isp) of each burn, the durations of the burn and coast sequences, and the mass of the spacecraft before and after each burn/coast sequence. Depending on the misdirected burn, the spacecraft would be propelled into a specific orbit, with atmospheric reentry as a possible outcome of the SMB. This failure scenario may not be highly probable, but it provides an envelope which encompasses everywhere that the vehicle can get to, given the onboard fuel. The possible outcomes of the SMB fall into the following categories [39]:

1. Hyperbolic escape (HE): For this subset of SMB, the spacecraft has reached hyperbolic speed and achieved an interplanetary trajectory, and thus is not on a path that reenters the atmosphere. HE includes the desired special case of being on the correct interplanetary trajectory as well as being on off-nominal interplanetary trajectories. About 5% - 30% of SMB maps to a hyperbolic escape.

2. Orbit decay reentry (DEL): For this subset of SMB, the perigee of the final orbit is above the atmosphere, so that reentry occurs after a period of orbit decay. Less than 10% of SMB maps to an orbit decay reentry.
3. Powered reentry (PWE): For this subset of SMB, the reentry occurs while the burns are in progress, and the spacecraft has not separated from the launch vehicle. About 40% - 50% of SMB maps to a powered reentry .
4. Prompt reentry (ELP): For this subset of SMB, the burns have finished prior to reentry but the vehicle is then on a downward path approaching a perigee within the atmosphere. Less than 10% of SMB maps to a prompt reentry.
5. Delayed reentry (ELD): For this subset of SMB, the vehicle is on an upward path at the end of the burns and will reenter the atmosphere after passing though an apogee. About 40% - 50% of SMB maps to a delayed reentry.
6. Prompt hyperbolic reentry (HP): For this subset of SMB, the vehicle has an escape speed but will reenter the atmosphere and may exit and fall into the HE or ELD categories. Less than 1% of SMB maps to a prompt hyperbolic reentry.
7. Circular Orbit Decay (COD): The spiral case of COD is due to failed burns from parking orbit. Reentry may occur one or two weeks later. With a shallow reentry angle, there may be multiple skip-outs before the spacecraft is captured into atmospheric reentry, and the COD reentry is after the skip-outs are all done. The reentry is similar to DEL. The COD is a single point at near circular orbit speed with near zero flight path angle.

The pairs of reentry speed (V) and flight path angle (Gamma) are plotted to generate the V-Gamma map. Note that the hyperbolic escape and orbit decay reentry

categories will not appear on this map. In the orbit decay reentry category, typically the initial elliptical orbit will eventually decay into a circular orbit, and then continues as a COD which is represented by a single point on the V-Gamma map. The COD reentry is a monotonic case where the speed is the circular orbit speed less 10 or 20 m/s and the gamma is slightly less than 0, e.g. -0.3º. However, in the case of a highly elliptical orbit, reentry near perigee may occur prior to achieving circular orbit due to orbit decay. In a COD or elliptical orbit decay, the entry point and time of entry are arbitrary, thus only impact point relative to the assumed entry point can be predicted. The relative probabilities for the categories of SMB outcome are illustrated on a pie graph. A mission to explore an outer planet which requires higher launch energy will display a higher percentage for the hyperbolic escape in its pie graph compared to that of a mission to explore an inner planet.

Note that the points within the V-Gamma map are not restricted to the SMB failure scenario; for example, the outcomes of partial burns and no burn are also points within the V-Gamma map. Therefore, a given V-Gamma pair within the map may correspond to multiple failure scenarios, and thus the entry point is not unique. However, the points about the V-Gamma map (on the boundary of the V-Gamma map) are restricted to the SMB failure scenario. For each point about the V-Gamma map, a non-arbitrary entry condition can be determined and associated with it is a specific impact point which can be predicted through trajectory propagation with breakup analysis.

The accident initial conditions (AIC) that are contributors to various accident outcome conditions (AOC) are provided. For example, an attitude control malfunction may be a contributor which occurs during the ascent as the AIC, and the resulting AOC

may be the activation of the Command Destruct System (CDS) and a suborbital reentry of the spacecraft released from the destructed launch vehicle. Another example is a Stage II liquid rocket engine (LRE) catastrophic failure which may be a contributor occurring while in the parking orbit as the AIC, and the AOC is no FTS and an out-of-orbit reentry of the spacecraft alone. The various contributors resulting in particular AIC and AOC have different probabilities of occurrence.

D.2 SetA ssumptions to Bound Failure Scenarios

Given the large number of possible failure scenarios, it is not necessary to examine all of them for risk assessment. Therefore, assumptions are set to bound or simplify the failure scenarios while yielding a thorough analysis. For preliminary vehicle breakup analysis, the following assumptions can be made whenever applicable:

1) A mission-ending failure consisting of multiple independent malfunctions is not credible and therefore not considered.
2) For a first-order approximation, incremental velocity from the FTS activation is neglected.
3) Following FTS activation, the released spacecraft is tumbling due to uneven and asymmetric forces from the FTS, and damage to the spacecraft is negligible.
4) For a first-order approximation, temperature-dependence in material properties, e.g. emissivity, is not considered.

For the analysis of suborbital reentries, thrust cessation with FTS activation can be used as a representative failure scenario. With the assumption that deviation of the trajectory from nominal is negligible, the initial condition can be extracted from the ascent profile. An array of FTS activation times is assumed at various points along the

ascent trajectory, with higher concentration of cases towards the latter part of the ascent where impact in Africa is the likely outcome. The resulting reentry vehicle configuration is dependent on the outcome of the FTS activation since each destruct system may affect different parts of the launch vehicle. For example, the Stage III Star 48 Motor has a separate destruct system consisting of two conical shaped charges. The activation of this destruct system may leave only the end dome of the motor attached to the spacecraft as the reentry vehicle. Without the activation of the shaped charges, the launch vehicle's destruct system would leave an almost intact Star 48 motor attached to the spacecraft as the reentry vehicle. Therefore, it is necessary to determine if and which destruct system(s) is activated in a failure scenario. Considering that the FTS was activated, a tumbling reentry vehicle would be the only attitude examined with the assumption that the forces from the FTS are uneven and asymmetric.

For the analysis of out-of-orbit reentries, typically a set of "cardinal points" consisting of 12 or 13 V-Gamma pairs at the boundary of the V-Gamma map is selected for analysis. The points about the V-Gamma map are the limits of reentry conditions under the SMB failure scenario and consist of various categories of reentry including the prompt reentry, delayed reentry, powered reentry, and COD. The cardinal points form an entry ellipse, and associated with it is a bounding impact footprint which also envelops the impact points of the various failure scenarios corresponding to the points within the V-Gamma map. The cardinal points include:

1) V_{max}, γ_{max} for steepest entry
2) $V_{parabolic}$, γ_{max} at the top of the V-Gamma map for steepest entry at parabolic speed (can be as steep as -90º)

3) V_{min}, γ_{min}

4) V_{min}, γ_{max}

5) $V_{parabolic}$, γ = -5° for high integrated heating case

6) COD

7) PWE with V_{min} for retrograde burn that generates opposing velocity

8) PWE with V_{max} for posigrade burn that adds to velocity

9) PWE with medium V

10) Additional points to produce a fairly even distribution of points about the V-Gamma map

The initial vehicle configuration is determined by the reentry time. For example, if the launch vehicle has multiple stages to perform burns while in the parking orbit, e.g. Stage II and Stage III, the vehicle in a powered reentry may enter the atmosphere under the following scenarios:

1. During the Stage II burn in which the reentry configuration would be spacecraft + Stage III with full propellant + Stage II burning with partial propellant
2. During the coast between Stage II and Stage III burns in which the reentry configuration would be spacecraft + Stage III with full propellant. The empty Stage II may also be attached depending on if the reentry time is before or after staging. The Stage III burn may be initiated post-entry in the nominal, timed burn sequence, if not inhibited by reentry heating and/or forces.
3. During the Stage III burn in which the reentry configuration would be spacecraft + Stage III burning with partial propellant.

The mass of the remaining propellant in the burning engine/motor in scenarios 1 and 3 above can be calculated given the reentry time relative to the initiation of the burn and the rate of fuel consumption. The reentry angle-of-attack (α_{EI}) in a powered reentry is obtained as part of the V-Gamma map calculations. For the other reentry categories, the reentry attitude is arbitrary. Therefore, the representative vehicle attitudes typically examined are reentries with the vehicle face-on ($\alpha_{EI} = 0^{o}$), end-on ($\alpha_{EI} = 180^{o}$), side-on ($\alpha_{EI} = 90^{o}$), and tumbling. Note that there may be different tumbling modes. The entry attitude determines the vehicle ballistic coefficient and the exposure of the vehicle components to the flow, thus affecting the trajectory, the breakup sequence, the release of the GPHS modules or LWRHU, and the impact point.

Potential failure scenarios that are major contributors to suborbital and out-of-orbit reentry accident outcome conditions (AOCs) are also examined. Although the suborbital and out-of-orbit reentries mentioned above are representative and bounding cases, they do not necessarily correspond to the major initiating failure contributors to suborbital and out-of-orbit AOCs. As an example for suborbital reentry, the loss of attitude control during the second stage first burn is the primary failure leading to a command destruct action with a nearly intact STAR 48B motor and intact spacecraft as the reentry body. A loss of attitude control and a stage II liquid rocket engine catastrophic failure are the two major failure events leading to an out-of-orbit reentry, with both contributing about equally to this AOC.

D.3 Determine Spacecraft Configuration and Select Thermal/Force Nodes

From the detailed drawings of the spacecraft, the location(s) of the nuclear-powered system can be identified. The nuclear-powered system may be embedded inside

other components, e.g. an LWRHU buried inside the MER rover, or it may be a protrusion on the spacecraft, e.g. an RTG attached to the bus as in the Ulysses spacecraft.

The spacecraft consists of a multitude of components from which thermal/force nodes are selected for failure criteria calculations to form an expected sequence of failure leading to the release of the nuclear component. The components of interest in the breakup analysis are typically points of weakness in the spacecraft that are more likely to fail, and not components embedded or attached to large heat sinks. Furthermore, the components of interest are those where (1) a failure will cause a significance change in the spacecraft configuration or ballistic coefficient, and thus change the course in the spacecraft trajectory, or (2) a failure will cause a significant change in the exposure of other components to the flow, and thus affects the sequence of breakup. An example is the failure of a fuel tank carrying a large amount of liquid propellant which may not cause the drag coefficient to change significantly, but will result in a considerable reduction in the spacecraft mass. Another example is the failure of the solar array on the cruise stage since it will cause a significant change in the spacecraft mass, aerodynamic drag, and the exposure of other components to the flow. The thermal blanket which usually covers a large surface area of the spacecraft is typically the first to fail, and its failure will change the exposure of other components to the flow.

The thermal/force nodes selected for failure evaluation are not necessarily components of large mass or size, but may be relatively small objects serving as supports, such as struts, cables, brackets, nuts, and bolts. For example, the failure of the struts that support the star scanner will cause a notable mass reduction, not due to the loss of the struts, but due to the loss of the star scanner. It is necessary to determine how a

component is attached to the spacecraft, e.g. bolted down or welded, since that may affect the failure criteria. In the spacecraft drawings, certain supports may not be obvious or even shown. Therefore, discussions with the structural and design engineers to obtain such information will be required.

Large components such as the heatshield and backshell of an aeroshell are often joined together by pyrotechnic devices. The activation of the pyrotechnic devices when the autoignition temperature is reached will cause the large components to separate. The locations of the pyrotechnic devices are typically designed in a manner where they are well hidden from the flow and embedded in the large components, which act as heat sinks. Therefore, autoignition may not be likely, and pyrotechnic devices can usually be neglected in a preliminary analysis.

A component is typically made of uniform material. If a component is made up of multiple materials, then either the component can be divided into multiple nodes, each of uniform material, or the averaged material properties can be used for the component modeled as a single node to simplify the problem. An example is the thermal blanket consisting of multi-layers of different materials. The thermal blanket can be divided into multiple nodes where each node consists of consecutive layers of the same material, or the effective material properties for all the layers can be calculated to model the thermal blanket as a single node.

D.4 Collect Information on Node Physical and Material Properties

Once the thermal/force nodes are identified, the physical properties of the nodes are obtained from the detailed drawings and mass breakdown of the spacecraft to describe the characteristics of each node such as its shape, size, thickness, material type,

and mass. Given the material that makes up a node, the material properties can be obtained from material handbooks. Examples of materials commonly used in spacecraft components include aluminum, titanium, graphite epoxy, stainless steel, carbon-carbon, and copper [40]. For example, the RTG housing is typically made of aluminum. For materials not found or difficult to find in handbooks such as aerogel (solid insulator), vectran (liquid crystal polymer fiber), and SIRCA (thermal shield material), the materials engineer should be consulted to obtain the material properties.

To calculate the temperature of a thermal node during a reentry simulation, the material thermo-mechanical properties needed include the material emissivity, density, specific heat, and thermal conductivity. Other node physical properties needed for the calculation of node temperature include the areas subject to convective, radiative, and conductive heat transfer, and the path length of heat conduction. Note that for some materials, there is difficulty in determining parameters at elevated temperatures beyond the normal range of usefulness. For the assessment of node failure, the material melting temperature can be used for failure evaluation such that breakup is delayed as compared to using a lower failure temperature. This is a conservative approximation since a component typically will break up before reaching the melting temperature due to g-load as the material strength is weakened while the component gets heated.

A liquid propellant fuel may fail due to the burst pressure or the burnout flux being exceeded. Typically, the tank is made of titanium, and the liquid fuel is hydrazine. To evaluate tank failure due to excessive internal pressure, the tank operating and burst pressures are obtained. The material properties needed include the liquid-dependent coefficients for the calculation of vapor pressure of the liquid fuel, the percentage of

room temperature tensile yield strength of the tank material, specific heats of the tank material and liquid fuel, and emissivity of the tank material. Other tank physical properties needed include the tank and liquid fuel masses, and the tank surface area normal to the flow. To evaluate tank failure caused by exceeding the burnout flux, the material properties needed of the liquid fuel include the enthalpy of vaporization, density of saturated vapor, surface tension of liquid-vapor, and density of saturated liquid.

D.5 Make Assumptions for Missing Data Based on Engineering Judgment

The detailed drawings and mass breakdown of the spacecraft may not contain all the information needed for the calculation of aerodynamic loads on the nodes or the failure criteria. Examples of the physical properties of components that may not be specified in the detailed drawings or mass breakdown are the material type and thickness. Other pieces of information that may be missing include how a component is attached to the spacecraft, e.g. welded or bolted down, and the operating and burst pressures of a liquid propellant tank. Occasionally, discussions with the design engineers to obtain the missing information may provide only estimates. This is especially true if a preliminary vehicle breakup analysis is requested during the early phases of the mission design and analysis before the spacecraft design matures. It is then necessary to make assumptions for the missing data using typical values from past missions in order to proceed with the breakup analysis. Certain components are almost always made of the same material in past missions, e.g. the liquid propellant tank is typically made of titanium. Other components may have wide variation of materials, e.g. struts may be composed of aluminum, titanium, stainless steel, or composite tubes. For these components, aluminum can be assumed since it is the most commonly used material in a spacecraft.

Assumptions made for the missing data should be clearly stated in the final report, and the analysis results are valid within these assumptions. Note that in the breakup analysis, the properties of massive and significant components are usually known, even during the preliminary design phase. Thus, the predicted breakup sequence and outcome of the reentry usually will not be significantly different if the assumptions made for missing data are incorrect, e.g. a strut assumed to be composed of aluminum is actually made of titanium, or its thickness is actually 10% more than the assumed value. Sometimes the failure of a strut will depend comparatively little on the material and thickness, and the time and altitude of the failure will change only slightly. As the spacecraft design evolves and becomes more mature during the latter phases of the mission design and analysis, some of the data which were missing will become available to perform the detailed breakup analysis.

D.6 SetE xposure Factors

The thermal load on a node depends greatly on the exposure of the node to convective heating from the flow, which is described by the exposure factor (EF). The exposure of the node to the flow depends on the vehicle reentry attitude, e.g. flying forward or face-on, backward or end-on, side-on, tumbling side-over-side, or tumbling end-over-end. Therefore, the exposure factor of a node is specified for each vehicle reentry attitude. For random tumbling, an average can be taken of tumbling side-over-side and end-over-end.

A vehicle flying forward, backward, or side-on may begin tumbling when certain components break up. For example, when the aeroshell flying forward or backward fails, the released content such as a rover may begin to tumble. An aerodynamically stable

vehicle flying at an attitude other than trim or tumbling slowly upon reentry may re-orient itself due to the stabilizing moment, resulting in the heavy end flying forward. The vehicle reentering from out-of-orbit may be spinning upon reentry if the spin-up sequence occurred nominally while in the parking orbit, giving it aerodynamic stability. As components begin to break off, the spinning vehicle may not begin to tumble due to the aerodynamic stability, but may begin coning.

A node fully or directly exposed to the flow is given an exposure factor of 1, and an exposure factor of 0 means the node is completely hidden from the flow. A partial exposure to the flow would yield an exposure factor between 0 and 1. The exposure factor of a node can be adjusted based on engineering judgment to account for its location on the spacecraft and its position relative to other components. The exposure factor has direct impact on how quickly the node temperature builds up; the higher the exposure factor, the faster the node temperature rises. Once a node fails, the components that were shielded by the node will have increased exposure to the flow.

D.7 Determine Failure Criteria

The vehicle is subject to aerodynamic loads during the accidental reentry, and a component may fail by melting, or by breaking away from the vehicle, or by a combination of the two. The component failure may occur due to thermal load alone, e.g. the failure of thermal blanket early in the reentry; it may be due to structural load alone, e.g. the failure of the content in the aeroshell hidden from the flow but subject to g-load; or it may be due to combined thermal and structural loads, e.g. the failure of the RTG housing exposed to the flow.

In the evaluation of thermal node failure, two approaches can be taken:

1. In one approach, the node temperature is calculated during the reentry simulation by modeling the node as a simple shape, such as a slab, a hollow cylinder, or a hollow sphere [41]. For example, the solar array is modeled as a slab; a strut is modeled as a hollow cylinder; and a liquid propellant tank is modeled as a hollow sphere. The node is assumed to be either a good or poor conductor, and time integration of the convective and radiative heat transfer rates over the applicable surface areas is performed with consideration for the exposure factor [41]. Note that the convective heating on a node is related to the reference stagnation point heating by a heating factor defined by the geometry of the node, and cold wall is assumed in radiative cooling. Other options exist to model heat conduction between the front and back halves of the node, or between layers in a three-layered node. For failure due to thermal load, the node temperature is evaluated against the node failure temperature during the reentry simulation, and once the failure temperature is exceeded, node failure occurs.
2. In the second approach, given the node properties and exposure factor, the heating required to reach the failure temperature can be calculated from the material specific heat. The calculation assumes perfect conduction within the node, but does not account for conduction to other nodes. Radiative cooling can be approximated, but is generally not considered until the first round of simulation run is made to approximate the time duration of the heat-up or melting phase. The heating to reach failure temperature is then adjusted by a heating factor to relate to the integrated reference stagnation point heating (Q_{ref}) to yield the failure integrated heating (Q_{fail}) for the node. For failure due to thermal load, Q_{ref} is

evaluated against Q_{fail} during the reentry simulation, and once Q_{fail} is exceeded, node failure occurs. Note that in this approach, Q_{fail} is given relative to Q_{ref}. Therefore, a higher exposure factor will yield a lower Q_{fail}, such that less time is required for Q_{ref} to reach the Q_{fail} value for an earlier failure, consistent with what is expected from the higher exposure factor. In this approach, the Q_{fail} of a node is dependent on the vehicle attitude and is dictated through the exposure factor.

In general, the second approach is used to calculate the failure criteria of various nodes to form the expected sequence of failure and to perform preliminary breakup analysis. The first approach is used for higher-fidelity breakup analysis.

During the early phases of the mission design and analysis, the maximum g-load for the spacecraft or the internal content of the aeroshell may be provided. In the trajectory simulation, the trajectory g-load is then evaluated against the maximum g-load for the determination of force node failure due to structural load. During the latter phases of the mission design and analysis, the 3 components of failure g-loads in the body frame for various supports such as struts, brackets, etc., are provided. For the assessment of failure, the 3 components of g-load for a force node are calculated during the trajectory simulation and evaluated against the failure g-load components. Once one of the failure g-load components is exceeded, node failure occurs.

The thermal failure criteria derived based on the failure temperature, e.g. melting temperature, is applicable in the absence of structural loads. Similarly, the failure g-loads are applicable in the absence of thermal loads. For the assessment of failure due to combined thermal and structural loads, the thermal and structural failure criteria can be combined to form a linear function. An example is given in Figure 23 where the linear

function is formed using a failure integrated heating of 780 J/cm^2 and a failure g-load of 20 gees. At a given reference integrated heating during the trajectory simulation, node failure occurs if the trajectory g-load exceeds the corresponding failure g-load obtained from the linear function for the node.

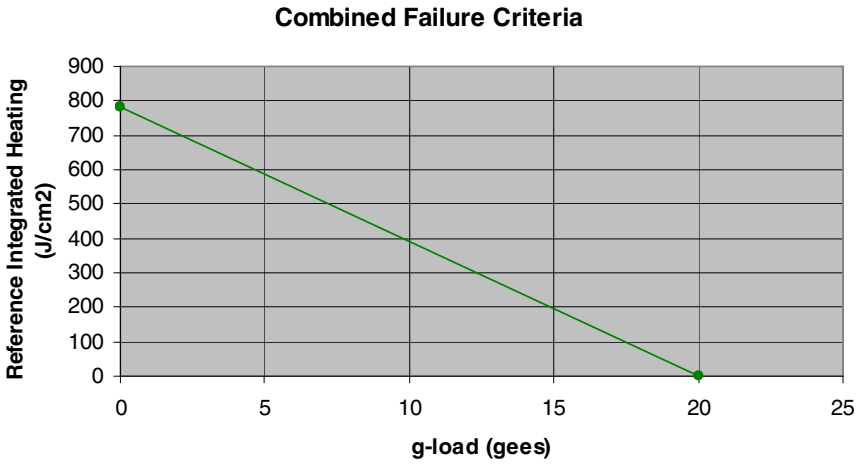


Figure 23. Combined Failure Criteria

D.8 Determine Expected Sequence of Failure

The sequence of failure in the spacecraft components leading to the release of the GPHS modules or LWRHU during an inadvertent reentry may not be obvious at first. Therefore, the failure criteria for various components are determined, and are the basis in forming an expected sequence of failure. The order that components break up is dependent on the vehicle attitude. Therefore, a different expected sequence of failure is formed for each reentry attitude.

Upon identifying a node, it is useful to list the different ways that the node may fail. For example, a hydrazine tank may fail (1) when the burnout flux is reached, (2) when the internal pressure exceeds the burst pressure, or (3) if the brackets holding the tank to the vehicle breaks or melts. It may not be obvious which of the 3 failure criteria

will occur first during an accidental reentry. Therefore, all 3 failure criteria will need to be evaluated to determine the one that occurs the earliest, which is then used as the criterion for tank failure. If the tank separates from the spacecraft, the result brings a change in mass and possibly in spacecraft attitude.

An LWRHU may be embedded inside other components such that those components will need to fail in an "onion-peeling" order before the LWRHU is released. An example is an LWRHU embedded inside a rover. The aeroshell needs to fail first to expose the rover to the flow, and the rover panel has to fail to expose the embedded LWRHU for release. Additional layers consisting of other components may exist, depending on the design, such as lander, airbag, rover wheels, etc.

Based on the failure criteria calculated for the nodes and the spacecraft configuration, an expected sequence of failure can be formed. Determining the fate of the nuclear component is the primary objective. Therefore, the outcomes of the components that break off of the vehicle after the release of the nuclear component are not of concern (unless a debris analysis is requested). It may be that a component is determined to fail after the release of the nuclear component, and thus does not become a part of the expected sequence of failure. The expected sequence of failure is formed based on the thermal failure criteria. Once the trajectory simulation is performed and the g-load is calculated in the simulation, the expected sequence of failure may need to be updated as the consideration of structural failure criteria may change the breakup sequence of the nodes.

D.9 Determine Ballistic Coefficients of Various Spacecraft Configurations

The initial spacecraft configuration at atmospheric reentry is dependent on the failure scenario leading to the reentry. For example, if the FTS is activated, a significant portion of the launch vehicle will be destroyed and therefore not a part of the reentry vehicle. If staging occurred nominally while in the parking orbit, an accidental reentry would involve only the spacecraft as the reentry vehicle with arbitrary attitude. If tumbling occurs while in the parking orbit and the contingency procedure prevents engine/motor ignition and staging, the tumbling reentry vehicle would be the spacecraft with the engine attached and non-thrusting. The contingency procedures may be mission dependent and need to be considered with the failure scenario to determine the initial reentry configuration and attitude.

The subsequent spacecraft configuration and attitude following each failure can be determined for the expected sequence of failure developed for each reentry attitude. For each spacecraft configuration and attitude, the mass, drag coefficient, and reference area are needed for trajectory propagation. Once a node fails, the mass of the new configuration is obtained by subtracting the mass of the failed node. The C_D and A_{ref} may also need to be updated for the new configuration if the failure of the node has changed the aerodynamic characteristics of the vehicle notably. A Newtonian code developed based on Newtonian theory in fluid mechanics is available to calculate the hypersonic static aerodynamic coefficients as a function of angle-of-attack. As a quick approximation, subsonic drag coefficient can be assumed to be half the hypersonic value. For a tumbling vehicle, the average C_D can be used. Lift is generally assumed to be negligible, especially in a tumbling vehicle where lift averages out to zero.

D.10 Predict Vehicle Breakup and Outcome of Nuclear Component

Trajectory simulation is performed for the prediction of vehicle breakup and outcome of the nuclear component. The atmospheric reentry altitude is assumed at 120 km. Once a node failure is determined, the simulation is interrupted; updates to the vehicle mass, C_D, and A_{ref} are made; and the simulation is then resumed. Typically, once a component which does not carry the nuclear component breaks away, its trajectory is no longer tracked unless debris analysis is requested. In a debris analysis, the outcome of the separated component is determined by continuing the propagation of the trajectory with modeling of ablation. Multiple trajectory simulations are performed to cover the large spectrum of failure scenarios during ascent and while in the parking orbit. From the simulation results, the probabilities for the release of the nuclear component can be determined for suborbital and out-of-orbit reentries.

An object in a ballistic, free flight will converge towards its terminal velocity, which is achieved when its drag acceleration cancels the gravitational acceleration in a downward trajectory (γ = -90º). The terminal velocity of an object is obtained by:

$$\sqrt{\frac{2C_B g_{Earth}}{\rho_\infty}} \tag{75}$$

where ρ_∞ is the freestream density which decreases exponentially with increasing altitude. The reentry speed of a vehicle is significantly greater than its terminal velocity, thus the vehicle will slow down through drag by dissipating its energy in the form of heat. As the forward momentum of the vehicle decreases, its flight path also becomes steeper, until terminal velocity condition is achieved. As the formula for terminal

velocity suggests, the vehicle's ballistic coefficient has a direct impact on its trajectory such that a higher ballistic coefficient will cause the vehicle to:

1. Maintain its horizontal velocity longer, which may result in a more shallow flight path angle at surface impact
2. Travel further in range
3. Reach the surface sooner
4. Not decelerate as much
5. Have higher terminal velocity, resulting in higher impact speed.

In a suborbital reentry, the vehicle will continue on an upward path following launch failure but will eventually return in a fallback trajectory due to insufficient energy to capture into orbit. The heating accumulated during the upward path is assumed to dissipate into space while the vehicle is temporarily above the atmosphere before returning in the fallback trajectory. Therefore, the integration of heating for breakup analysis will not begin until reentry begins at 120 km. For a launch failure occurring early in the ascent, the vehicle may not exit the atmosphere before beginning the fallback trajectory. In this case, the integration of heating for breakup analysis will begin following the launch failure. Note that the integrated heating during the upward path of the trajectory is only a small percentage of the final integrated heating and does not contribute significantly to the outcome of vehicle breakup whether it is considered or not.

Smaller components or sharp edges facing the flow receive higher heating rate and are typically the first to fail, e.g. a cylindrical strut with small radius. Larger components or blunt shapes are subject to lower heating rate and take longer to fail, e.g. heatshield of blunt shape with large nose radius.

A shallow reentry such as in a COD will incur large integrated heating with minimal g-load, hence increasing the likelihood of vehicle breakup and the release of the nuclear component due to thermal loads. The time for the vehicle to reach the Earth surface in a shallow reentry is prolonged, thus radiative cooling becomes significant and should be modeled in the calculation of failure criteria and the trajectory simulation. For a steep reentry, integrated heating is reduced and the g-load becomes significant. The reduced time for the vehicle to reach the Earth surface allows the radiative cooling to be assumed negligible.

Spacecraft components made of aluminum which has relatively low melting temperature are inclined to ablate at high altitude and not reach the Earth surface. The breakup of a larger or sturdier vehicle/component usually occurs at lower altitudes. Components made of materials such as titanium, stainless steel, or carbon-carbon have high melting temperature and will likely ablate at lower altitude or survive to impact the surface.

D.11 Perform Sensitivity Analysis and Calculate Impact Footprint

The predicted breakup sequence is accurate within a range of uncertainties, thus the impact point is bounded by a footprint defined by semi-major axis, semi-minor axis, and azimuth. The uncertainties result from unknowns associated with the launch failure due to limitations on the observables, thus sensitivity analysis is performed to generate the envelope of impact points given the uncertainties. In the event of an accidental reentry, the reentry conditions are derived from tracking data with relatively small uncertainties, whereas the reentry configuration is typically predicted with less accuracy. Therefore, small parametric biases are applied to the initial condition such as entry speed

and flight path angle, and vehicle data including reentry mass, C_D, and A_{ref} are given larger dispersions for downtrack variations. For crosstrack variations, lift-to-drag ratio (L/D) with non-zero bank angle and effects of local wind are applied. To enhance the accuracy of the footprint prediction, real-time local wind profiles downloaded from the National Oceanic and Atmospheric Administration (NOAA) website [43] are used in lieu of synthetic wind models. The NOAA wind profiles are updated every 12 hours for various stations worldwide and are available to the general public.

For an analysis where the incremental velocity from the FTS activation was neglected, an incremental velocity can be added to the initial state vector extracted from the ascent profile at the point of failure for sensitivity analysis. Variations can also be applied to assumptions made for the missing data, such as assumed component material, thickness, etc.

It is unlikely that uncertainties in the failure criteria would change the outcome of the nuclear component in terms of whether it is released from the vehicle or not. However, variations in the failure criteria should be applied for sensitivity analysis. Dispersions can be applied to the failure integrated heating or failure temperature of each node considered in the expected sequence of failures. At the minimum, the breakup times and altitudes will be changed by these variations.

Appendix E. Coordinate Transformation Matrices

The direction cosine parameterization is denoted by C_a^b for transforming from an arbitrary a-frame to a second arbitrary b-frame. The inertial and spherical navigation coordinate systems are illustrated in Figure 24.

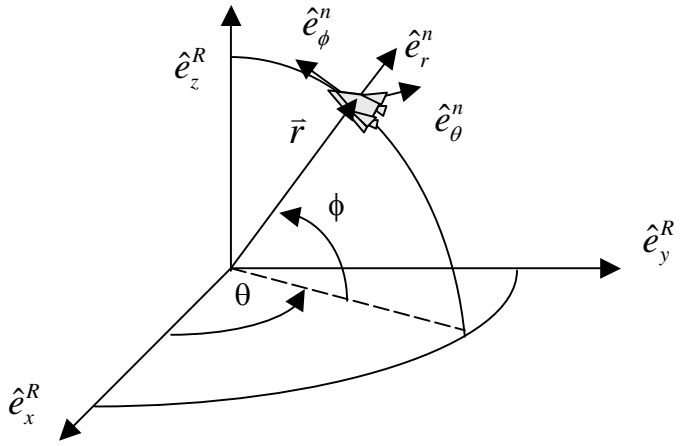


Figure 24. Rotating and Spherical Navigation Coordinate Systems

The matrix for transformation from navigation to rotating frame (C_n^R) for ϕ-Δθ rotation is: [44]

$$C_n^R = \begin{bmatrix} \cos\phi\cos(\Delta\theta) & -\sin(\Delta\theta) & -\sin\phi\cos(\Delta\theta) \\ \cos\phi\sin(\Delta\theta) & \cos(\Delta\theta) & -\sin\phi\sin(\Delta\theta) \\ \sin\phi & 0 & \cos\phi \end{bmatrix} \tag{76}$$

where ϕ is the latitude and Δθ is defined in Equation (86).

Referring to Figure 29 for the definitions of angles, the matrix for transformation from relative velocity to navigation frame (C_v^n) for γ-ψ rotation is:

$$C_v^n = \begin{bmatrix} \sin\gamma_R & 0 & -\cos\gamma_R \\ \sin\psi_R\cos\gamma_R & \cos\psi_R & \sin\psi_R\sin\gamma_R \\ \cos\psi_R\cos\gamma_R & -\sin\psi_R & \cos\psi_R\sin\gamma_R \end{bmatrix} \tag{77}$$

where γ_R is the air-relative flight path angle and ψ_R is the air-relative azimuth angle. To transform from inertial velocity to navigation frame, simply substitute the relative flight path angle and azimuth with inertial terms in the above matrix.

The matrix for transformation from rotating to inertial frame (C_R^I) is: [44]

$$C_R^I = \begin{bmatrix} \cos(\Omega t) & -\sin(\Omega t) & 0 \\ \sin(\Omega t) & \cos(\Omega t) & 0 \\ 0 & 0 & 1 \end{bmatrix} \tag{78}$$

The matrix for transformation from relative velocity to inertial frame (C_v^I) is obtained by $C_v^I = C_R^I C_n^R C_v^n$, which yields:

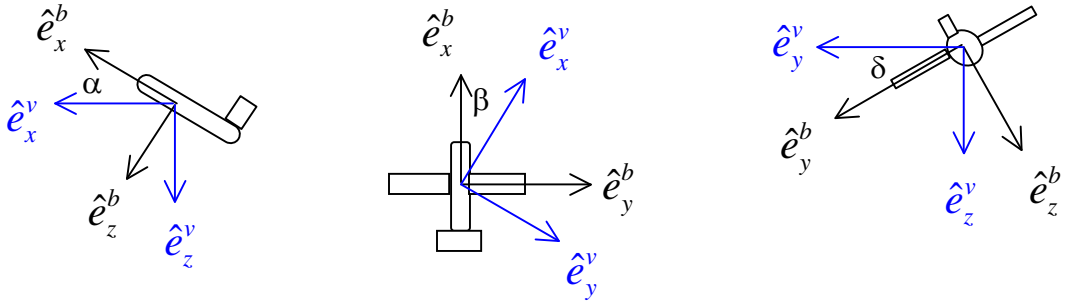
$$C_v^I = \begin{bmatrix} \begin{pmatrix} \mathrm{c}\phi\,\mathrm{s}\gamma_R\,\mathrm{c}\Theta \\ -\mathrm{s}\phi\,\mathrm{c}\psi_R\,\mathrm{c}\gamma_R\,\mathrm{c}\Theta \\ -\mathrm{s}\psi_R\,\mathrm{c}\gamma_R\,\mathrm{s}\Theta \end{pmatrix} & \begin{pmatrix} \mathrm{s}\psi_R\,\mathrm{s}\phi\,\mathrm{c}\Theta \\ -\mathrm{c}\psi_R\,\mathrm{s}\Theta \end{pmatrix} & \begin{pmatrix} -\mathrm{c}\gamma_R\,\mathrm{c}\phi\,\mathrm{c}\Theta \\ -\mathrm{s}\psi_R\,\mathrm{s}\gamma_R\,\mathrm{s}\Theta \\ -\mathrm{s}\phi\,\mathrm{c}\psi_R\,\mathrm{s}\gamma_R\,\mathrm{c}\Theta \end{pmatrix} \\ \begin{pmatrix} \mathrm{c}\phi\,\mathrm{s}\gamma_R\,\mathrm{s}\Theta \\ +\mathrm{s}\psi_R\,\mathrm{c}\gamma_R\,\mathrm{c}\Theta \\ -\mathrm{s}\phi\,\mathrm{c}\psi_R\,\mathrm{c}\gamma_R\,\mathrm{s}\Theta \end{pmatrix} & \begin{pmatrix} \mathrm{s}\psi_R\,\mathrm{s}\phi\,\mathrm{s}\Theta \\ +\mathrm{c}\psi_R\,\mathrm{c}\Theta \end{pmatrix} & \begin{pmatrix} -\mathrm{c}\gamma_R\,\mathrm{c}\phi\,\mathrm{s}\Theta \\ +\mathrm{s}\psi_R\,\mathrm{s}\gamma_R\,\mathrm{c}\Theta \\ -\mathrm{s}\phi\,\mathrm{c}\psi_R\,\mathrm{s}\gamma_R\,\mathrm{s}\Theta \end{pmatrix} \\ \begin{pmatrix} \mathrm{s}\phi\,\mathrm{s}\gamma_R \\ +\mathrm{c}\phi\,\mathrm{c}\psi_R\,\mathrm{c}\gamma_R \end{pmatrix} & \left(-\mathrm{s}\psi_R\,\mathrm{c}\phi\right) & \begin{pmatrix} \mathrm{c}\phi\,\mathrm{c}\psi_R\,\mathrm{s}\gamma_R \\ -\mathrm{c}\gamma_R\,\mathrm{s}\phi \end{pmatrix} \end{bmatrix} \tag{79}$$

where c and s denote cosine and sine. To transform from inertial velocity to inertial frame, simply substitute the relative flight path angle and azimuth with inertial terms in the above matrix.

The matrix for transformation from relative velocity to body frame (C_v^b) for δ-β-α or 1-3-2 rotation is:

$$C_v^b = \begin{bmatrix} \cos\alpha\cos\beta & \begin{pmatrix} -\sin\beta\cos\alpha\cos\delta \\ +\sin\alpha\sin\delta \end{pmatrix} & \begin{pmatrix} -\sin\beta\cos\alpha\sin\delta \\ -\sin\alpha\cos\delta \end{pmatrix} \\ \sin\beta & \cos\beta\cos\delta & \cos\beta\sin\delta \\ \sin\alpha\cos\beta & \begin{pmatrix} -\sin\beta\sin\alpha\cos\delta \\ -\sin\delta\cos\alpha \end{pmatrix} & \begin{pmatrix} -\sin\beta\sin\alpha\sin\delta \\ +\cos\alpha\cos\delta \end{pmatrix} \end{bmatrix} \quad (80)$$

where the angle-of-attack (α), sideslip (β), and bank (δ) are given in Figure 25.



(a) body x-z plane (b) body x-y plane (c) axis of rotation is out of paper

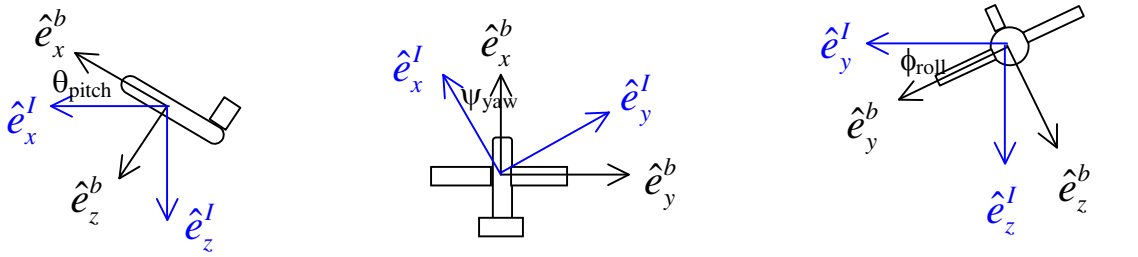
Figure 25. Angle-of-Attack, Sideslip, and Bank

Note that if δ = α = β = 0, the body and relative velocity frames would coincide.

The matrix for transformation from body to inertial frame (C_b^I) for ψ_{yaw}-θ_{pitch}-ϕ_{roll} or 3-2-1 rotation is: [45]

$$C_b^I = \begin{bmatrix} \mathrm{c}\psi_{yaw}\,\mathrm{c}\theta_{pitch} & \begin{pmatrix} \mathrm{c}\psi_{yaw}\,\mathrm{s}\theta_{pitch}s\phi_{roll} \\ -\mathrm{s}\psi_{yaw}c\phi_{roll} \end{pmatrix} & \begin{pmatrix} s\phi_{roll}\,\mathrm{s}\psi_{yaw} \\ +\mathrm{c}\psi_{yaw}\,\mathrm{s}\theta_{pitch}c\phi_{roll} \end{pmatrix} \\ \mathrm{s}\psi_{yaw}\,\mathrm{c}\theta_{pitch} & \begin{pmatrix} \mathrm{s}\psi_{yaw}\,\mathrm{s}\theta_{pitch}s\phi_{roll} \\ +\mathrm{c}\psi_{yaw}c\phi_{roll} \end{pmatrix} & \begin{pmatrix} -s\phi_{roll}\,\mathrm{c}\psi_{yaw} \\ +\mathrm{s}\psi_{yaw}\,\mathrm{s}\theta_{pitch}c\phi_{roll} \end{pmatrix} \\ -\mathrm{s}\theta_{pitch} & \mathrm{c}\theta_{pitch}s\phi_{roll} & \mathrm{c}\theta_{pitch}c\phi_{roll} \end{bmatrix} \quad (81)$$

where the Euler angles roll (ϕ_{roll}), pitch (θ_{pitch}), and yaw (ψ_{yaw}) are shown in Figure 26.



(a) pitch plane (b) yaw plane (c) roll axis out of paper

Figure 26. Euler Angles: Roll, Pitch, and Yaw

Note that if the Euler angles are zero, the body and inertial frames would coincide.

The matrix for transformation from orbit-plane to inertial frame (C_o^I) is: [46]

$$C_o^I = \begin{bmatrix} \begin{pmatrix} \mathrm{c}\,\omega_{AOP}\,\mathrm{c}\,\Omega_{LAN} \\ -\mathrm{s}\,\omega_{AOP}\,\mathrm{c}\,i\,\mathrm{s}\,\Omega_{LAN} \end{pmatrix} & \begin{pmatrix} -\mathrm{s}\,\omega_{AOP}\,\mathrm{c}\,\Omega_{LAN} \\ -\mathrm{s}\,\Omega_{LAN}\,\mathrm{c}\,i\,\mathrm{c}\,\omega_{AOP} \end{pmatrix} & \mathrm{s}\,i\,\mathrm{s}\,\Omega_{LAN} \\ \begin{pmatrix} \mathrm{c}\,\omega_{AOP}\,\mathrm{s}\,\Omega_{LAN} \\ +\mathrm{c}\,\Omega_{LAN}\,\mathrm{s}\,\omega_{AOP}\,\mathrm{c}\,i \end{pmatrix} & \begin{pmatrix} -\mathrm{s}\,\omega_{AOP}\,\mathrm{s}\,\Omega_{LAN} \\ +\mathrm{c}\,\omega_{AOP}\,\mathrm{c}\,i\,\mathrm{c}\,\Omega_{LAN} \end{pmatrix} & -\mathrm{s}\,i\,\mathrm{c}\,\Omega_{LAN} \\ \mathrm{s}\,\omega_{AOP}\,\mathrm{s}\,i & \mathrm{s}\,i\,\mathrm{c}\,\omega_{AOP} & \mathrm{c}\,i \end{bmatrix} \tag{82}$$

where the argument of periapsis (ω_{AOP}), longitude of ascending node (Ω_{LAN}), and inclination (i) are given in Figure 27.

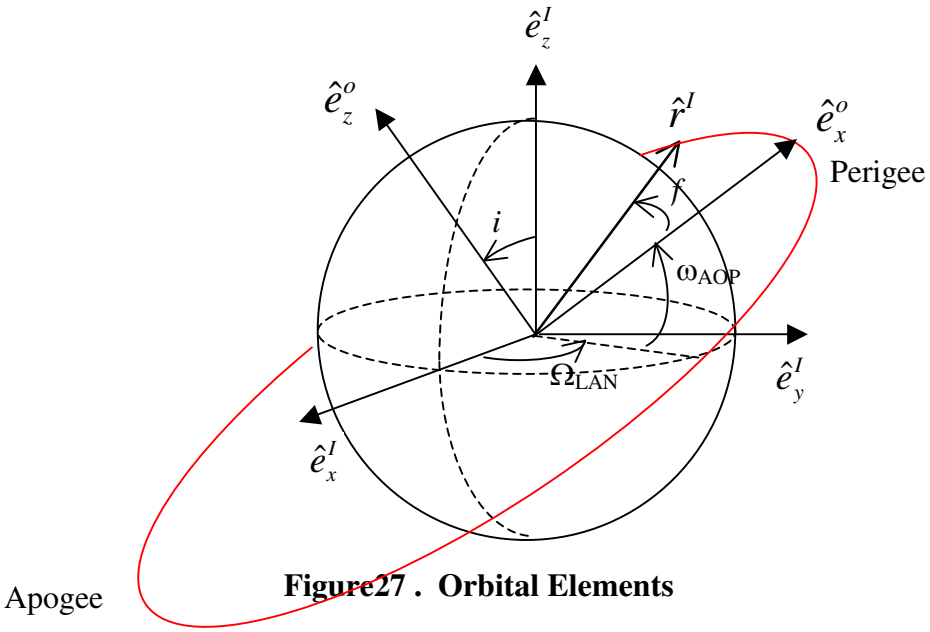


Figure27 . Orbital Elements

Note that for ortho-normal basis functions, the following is true:

$$C_a^b = \left[C_b^a \right]^T \tag{83}$$

The definitions of longitude with respect to various reference frames are given in Figure 28. The axes at t=0 and an arbitrary time, are given in solid and dashed lines, respectively. Note that the inertial axes are time invariant.

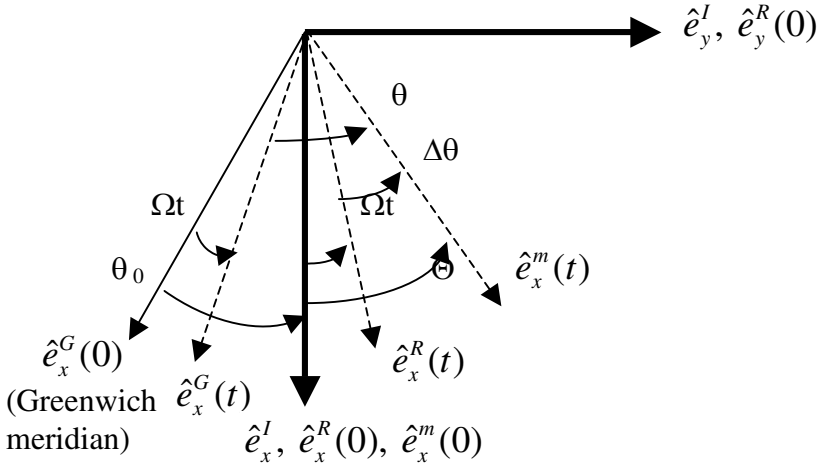


Figure 28. Definitions of longitude

where: $\hat{e}_x^m$ = Earth-centered unit vector in the inertial x-y plane and through the local meridian of the spacecraft

$\hat{e}_x^G$ = Earth-centered unit vector in the inertial x-y plane and through the Greenwich meridian

θ = Terrestrial longitude measured from the prime meridian

θ_0 = Initial terrestrial longitude at trajectory initiation (constant value)

Θ = Celestial longitude measured in inertial frame

Ω = Rotation rate of planet ($\vec{\omega}_{R/I}^I = \Omega \hat{e}_z^I$), assumed constant

t = Time

From Figure 28, the following relations can be derived:

$$\Theta = \Delta\theta + \Omega t \tag{84}$$

$$\theta = \theta_0 + \Theta - \Omega t \tag{85}$$

$$\Delta\theta = \theta - \theta_0 \tag{86}$$

Appendix F. Equations of Motion for 3-DOF Trajectory Propagation

F.1 Air-Relative Motion

The position ($\vec{r}^{\,n}$) and velocity ($\dot{\vec{r}}_R^{\,n}$) vectors in navigation frame ($\hat{e}_r^n$, $\hat{e}_\theta^n$, $\hat{e}_\phi^n$) are:

$$\vec{r}^{\,n} = r\hat{e}_r^n \tag{87}$$

$$\dot{\vec{r}}_R^{\,n} = \dot{r}\hat{e}_r^{\,n} + \vec{\omega}_{n/R}^n \times \vec{r}^{\,n} \tag{88}$$

where:

$$\vec{\omega}_{n/R}{}^{n} = \dot{\theta}\sin\phi\hat{e}_r^{\,n} - \dot{\phi}\hat{e}_\theta^{\,n} + \dot{\theta}\cos\phi\hat{e}_\phi^{\,n} \tag{89}$$

$\vec{\omega}_{n/R}{}^{n}$ is the angular velocity of the navigation frame relative to the rotating frame given in navigation frame coordinates. It is obtained using Equation (86), and the matrix for transformation between navigation and rotating frames given in Equation (76). Substituting Equation (89) into Equation (88) yields:

$$\dot{\vec{r}}_R^{\,n} = \dot{r}\hat{e}_r^{\,n} + (\dot{\theta}\sin\phi\hat{e}_r^{\,n} - \dot{\phi}\hat{e}_\theta^{\,n} + \dot{\theta}\cos\phi\hat{e}_\phi^{\,n}) \times (r\hat{e}_r^{\,n})$$

$$\dot{\vec{r}}_R^{\,n} = \dot{r}\hat{e}_r^{\,n} + r\dot{\theta}\cos\phi\hat{e}_\theta^{\,n} + r\dot{\phi}\hat{e}_\phi^{\,n} \tag{90}$$

The relative velocity vector in the velocity frame ($\dot{\vec{r}}_R^{\,v}$) is simply:

$$\dot{\vec{r}}_R^{\,v} = v_R\hat{e}_x^{\,v} \tag{91}$$

where v_R is the magnitude of the relative velocity, or $\left|\dot{\vec{r}}_R\right|$. Transforming from velocity frame to navigation frame using the matrix C_v^n in Equation (77) yields:

$$\dot{\vec{r}}_R^{\,n} = C_v^n\dot{\vec{r}}_R^{\,v}$$

$$\dot{\vec{r}}_R^{\,n} = v_R(\sin\gamma_R \hat{e}_r^{\,n} + \sin\psi_R \cos\gamma_R \hat{e}_\theta^{\,n} + \cos\psi_R \cos\gamma_R \hat{e}_\phi^{\,n}) \tag{92}$$

The following are obtained by equating the velocity components of Equations (90) and (92):

$$\begin{aligned} \hat{e}_r^{\,n}: &\quad \dot{r} = v_R \sin\gamma_R \\ \hat{e}_\theta^{\,n}: &\quad r\dot{\theta}\cos\phi = v_R \sin\psi_R \cos\gamma_R \\ \hat{e}_\phi^{\,n}: &\quad r\dot{\phi} = v_R \cos\psi_R \cos\gamma_R \end{aligned}$$

Rearranging yields:

$$\begin{aligned} \dot{r} &= v_R \sin\gamma_R \\ \dot{\theta} &= \frac{v_R \cos\gamma_R \sin\psi_R}{r\cos\phi} \\ \dot{\phi} &= \frac{v_R \cos\gamma_R \cos\psi_R}{r} \end{aligned} \tag{93}$$

The relative flight path angle is:

$$\gamma_R = \sin^{-1}\left(\frac{\dot{r}}{v_R}\right) \tag{94}$$

The acceleration vector in the velocity frame ($\ddot{\vec{r}}_R^{\,v}$) is obtained by taking the time derivative of Equation (91):

$$\ddot{\vec{r}}_R^{\,v} = \dot{v}_R \hat{e}_x^{\,v} + v_R(\vec{\omega}_{v/R}^{\,v} \times \hat{e}_x^{\,v}) \tag{95}$$

$\vec{\omega}_{v/R}^{\,v}$ is the angular velocity of the velocity frame relative to the rotating frame given in velocity frame coordinates. From Ref. [47]:

$$\vec{\omega}_{v/R}{}^{v} = \cos\gamma_R\left[\dot{\theta}(\cos\psi_R\cos\phi + \tan\gamma_R\sin\phi) - \dot{\phi}\sin\psi_R - \dot{\psi}_R\tan\gamma_R\right]\hat{e}_x{}^{v}$$
$$+\left[\dot{\gamma}_R - \dot{\theta}\sin\psi_R\cos\phi - \dot{\phi}\cos\psi_R\right]\hat{e}_y{}^{v} \quad (96)$$
$$+\cos\gamma_R\left[\dot{\theta}(\cos\psi_R\tan\gamma_R\cos\phi - \sin\phi) - \dot{\phi}\sin\psi_R\tan\gamma_R + \dot{\psi}_R\right]\hat{e}_z{}^{v}$$

The following relationships are applied:

$$\vec{\omega}\times\hat{e}_x = \omega_3\hat{e}_y - \omega_2\hat{e}_z$$
$$\vec{\omega}\times\hat{e}_y = -\omega_3\hat{e}_x + \omega_1\hat{e}_z$$
$$\vec{\omega}\times\hat{e}_z = \omega_2\hat{e}_x - \omega_1\hat{e}_y$$

Substituting, Equation (95) becomes:

$$\ddot{\vec{r}}_R{}^{v} = \dot{v}_R\hat{e}_x{}^{v} + v_R(\omega_3\hat{e}_y{}^{v} - \omega_2\hat{e}_z{}^{v})$$
$$= \dot{v}_R\hat{e}_x{}^{v} + v_R\cos\gamma_R\left[\dot{\theta}(\cos\psi_R\tan\gamma_R\cos\phi - \sin\phi) - \dot{\phi}\sin\psi_R\tan\gamma_R + \dot{\psi}_R\right]\hat{e}_y{}^{v} \quad (97)$$
$$-v_R\left[\dot{\gamma}_R - \dot{\theta}\sin\psi_R\cos\phi - \dot{\phi}\cos\psi_R\right]\hat{e}_z{}^{v}$$

Substituting Equation (93) for the angular rates yields:

$$\ddot{\vec{r}}_R{}^{v} = \dot{v}_R\hat{e}_x{}^{v} - v_R\cos\gamma_R\left(\frac{v_R}{r}\cos\gamma_R\sin\psi_R\tan\phi - \dot{\psi}_R\right)\hat{e}_y{}^{v} + v_R\left(\frac{v_R}{r}\cos\gamma_R - \dot{\gamma}_R\right)\hat{e}_z{}^{v} \quad (98)$$

The relative acceleration in navigation frame ($\ddot{\vec{r}}_R^{\,n}$) is obtained by transforming the above equation using the matrix in Equation (77):

$$\ddot{\vec{r}}_R^{\,n} = C_v^n\ddot{\vec{r}}_R^{\,v}$$

F.2 Inertial Motion

The position vector in velocity frame ($\vec{r}^{\,v}$) is obtained by transforming Equation (87) from the navigation frame using C_n^v obtained from the transpose of Equation (77):

$$\vec{r}^{\,v} = r\sin\gamma_R\hat{e}_x{}^{v} - r\cos\gamma_R\hat{e}_z{}^{v} \quad (99)$$

The inertial velocity is obtained by taking the time derivative of Equation (99):

$$\begin{aligned}\dot{\vec{r}}_I^{\,v} &= (\dot{r}\sin\gamma_R + r\dot{\gamma}_R\cos\gamma_R)\hat{e}_x^{\,v} + r\sin\gamma_R(\vec{\omega}_{v/I}^{\,v}\times\hat{e}_x^{\,v}) \\ &\quad -(\dot{r}\cos\gamma_R - r\dot{\gamma}_R\sin\gamma_R)\hat{e}_z^{\,v} - r\cos\gamma_R(\vec{\omega}_{v/I}^{\,v}\times\hat{e}_z^{\,v})\end{aligned} \tag{100}$$

$\vec{\omega}_{v/I}^{\,v}$ is the angular velocity of the velocity frame relative to the inertial frame given in velocity frame coordinates. From Ref. [47]:

$$\begin{aligned}\vec{\omega}_{v/I}^{\,v} &= \cos\gamma_R\left[\dot{\Theta}(\cos\psi_R\cos\phi + \tan\gamma_R\sin\phi) - \dot{\phi}\sin\psi_R - \dot{\psi}_R\tan\gamma_R\right]\hat{e}_x^{\,v} \\ &\quad +\left[\dot{\gamma}_R - \dot{\Theta}\sin\psi_R\cos\phi - \dot{\phi}\cos\psi\right]\hat{e}_y^{\,v} \\ &\quad +\cos\gamma_R\left[\dot{\Theta}(\cos\psi_R\tan\gamma_R\cos\phi - \sin\phi) - \dot{\phi}\sin\psi_R\tan\gamma_R + \dot{\psi}_R\right]\hat{e}_z^{\,v}\end{aligned} \tag{101}$$

Note that from Equation (84):

$$\dot{\Theta} = \dot{\theta} + \Omega \tag{102}$$

Substituting Equations (93), (101), and (102) into Equation (100) yields:

$$\begin{aligned}\dot{\vec{r}}_I^{\,v} &= (v_R + r\Omega\sin\psi_R\cos\phi\cos\gamma_R)\hat{e}_x^{\,v} + r\Omega\cos\psi_R\cos\phi\hat{e}_y^{\,v} \\ &\quad +r\Omega\sin\psi_R\cos\phi\sin\gamma_R\hat{e}_z^{\,v}\end{aligned} \tag{103}$$

The inertial acceleration vector is obtained in similar fashion:

$$\begin{aligned}\ddot{\vec{r}}_I^{\,v} &= (\dot{v}_R - \Omega^2 r\sin\gamma_R\cos^2\phi + \Omega^2 r\cos\psi_R\cos\phi\cos\gamma_R\sin\phi)\hat{e}_x^{\,v} \\ &\quad +(\dot{\psi}_R v_R\cos\gamma_R - 2v_R\Omega\sin\phi\cos\gamma_R - \frac{{v_R}^2}{r}\cos^2\gamma_R\sin\psi_R\tan\phi \\ &\quad +2v_R\Omega\cos\psi_R\sin\gamma_R\cos\phi - \Omega^2 r\sin\psi_R\cos\phi\sin\phi)\hat{e}_y^{\,v} \\ &\quad +(\frac{{v_R}^2}{r}\cos\gamma_R + 2\Omega v_R\sin\psi_R\cos\phi - \dot{\gamma}_R v_R + r\Omega^2\cos^2\phi\cos\gamma_R \\ &\quad +\Omega^2 r\cos\psi_R\cos\phi\sin\gamma_R\sin\phi)\hat{e}_z^{\,v}\end{aligned} \tag{104}$$

To obtain the inertial flight path angle, first transform Equation (103) from velocity frame to navigation frame using the transformation matrix in Equation (77):

$$\dot{\vec{r}}_I^{\,n} = v_R \cos\psi_R \cos\gamma_R \hat{e}_\phi^{\,n} + (v_R \sin\psi_R \cos\gamma_R + r\Omega\cos\phi)\hat{e}_\theta^{\,n} + v_R \sin\gamma_R \hat{e}_r^{\,n} \tag{105}$$

Referring to Equation (93), the inertial flight path angle obtained from the above equation is then:

$$\gamma_I = \sin^{-1}\left(\frac{v_R \sin\gamma_R}{v_I}\right)$$

$$\gamma_I = \sin^{-1}\left(\frac{\dot{r}}{v_I}\right) \tag{106}$$

The inertial acceleration vector in the navigation frame is obtained by transforming Equation (104) from the velocity frame using the transformation matrix in Equation (77):

$$\ddot{\vec{r}}_I^{\,n} = C_v^n \ddot{\vec{r}}_I^{\,v}$$

F.3 Relationship Between Inertial and Relative Vectors

Comparing Equations (104) and (98), the inertial acceleration can also be written as:

$$\begin{aligned}\ddot{\vec{r}}_I^{\,v} = \ddot{\vec{r}}_R^{\,v} &+ \Omega^2 r(\cos\psi_R \cos\phi \cos\gamma_R \sin\phi - \sin\gamma_R \cos^2\phi)\hat{e}_x^{\,v} \\ &+ \Omega\cos\phi(2v_R \cos\psi_R \sin\gamma_R - 2v_R \tan\phi \cos\gamma_R - \Omega r \sin\psi_R \sin\phi)\hat{e}_y^{\,v} \\ &+ \Omega\cos\phi(2v_R \sin\psi_R + r\Omega\cos\phi\cos\gamma_R + \Omega r \cos\psi_R \sin\gamma_R \sin\phi)\hat{e}_z^{\,v}\end{aligned} \tag{107}$$

Comparing Equations (105) and (92), the inertial velocity can also be written as:

$$\dot{\vec{r}}_I^{\,n} = \dot{\vec{r}}_R^{\,n} + (r\Omega\cos\phi)\hat{e}_\theta^{\,n} \tag{108}$$

Or, comparing Equations (103) and (91) in the velocity frame yields:

$$\dot{\vec{r}}_I^{\,v} = \dot{\vec{r}}_R^{\,v} + (r\Omega\sin\psi_R \cos\phi\cos\gamma_R)\hat{e}_x^{\,v} + r\Omega\cos\psi_R\cos\phi\hat{e}_y^{\,v} + r\Omega\sin\psi_R\cos\phi\sin\gamma_R\hat{e}_z^{\,v} \tag{109}$$

The following are worth noting:

1. All the terms associated with the rotation of Earth (Ω) in the equations describing inertial motion contribute to the difference between the relative and inertial vectors. Also, note that the difference is not a function of longitude.
2. From Equation (108), note that the inertial and relative velocity vectors have the same components of velocity radially and tangent to the local meridian.
3. The "relative velocity" is often referred to as the air-relative, wind-relative, with-rotating-atmosphere, with-rotating-planet, aerodynamic, freestream, or topocentric velocity (assuming no local wind).

F.4 Dynamics

The dynamics modeling includes aerodynamics, thrust, and gravitation:

$$\begin{aligned} \sum \vec{F}^v &= \sum F_x^v \hat{e}_x^v + \sum F_y^v \hat{e}_y^v + \sum F_z^v \hat{e}_z^v \\ &= \vec{F}_{aero}^v + \vec{F}_{thrust}^v + \vec{F}_{grav}^v \end{aligned} \tag{110}$$

The aerodynamic forces in the velocity frame, body-fixed thrust, and gravitation are given in Ref. [41].

Table 14 summarizes the calculations to obtain the thrust force (F_{thrust}) and rate of fuel consumption ($\dot{m}$), depending on the inputs provided by the user.

Table 14. Thrust Calculation

Inputs	Thrust	$\dot{m}$
Isp, $\dot{m}$	$F_{thrust} = I_{sp} g_{Earth} \dot{m}$	given
Isp, F_{thrust}	given	$\dot{m} = \dfrac{F_{thrust}}{I_{sp} g_{Earth}}$

where: F_{thrust} = thrust force

$\dot{m}$ = rate of fuel consumption

Isp = engine specific impulse

g_{Earth} = Earth gravitational acceleration

F.5 Equations of Motion

The force equation in the velocity frame is:

$$\sum \vec{F} = m\ddot{\vec{r}}_I^{\,v}$$

where the left-hand-side is the dynamics and the right-hand-side is the kinematics. The inertial acceleration expressed in the velocity frame given in Equation (104) is used:

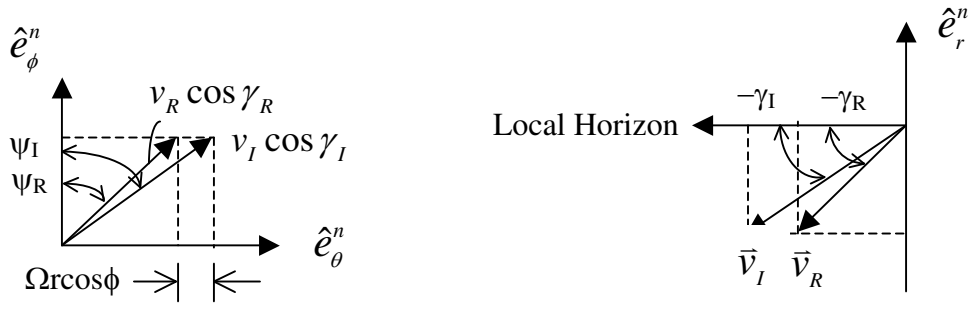
$$\begin{aligned}
\sum F_x^{\,v} &= m(\dot{v}_R - r\Omega^2\cos^2\phi\sin\gamma_R + r\Omega^2\cos\phi\cos\psi_R\sin\phi\cos\gamma_R) \\
\sum F_y^{\,v} &= m(\dot{\psi}_R v_R\cos\gamma_R - \frac{v_R^{\,2}}{r}\sin\psi_R\tan\phi\cos^2\gamma_R - r\Omega^2\cos\phi\sin\psi_R\sin\phi \\
&\quad +2v_R\Omega\sin\gamma_R\cos\phi\cos\psi_R - 2v_R\Omega\sin\phi\cos\gamma_R) \\
\sum F_z^{\,v} &= m(-\dot{\gamma}_R v_R + \frac{v_R^{\,2}}{r}\cos\gamma_R + r\Omega^2\cos\gamma_R\cos^2\phi \\
&\quad +r\Omega^2\sin\phi\sin\gamma_R\cos\phi\cos\psi_R + 2v_R\Omega\cos\phi\sin\psi_R)
\end{aligned}$$

Rearranging,

$$\begin{aligned}
\dot{v}_R &= \frac{\sum F_x^{\,v}}{m} + r\Omega^2\cos^2\phi\sin\gamma_R - r\Omega^2\cos\phi\cos\psi_R\sin\phi\cos\gamma_R \\
\dot{\psi}_R &= \frac{\sum F_y^{\,v}}{mv_R\cos\gamma_R} + \frac{v_R}{r}\sin\psi_R\tan\phi\cos\gamma_R + \frac{r\Omega^2}{v_R\cos\gamma_R}\cos\phi\sin\psi_R\sin\phi \\
&\quad -2\Omega\tan\gamma_R\cos\phi\cos\psi_R + 2\Omega\sin\phi \qquad (111) \\
\dot{\gamma}_R &= -\frac{\sum F_z^{\,v}}{mv_R} + \frac{v_R}{r}\cos\gamma_R + \frac{r\Omega^2}{v_R}\cos\gamma_R\cos^2\phi \\
&\quad +\frac{r\Omega^2}{v_R}\sin\phi\sin\gamma_R\cos\phi\cos\psi_R + 2\Omega\cos\phi\sin\psi_R
\end{aligned}$$

Equations (93) and (111) form the set of governing equations for translational motion.

F.6 Transformation of Vehicle State to Rotating Frame



(a) Local horizontal plane (b) Local vertical plane

Figure 29. Azimuth and Flight Path Angle

It was shown previously that the inertial and relative velocity vectors have the same components of velocity radially and tangent to the local meridian. Thus, the following relations are obtained from Figure 29:

$$v_R \cos\gamma_R \cos\psi_R = v_I \cos\gamma_I \cos\psi_I \tag{112}$$

$$v_R \cos\gamma_R \sin\psi_R + \Omega r \cos\phi = v_I \cos\gamma_I \sin\psi_I \tag{113}$$

$$v_R \sin\gamma_R = v_I \sin\gamma_I \tag{114}$$

Given the vehicle state in inertial spherical coordinates, the air-relative state can be obtained, and vice versa. Thus, the 3 unknowns are either (v_I, γ_I, ψ_I) or (v_R, γ_R, ψ_R), depending on the direction of transformation. The 3 unknowns are solved using the 3 equations in (112) through (114), as discussed in the following subsections.

F.7 Inertial State to Air-Relative State in Spherical Coordinates

The vehicle state in inertial spherical coordinates consists of the inertial velocity (v_I), inertial flight path angle (γ_I), latitude (ϕ), longitude (θ), radius (r), and inertial azimuth (ψ_I). Rearranging Equation (112), the following is obtained:

$$v_R \cos\gamma_R = \frac{v_I \cos\gamma_I \cos\psi_I}{\cos\psi_R} \tag{115}$$

Substituting into Equation (113) yields:

$$\tan\psi_R v_I \cos\gamma_I \cos\psi_I + \Omega r \cos\phi = v_I \cos\gamma_I \sin\psi_I \tag{116}$$

Rearranging,

$$\psi_R = \tan^{-1} \frac{v_I \cos\gamma_I \sin\psi_I - \Omega r \cos\phi}{v_I \cos\gamma_I \cos\psi_I} \tag{117}$$

Note that the correct quadrant for the azimuth needs to be evaluated. Rearranging Equation (114) yields:

$$v_R = \frac{v_I \sin\gamma_I}{\sin\gamma_R}$$

Substitute into Equation (115) and rearrange:

$$\gamma_R = \tan^{-1}\left[\frac{\cos\psi_R \tan\gamma_I}{\cos\psi_I}\right] \tag{118}$$

The sign of γ_R is the same as that of γ_I. The above equation is solved after Equation (117) such that ψ_R is known. Next, the air-relative speed is solved:

$$v_R = \frac{v_I \sin\gamma_I}{\sin\gamma_R} \tag{119}$$

In the case of a circular orbit, Equation (119) encounters the divide-by zero problem. The relative speed should then be solved by rearranging Equation (112) or (113), for example:

$$v_R = \frac{v_I \sin\psi_I \cos\gamma_I - \Omega r \cos\phi}{\cos\gamma_R \sin\psi_R} \tag{120}$$

At the maximum/minimum latitude (where $\phi = \pm$ inclination), $\psi_I = \psi_R = \pm 90^o$. In this case, Equation (118) for calculating the air-relative flight path angle encounters the divide-by-zero problem. Alternatively, Equations (113) and (114) are used to obtain the solution:

$$\gamma_R = \tan^{-1}\left[\frac{v_I \sin\psi_R \sin\gamma_I}{v_I \cos\gamma_I \sin\psi_I - \Omega r \cos\phi}\right] \tag{121}$$

F.8 Air-Relative State to Inertial State in Spherical Coordinates

The vehicle state in rotating spherical coordinates consists of the air-relative velocity (v_R), air-relative flight path angle (γ_R), latitude (ϕ), longitude (θ), radius (r), and air-relative azimuth (ψ_R). Rearranging Equation (112), the following is obtained:

$$v_I \cos\gamma_I = \frac{v_R \cos\gamma_R \cos\psi_R}{\cos\psi_I} \tag{122}$$

Substituting into Equation (113) yields:

$$v_R \cos\gamma_R \sin\psi_R + \Omega r \cos\phi = v_R \cos\gamma_R \cos\psi_R \tan\psi_I \tag{123}$$

Rearranging,

$$\psi_I = \tan^{-1}\frac{v_R \cos\gamma_R \sin\psi_R + \Omega r \cos\phi}{v_R \cos\gamma_R \cos\psi_R} \tag{124}$$

The correct quadrant for ψ_I needs to be evaluated. Rearranging Equation (114) yields:

$$v_I = \frac{v_R \sin\gamma_R}{\sin\gamma_I}$$

Substituting into Equation (122) and rearranging,

$$\gamma_I = \tan^{-1}\left[\frac{\cos\psi_I \tan\gamma_R}{\cos\psi_R}\right] \tag{125}$$

The sign of γ_I is the same as that of γ_R. The above equation is solved after Equation (124) such that ψ_I is known. Next, the inertial speed is solved:

$$v_I = \frac{v_R \sin\gamma_R}{\sin\gamma_I} \tag{126}$$

F.9 Inertial State in Cartesian Coordinates to Air-Relative State in Spherical Coordinates

In the event of a launch failure, the initial vehicle state in inertial frame Cartesian coordinates based on tracking data is provided by the Air Force Space Command. Therefore, transformation from the inertial Cartesian coordinates to the rotating spherical coordinates is needed. The vehicle state in inertial Cartesian coordinates is given by:

$$\begin{aligned}\vec{r}^{\,I} &= X\hat{e}_x^I + Y\hat{e}_y^I + Z\hat{e}_z^I \\ \vec{v}_I^{\,I} &= U\hat{e}_x^I + V\hat{e}_y^I + W\hat{e}_z^I\end{aligned} \tag{127}$$

such that:

$$r = \sqrt{X^2 + Y^2 + Z^2} \tag{128}$$

$$v_I = \sqrt{U^2 + V^2 + W^2} \tag{129}$$

The latitude, longitude, and azimuth are given by:

$$\phi = \sin^{-1}\left(\frac{Z}{r}\right) \tag{130}$$

$$\Theta = \tan^{-1}\left(\frac{Y}{X}\right) \tag{131}$$

$$\psi_I = \tan^{-1}\left[\frac{-U\sin\Theta + V\cos\Theta}{-U\sin\phi\cos\Theta - V\sin\phi\sin\Theta + W\cos\phi}\right] \tag{132}$$

Note that the correct quadrant for the azimuth needs to be evaluated. The radial velocity is obtained by:

$$\dot{r} = \vec{v}_I^I \bullet \hat{r}^I \tag{133}$$

The inertial flight path angle is:

$$\gamma_I = \sin^{-1}\frac{\dot{r}}{v_I} \tag{134}$$

The inertial vehicle state in spherical coordinates is then transformed to the rotating, spherical coordinates.

Appendix G. MER Data for Vehicle Breakup Analysis

Information on the MER spacecraft, launch vehicle, thermal nodes, exposure factors, failure criteria, etc, required to perform vehicle breakup analysis are given in this section.

G.1 Task Description

The MER pre-launch vehicle breakup analysis required trajectory simulations with thermal and structural modeling for the prediction of the LWRHU footprint. Before the vehicle breakup analysis could be performed, much research was needed to collect essential information such as the vehicle configuration, possible reentry scenarios, requirements to meet task objectives, and so forth. Detailed discussions of the above tasks and the results of the vehicle breakup analysis are given in the following subsections.

G.2 Launch Vehicle and Spacecraft Configuration

The MER-A and MER-B spacecraft were launched using Delta II 7925 and Delta II 7925H launch vehicles, respectively. The differences between the two launch vehicles were assumed negligible for vehicle breakup purposes, and only one configuration was analyzed. The launch vehicle configuration is given in Figure 30 [57]. Major components of the launch vehicle included First Stage, Second Stage, Third-Stage motor, nine Graphite Epoxy Motors (GEM), and Fairing. In the event of an unrecoverable vehicle malfunction in the launch vehicle, the Flight Termination System (FTS) would be activated either automatically or by command, to terminate vehicle thrust and disperse propellants [57]. For MER, the third stage motor had two additional large conical shaped

charges mounted on the Payload Attach Fitting (PAF) with the outputs directed into the dome of the motor (in the direction of the spacecraft).

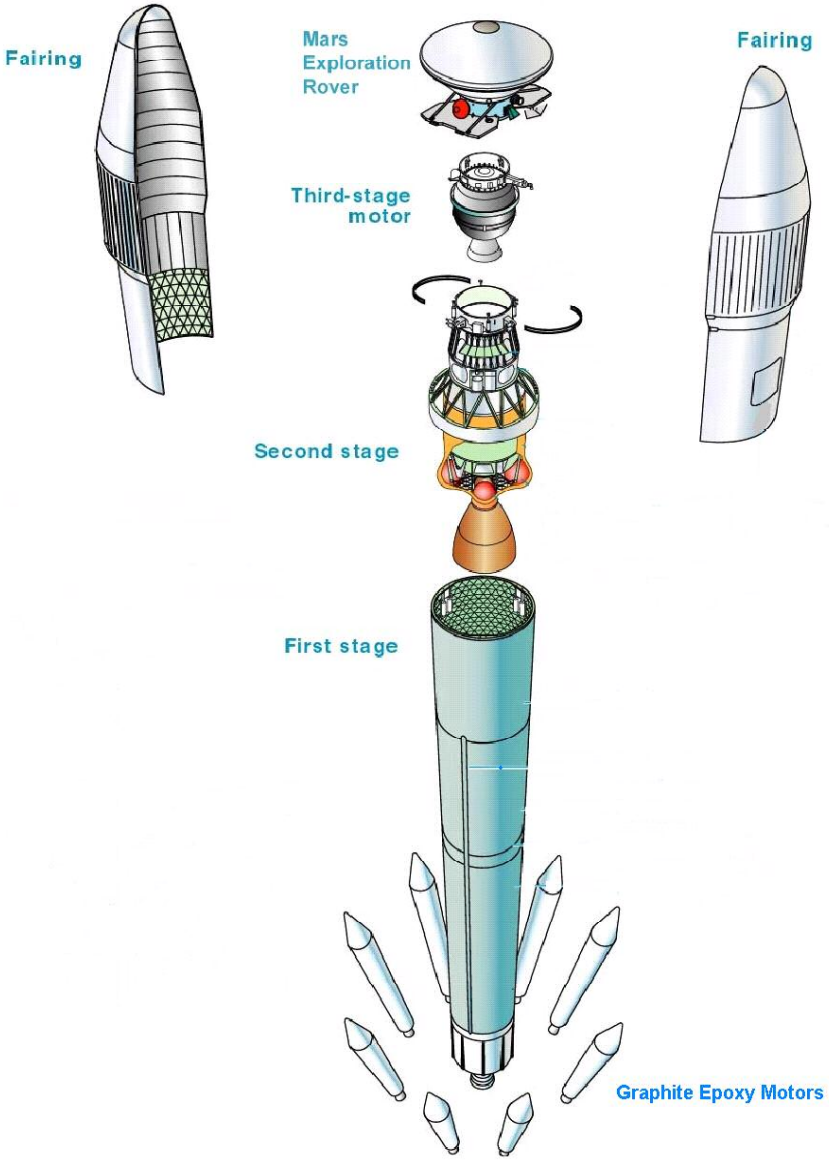


Figure 30. Delta II 7925 Launch Vehicle Configuration

The MER-A and MER-B spacecrafts were identical, and the configuration is given in Figure 31 [57]. Major components of the spacecraft included the Heatshield (H/S), Backshell (B/S), Cruise Stage (CS), Lander, and Rover.

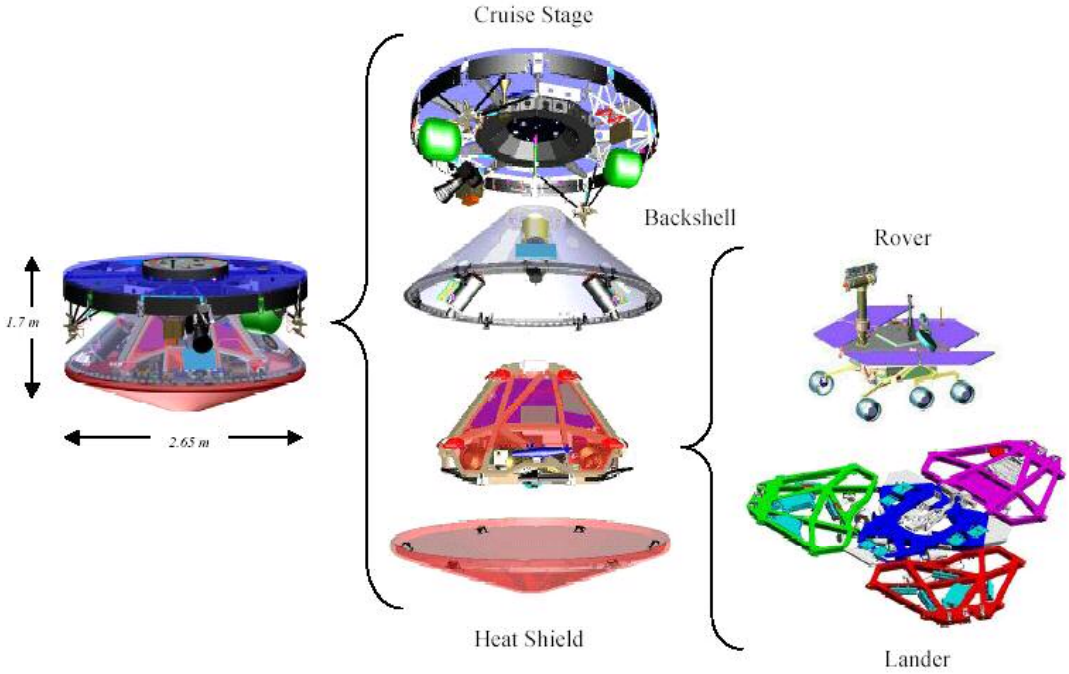


Figure 31. MER Spacecraft Configuration

G.3 Mission Timeline

The launch window for MER-A and MER-B extended from May 30 to July 15, 2003. Two launch opportunities existed for each day, at launch azimuth of 93º and 99º, respectively. The mission timeline depended on the day of launch and the launch opportunity. For example, the timelines of the actual days of launch for MER-A and MER-B corresponding to the first and second launch opportunities on June 10 and July 7, respectively, are given in Table 15 [58].

Table 15. Mission Timelines

Event	MER-A, June 10, 2003 Azimuth 93° (sec)	MER-B, July 7, 2003 Azimuth 99° (sec)
Liftoff	0.000	0.000
Jettison 6 GL GEM	66.000	80.500
Jettison 3 AL GEM	131.500	159.500
MECO	263.409	263.469
Stage I – II Separation	271.409	271.469
Jettison Fairing	282.000	282.000
SECO 1	578.489	528.447
First Restart – Stage II	1588.686	4317.164
SECO 2	1714.543	4466.730
Fire Spin Rockets	1764.543	4516.730
Jettison Stage II	1767.543	4519.730
Stage III Ignition	1804.543	4556.730
Stage III Burnout	1891.683	4643.870
Initiate Yo-Yo Despin	2174.543	4926.730
Jettison Stage III	2179.543	4931.730

where: GL = Ground Lit

AL = Air Lit

MECO = Main Engine Cutoff

SECO = Second Stage Engine Cutoff

G.4 Assumptions and Considerations

From the time of liftoff until the MER spacecraft began the interplanetary cruise to Mars, an unrecoverable vehicle malfunction could occur to end the mission with the possibility of atmospheric reentry of the vehicle to impact Earth surface. To bound the

failure scenarios for vehicle breakup analysis, the following assumptions and considerations were imposed:

1. The FTS would be activated upon unrecoverable vehicle malfunction during the ascent phase.
2. A mission-ending failure consisting of multiple independent malfunctions were not credible and therefore not considered.
3. Before failure occurred, the launch vehicle was on course and did not deviate from the nominal path. After the FTS activation, the debris remained on course.
4. Incremental velocity from the FTS activation was neglected. Therefore, the end condition of the launch vehicle trajectory was the initial condition for the debris trajectory.
5. The spacecraft configuration remained undamaged after the FTS activation.
6. A 50 kg mass representing the end dome from the Stage III motor would survive the FTS activation and remain attached to the spacecraft.
7. The forces exerted on the spacecraft from the activation of two shaped charges as part of the FTS would likely be uneven and asymmetric. Therefore, the spacecraft was assumed to be tumbling after the FTS activation.
8. Timed sequences in the parking orbit would occur nominally unaffected by the failure, including the start and end of burns, staging, and spin up. This was consistent with the assumptions made in the V-Gamma Map.
9. Thrust misalignment in the parking orbit would be fixed in the inertial frame and prevailed through the Stage II and Stage III burns. This was consistent with the assumptions made in the V-Gamma Map.

Material surface emissivity (ε) was assumed constant and invariant to temperature.

G.5 Reentry Scenarios

The multitude of possible unrecoverable vehicle malfunctions would lead to various reentry scenarios. The reentry scenarios were categorized into two types: (1) suborbital and (2) out-of-orbit.

The suborbital reentries resulted from failures during the ascent. An unrecoverable vehicle malfunction during the ascent would trigger an automated or commanded activation of the FTS. After the destruction of the launch vehicle, the freed spacecraft would continue on its upward trajectory. Unable to escape due to gravity, the spacecraft would eventually head back towards Earth in a fallback trajectory. The outcome would be a nominal surface impact point, accurate within a range of uncertainties defined by a footprint. The nominal impact point was unique, dependent specifically on the point in the ascent trajectory at which the FTS was activated. A FTS activation early in the ascent while the vehicle speed was still relatively low would result in a surface impact in the Atlantic Ocean. A FTS activation late in the ascent after the vehicle had picked up speed would result in an impact point in Africa. Therefore, the suborbital reentries were further categorized into two types: (1) low speed for ocean impact and (2) high speed for land impact. The spacecraft was assumed to be tumbling in suborbital reentries due to asymmetric forces from the conical shaped charges in the activation of the FTS.

The out-of-orbit reentries resulted from failures while in the parking orbit after a successful ascent. A failure while in the parking orbit could be the result of steady misaligned burns (SMB), an incomplete burn, or no burn in the Stage II and III engines.

The thrust misalignment was measured by the cone and clock angles in the yaw plane and about the roll axis, respectively. Depending on the misaligned burns, the spacecraft would be propelled into a specific orbit, with an atmospheric reentry as a possible outcome of the SMB. The reentries were categorized into six classes: (1) prompt elliptic, (2) delayed elliptic, (3) powered entry, (4) circular orbit decay or COD, (5) decay of an initial ellipse, and (6) prompt hyperbolic. The delayed elliptic reentry involved the spacecraft passing through the apogee before reentering the atmosphere. Thus, the spacecraft would be separated from Stage III and spinning. The powered entry involved the spacecraft reentering the atmosphere during the Stage II burn, coast, or Stage III burn. Thus, the spacecraft could be reentering at different speeds and angles, depending on the cone and clock angles. The COD could result from a scenario where the spacecraft was left in Earth orbit, separated from the Stage III motor, unable to boost to a Sufficiently High Orbit (SHO), unable to control attitude, spinning at two rpm, and finally de-orbited after prolonged drag effects. The powered entry, delayed elliptic, and COD were considered for out-of-orbit reentry scenarios. The spacecraft was assumed to be spinning in out-of-orbit reentries due to the firing of the spin rockets following SECO 2 as part of the nominal timeline (see Table 15).

In summary, the reentry scenarios considered included:

1. Suborbital Reentry
    a. Low speed (fallback trajectory resulting in ocean impact point in Atlantic Ocean)
    b. High speed (fallback trajectory resulting in ground impact point in Africa)
2. Out-of-orbit Reentry

a. Circular orbit decay

b. Delayed elliptic

c. Powered reentry

G.6 Thermal Nodes

Vehicle breakup could occur due to aerodynamic heating and/or g-load. For thermal and structural analyses, the launch vehicle and spacecraft were analyzed in detail to determine the weak points where failure was likely to occur. Based on this information, the vehicles were then divided into components and modeled as thermal nodes. The thermal nodes included major components and supports on the launch vehicle and spacecraft as described in the following subsections.

G.6.1 Cruise Stage Thermal Nodes

Twenty-five thermal nodes were identified for the Cruise Stage as shown in Figure 32.

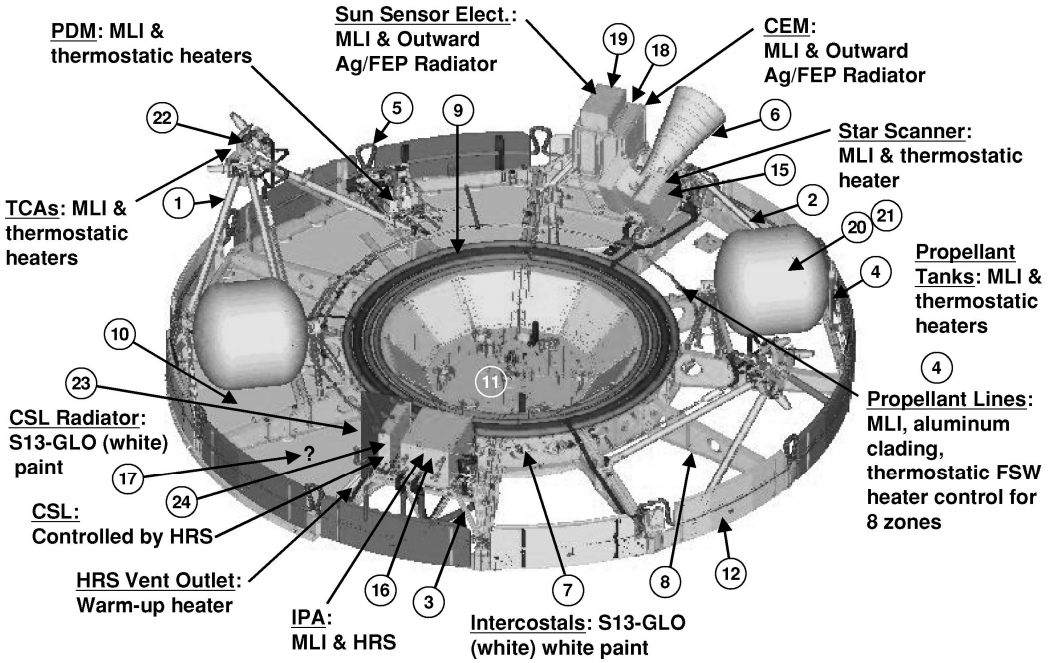


Figure 32. Cruise Stage Thermal Nodes

The characteristics and material properties of the 25 Cruise Stage thermal nodes used in the vehicle breakup analysis are given in Table 16 and were applicable to both MER-A and MER-B.

Table 16. Properties of Cruise Stage Thermal Nodes

Node #	Node Name	Mass (kg)	Shape	d (cm)	Radius (cm)	Material	ε	Density (g/cm^3)	c (J/g/C)
1	Cluster strut	1	cyl	0.089	1.27	Ti-6-4	0.12	4.5	0.71
2	Star scanner strut	1	cyl	0.089	0.794	Ti-6-4	0.12	4.5	0.71
3	IPA strut	1	cyl	0.089	1.27	Al 2297	0.09	2.7	1.027
4	Propellant tube	1	cyl	0.05	0.318	S/S 316	0.14	7.9	0.639
5	HRS tube	1	cyl	0.05	0.318	S/S 316	0.14	7.9	0.639
6	Star scanner cone	1.08	cyl	0.025	6.35	Al 6061	0.09	2.7	1.027
7	Intercostal	0.63	cyl	0.178	5.08	Al 2297	0.09	2.7	1.027
8	Rib (12)	1.11	cyl	0.152	5.08	Al 2297	0.09	2.7	1.027
9	Torus	9.49	cyl	0.229	10.16	Al 2295	0.09	2.7	2.7
10	Honeycomb faceskin	195	sph	0.013	129.54	Al 2024	0.09	2.7	1.027
11	LVA plate	28.6	sph	1.614	45.72	Al 7075	0.09	2.7	1.027
12	HRS box	0.42	sph	0.042	8.89	Al 6061	0.09	2.7	1.027
13	Fiberglass cable sleeve	4	cyl	0.152	2.54	Fglass/E	0.8	2.5	0.78
14	Circuit board	0.08	sph	0.127	7.62	Fglass/E	0.8	2.5	0.78
15	Star scanner electronics box	4.32	sph	0.102	5.08	Al 6061	0.09	2.7	1.027
16	IPA box	7.3	sph	0.102	12.065	Al 6061	0.09	2.7	1.027
17	PDM box	2.09	sph	0.102	9.525	Al 6061	0.09	2.7	1.027
18	CEM box	4.11	sph	0.102	10.16	Al 6061	0.09	2.7	1.027
19	SSE box	1.13	sph	0.157	8.255	Al 6061	0.09	2.7	1.027

20	Hydrazine tank GE skin	2.91	sph	0.025	20.955	Ti-6-4	0.8	1.39	0.92
21	Hydrazine tank Al skin	2.91	sph	0.015	20.955	–	0.09	2.7	1.027
22	Thruster cluster	2.8	sph	0.541	6.35	Al 6061	0.09	2.7	1.027
23	Shark fin radiator	1.4	sph	0.686	19.431	Al 6061	0.09	2.7	1.027
24	CSLA box	2	sph	0.102	9.906	Albemet	0.09	2.7	1.027
25	Cable copper braid	3.6	cyl	0.051	2.286	Cu 102	0.1	8.96	0.38

where: IPA = Integrated Pump Assembly

HRS = Heat Rejection System

LVA = Launch Vehicle Adapter

PDM = Propellant Distribution Module

CEM = Cruise Electronics Module

SSE = Sun Sensor Electronics

GE = graphite epoxy

Al = Aluminum

CSLA = Cruise Shunt Limiter Assembly

d = Component thickness

c = Material specific heat

cyl = Cylinder

sph = Sphere

Ti = Titanium

S/S = Stainless Steel

Fglass/E = Fiberglass / Epoxy

Cu = Copper

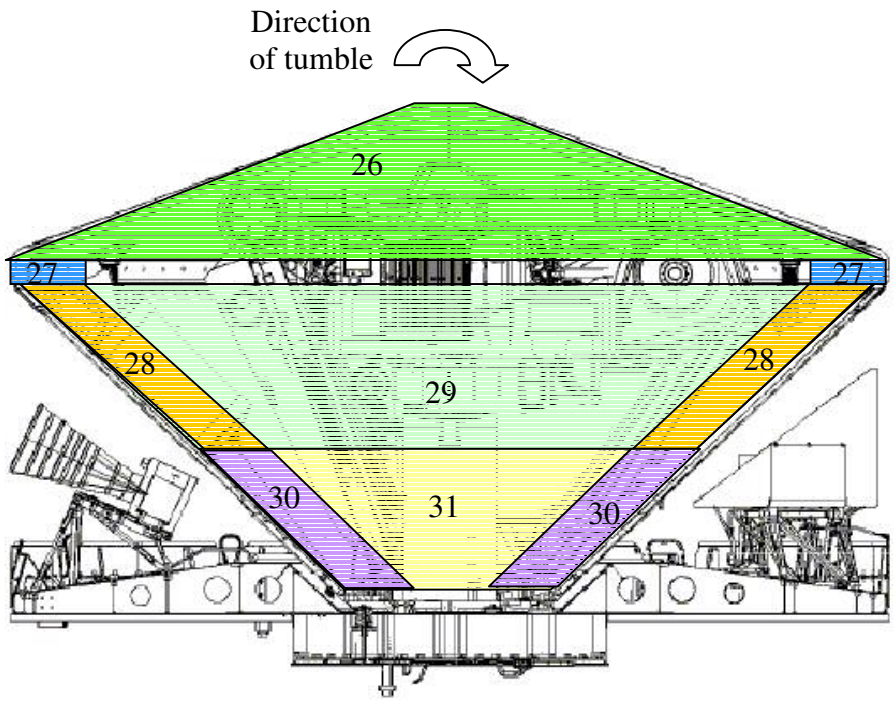
G.6.2 Launch Vehicle and Entry Vehicle Thermal Nodes

In addition to the above twenty-five Cruise Stage thermal nodes [17], the following launch vehicle and entry vehicle thermal nodes listed in Table 17 were identified.

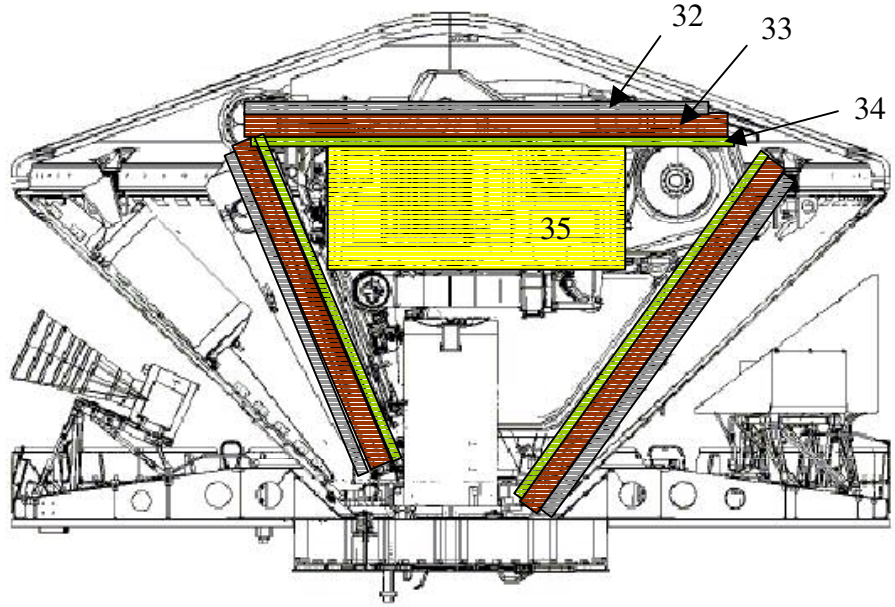
Table 17. Launch Vehicle and Entry Vehicle Thermal Nodes

Node #	Thermal Node	
	Suborbital Reentry	**Out-of-Orbit Reentry**
26	Thermal Protection System (TPS)	Stage III Ti Case
27	H/S Shoulder	LVA2
28	B/S Large End Hot Side	Small Cone
29	B/S Large End All Cone	Nose
30	B/S Small End Hot Side	Shoulder
31	B/S Small End All Cone	LVA
32	Airbags	Airbags
33	Petal Struts	Petal Struts
34	Aerogel	Rover Al Plate
35	Rover Al Plate	-

For a suborbital reentry, the entry vehicle consisted of the Aeroshell, Lander, Rover, and Cruise Stage, and the thermal nodes are defined in Figure 33. Note that the spacecraft is illustrated as tumbling in the clockwise direction where the axis of rotation is out of the paper. Thus, the plane of the paper acts as the plane of symmetry in the definition of the thermal nodes.



(a)



(b)

Figure 33. (a) Aeroshell and (b) Lander and Rover Thermal Nodes in Suborbital Reentry

The entry and launch vehicle thermal nodes in an out-of-orbit entry are shown in Figure 34. The Lander and Rover nodes are not illustrated but are the same as those defined in Figure 33, except with different n

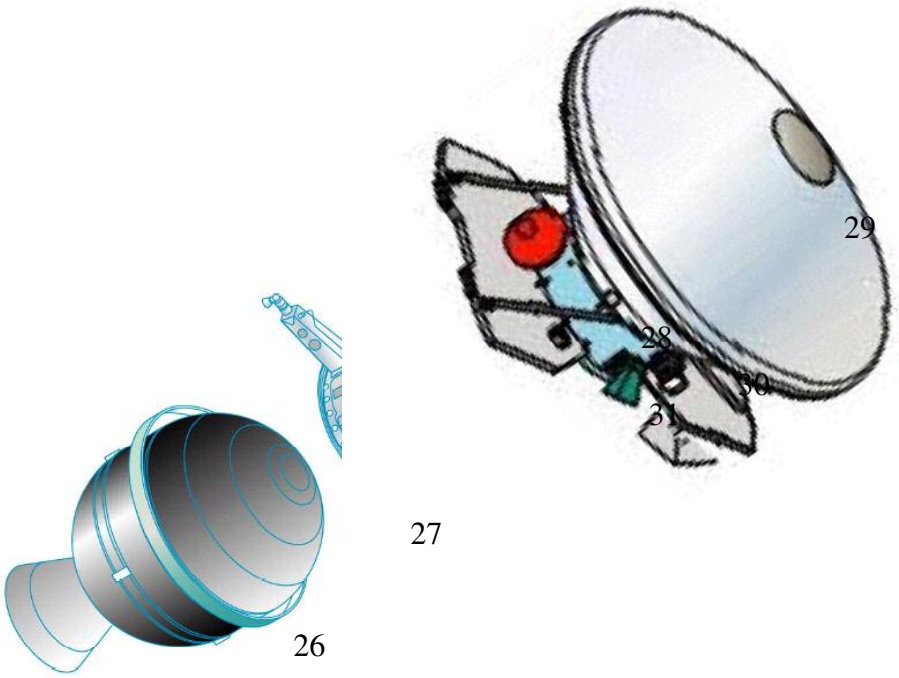


Figure 34. Entry and Launch Vehicle Thermal Nodes in Out-of-Orbit Reentry

G.7 Failure Criteria

Failure criteria were specified in terms of temperature for the Cruise Stage nodes, total integrated reference heating (Q_{ref}) for the launch vehicle and Aeroshell, and delta integrated reference heating (ΔQ_{ref}) for the Lander and Rover nodes. The failure criteria in the form of integrated heating were derived based on the Aeroshell integrated heating load limit provided by Lockheed Martin (LMA) and were dependent on the orientation of the vehicle to the flow. The failure criteria are given in the following subsections. Note that in the case of a steep entry, a g-load failure criterion of 30 gees with no heating was also considered [59].

G.7.1 Failure Criteria for Cruise Stage Nodes

The failure temperatures for the twenty-five Cruise Stage nodes were set to the melting temperatures of the materials and were applicable to both MER-A and MER-B. The failure temperatures were applicable for both suborbital and out-of-orbit reentries. For a Cruise Stage node, the temperatures for the node modeled as poor and good conductors were calculated. For node failure assessment, the average of these two temperatures was compared with the node failure temperature.

The following conditions were also imposed in the failure assessment of the Cruise Stage nodes:

1. If Node 1 (Cluster strut) failed, Node 22 (Thruster cluster) also failed.
2. If Node 2 (Star scanner strut) failed, Node 6 (Star scanner cone) also failed.
3. If Node 3 (IPA strut) failed, Nodes 16 (IPA box) and 24 (CSLA box) also failed.
4. If Node 8 (Rib 12) failed, all nodes except for 7 (Intercostal), 9 (Torus), and 11 (LVA) also failed.

G.7.2 Failure Criteria for Aeroshell

The Aeroshell failure criteria were provided by Lockheed Martin (LMA) [60]. The inadvertent Earth entry of the MER Aeroshell as part of launch failure analysis was evaluated. Assumptions for this case were a low circular Earth orbit with the Aeroshell separated from its Cruise Stage. LMA had assessed the inadvertent Earth entry of the MER vehicle in its Mars entry configuration and determined that the Aeroshell failed before reaching the ground, both in the Heatshield-leading and Backshell-leading orientations.

G.7.3 Failure Criteria for Entry Spacecraft

In a suborbital reentry, the entry vehicle was assumed to be tumbling due to uneven, asymmetric forces from the shaped charges. The failure criteria for the entry spacecraft were derived based on the physical and thermal properties of the nodes [61-63]. The failure integrated heating for the entry vehicle thermal nodes in a suborbital reentry are given in Table 18 and were applicable to both MER-A and MER-B. Note that launch vehicle nodes did not exist in suborbital reentries due to the activation of the FTS. It was assumed that if the B/S small end all cone failed, then the entire Aeroshell would be separated from the Lander/Rover.

Table 18. Failure Integrated Heating for Entry Vehicle in Suborbital Reentry

Thermal Node	Failure Q_{ref} (J/cm^2)
TPS	36588
H/S Shoulder	11156
B/S large end hot side	14844
B/S large end all cone	11156
B/S small end hot side	5578
B/S small end all cone	11156
Airbags	Δ = 1129
Petal struts	Δ = 123
Aerogel	Δ = 279
Rover Al plate	Δ = 96

In an out-of-orbit reentry, the entry spacecraft was assumed to be spinning at a fixed angle-of-attack. The angle-of-attack dependent failure integrated heating are given in Table 19 and were applicable to both MER-A and MER-B. Note that for thermal nodes not applicable in the expected sequence of failure, the failure criteria were not derived.

Table 19. Failure Integrated Heating for Entry and Launch Vehicles in Out-of-Orbit Reentry

Thermal Node	Failure Q_{ref} (J/cm^2)	Failure Q_{ref} (J/cm^2)	Failure Q_{ref} (J/cm^2)
	$\alpha = 0°$	$\alpha = 90°$	$\alpha = 180°$
Stage III Ti Case	N/A	1607	N/A
LVA2	N/A	2867	N/A
Small cone	N/A	4522	2011
Nose	9147	N/A	N/A
Shoulder	10724	N/A	N/A
LVA	N/A	N/A	4000
Airbags	$\Delta = 1130$	$\Delta = 4000$	$\Delta = 5000$
Petal struts	$\Delta = 123$	$\Delta = 400$	$\Delta = 6000$
Al Plate	$\Delta = 375$ (bottom plate)	$\Delta = 1000$ (side plate)	$\Delta = 500$ (top plate)

G.8 Exposure Factors

Exposure factors were applicable only to Cruise Stage thermal nodes since the failure analysis was based on temperature and not integrated heating. After a node failure had been verified, the exposure factor for the failed node became 0. For entry vehicle thermal nodes, the exposure factors were absorbed into the derived, angle-of-attack dependent failure integrated heating.

G.8.1 Suborbital Reentry Exposure Factors

The spacecraft was assumed to be tumbling in a suborbital reentry. Therefore, only one set of exposure factors was used for all suborbital reentries. The exposure factors were updated once, when the solar array substrate, or Node 10, failed. The solar array substrate partially shielded many Cruise Stage thermal nodes from exposure to the

flow, and its failure significantly increased the exposure of these nodes to the flow. The exposure factors are given in Table 20 and were applicable to both MER-A and MER-B.

Table 20. Exposure Factors for Suborbital Reentries

Node #	At t = 0 sec	After Failure of Node 10
1 – 9, 12 – 25	0.25	0.75
10	0.5	0.0
11	0.5	0.75

G.8.2 Out-of-Orbit Reentry Exposure Factors

The exposure factors for the Cruise Stage nodes in an out-of-orbit reentry were dependent on the entry angle-of-attack. The exposure factors are given in Table 21 and were applicable to both MER-A and MER-B.

Table21 . Exposure Factors for Out-of-Orbit Reentries

	α = 0°		α = 90°		α = 180°	
Node #	t = 0 sec	After Failure of Node 10	t = 0 sec	After Failure of Node 12	t = 0 sec	After Failure of Node 10
1, 6, 18 - 22	0.25	0.25	0.32	1/π	0.14	0.9
2 – 4, 7 – 8, 13 – 15, 17, 23, 25	0.25	0.25	0.06	1/π	0.0	0.9
5	0.25	0.25	0.31	1/π	0.14	0.43
9, 11	0.0	0.1	0.06	1/π	0.0	0.9
10	0.25	0.0	0.06	1/π	0.9	0.0
12	0.25	0.25	0.31	0.0	0.14	0.43
16, 24	0.25	0.25	0.32	1/π	0.0	0.9

G.9 Expected Sequence of Failures and Vehicle Properties Updates

During the reentry, vehicle breakup caused the vehicle configuration to change and vehicle properties such as vehicle mass (m), C_D, and A_{ref} were updated accordingly. The expected sequence of failures for the reentry scenarios were developed to obtain the various vehicle configurations, and vehicle properties for these configurations were determined. In a suborbital reentry, the vehicle was assumed to be tumbling and only one expected sequence of failures was considered. The expected sequence of failures in a suborbital reentry and the vehicle properties updates including the ballistic coefficient (C_B) are listed in Table 22.

Table 22. Expected Sequence of Failures and Vehicle Properties Updates in Suborbital Reentry

Event	Mass (kg)		C_D	A_{ref} (m^2)	C_B (kg/m^2)	
	MER-A	MER-B			MER-A	MER-B
At t = 0 sec	1127	1131.511	1.11	5.5	184.6	185.34
Failure of Node 10	932 kg subtract masses of other nodes which failed before Node 10 failure	936.511 kg subtract masses of other nodes which failed before Node 10 failure	1.11	5.5	depend on updated mass	depend on updated mass
Failure of entire CS & Aeroshell	762	766.511	1.11	2.01	341.54	343.56
Failure of airbags & petals	180	184.511	1.25	0.5	288	295.22
Failure of aerogel & Al plate, free RHU	0.04	0.04	1.333	8.32×10^{-4}	36.07	36.07

For out-of-orbit reentries, the mass of the entry vehicle depended on the type of reentry. For example, for delayed elliptic and COD, the spacecraft had separated from Stage III.

For powered entry, the vehicle consisted of the spacecraft with Stage III, and perhaps also Stage II, depending on the time of entry. The vehicle would be thrusting, or the reentry could occur during coast and Stage III would ignite post-entry. The entry masses for COD and delayed reentries were 1077.01 kg for MER-A and 1081.511 for MER-B. The entry mass for powered entries was dependent on the entry time. The vehicle mass was updated by subtracting the masses of failed nodes. The node masses are given in Table 23.

Table 23. Node Masses for Updates

Component	Mass (kg)	
	MER-A	**MER-B**
CS (less LVA)	201.6	206.111
LVA	33.5	33.5
Stage II Fuel	1615.1	1615.1
Empty Stage II	1146.8	1146.8
Stage III Fuel	2018.9	2018.9
Empty Stage III Ti Case	164.6	164.6
LVA2	50	50
Nose (H/S less shoulder)	80	80
Cone (B/S less shoulder)	197.5	197.5
Shoulder	10	10
Airbags	111.1	111.1
Petals	263.2	263.2
Rover	180.1	180.1
RHU	0.04	0.04
Total	6072.4	6072.4

The expected sequence of failures was dependent on the vehicle orientation to the flow. The expected sequence of failures and the vehicle properties updates in an out-of-orbit

reentry at entry angle-of-attack of 0º, 90º, and 180º are given in Table 24, Table 25, and Table 26, respectively, and were applicable to both MER-A and MER-B.

Table 24. Expected Sequence of Failures and Vehicle Properties Updates in Out-of-Orbit Reentry at Entry Angle-of-Attack of 0º

Event	C_D	A_{ref} (m^2)
At t = 0 sec	1.65	5.52
Failure of CS nodes	1.65	5.52
Failure of Nose	1.65	5.52
Failure of Shoulder	1.65	5.52
Failure of Airbags	1.65	5.52
Failure of Petals	1.65	5.52
Failure of Rover bottom plate, free RHU	1.333	8.32×10^{-4}

Table 25. Expected Sequence of Failures and Vehicle Properties Updates in Out-of-Orbit Reentry at Entry Angle-of-Attack of 90º

Event	C_D	A_{ref} (m^2)
At t = 0 sec	1.25	3.92
Failure of CS Node 12	1.25	3.92
Failure of rest of CS nodes and Stage III Ti Casing (stops thrust)	1.25	2.5
Failure of LVA2	1.25	2.5
Failure of Small cone (lose Aeroshell)	1.25	1.59
Failure of Airbags, side on	1.25	1.59
Failure of Petals, side on	2.0	0.59
Failure of Rover side plate, free RHU	1.333	8.32×10^{-4}

Table 26. Expected Sequence of Failures and Vehicle Properties Updates in Out-of-Orbit Reentry at Entry Angle-of-Attack of 180°

Event	C_D	A_{ref} (m^2)
At t = 0 sec	1.04	5.52
Failure of CS Node 10	1.04	5.52
Failure of rest of CS nodes	1.04	5.52
Failure of small cone (lose Aeroshell)	1.7	1.82
Failure of LVA	1.7	1.82
Failure of Airbags, side on	1.7	1.17
Failure of Petals, side on	2.0	0.59
Failure of Rover top plate, free RHU	1.333	8.32×10^{-4}

Appendix H. References

1. "Atomic Power in Space, A History", U.S. Department of Energy, DOE/NE/32117-H1, March 1987.
2. Connor, J. Jr., "Aerospace Nuclear Safety", Aerospace Med., Volume 31, pp. 797-806, January 1, 1960.
3. Fink, C., "Snap 9A: Significant Development Factors and Launch Approval", 3rd Biennial Aerospace Power Systems Conference, September 1-4, 1964.
4. Sholtis, J. Jr., and Winchester, R., "Nuclear-Powered Space Missions: Obtaining Launch Approval", AIAA-92-3698, 28th Joint Propulsion Conference and Exhibit, July 6-8, 1992.
5. Lucero, E. F., "Overview of Technical Challenges of Reentry Analysis of Radioisotope Heat Sources", AIAA 93-0379, 31st Aerospace Sciences Meeting & Exhibit, Reno, NV, January 11-14, 1993.
6. Rosko, R. and Loughin, S., "Safety Evaluation of RTG Launches Aboard Titan IV Launch Vehicles", AIP Conference Proceedings, Volume 387, Issue 1, pp. 1475-1480, January 26-30, 1997.
7. Reimus, M.; Rinehart, G.; Herrera, A.; Lopez, B.; Lynch, C.; and Moniz, P.; "Light-Weight Radioisotope Heater Unit (LWRHU) Impact Tests", AIP Conference Proceedings, Volume 420, Issue 1, pp. 1329-1337, January 15, 1998.
8. Fritsche, B.; Roberts, T.; Romay, M.; Ivanov, M.; Grinberg, E.; and Klinkrad, H.; "Spacecraft Disintegration During Uncontrolled Atmospheric Re-entry", IAA 99-6.7.02, Space Debris Conference, February, 1998.

9. Yau, M.; Reinhart, L.; Guarro, S.; "Launch Vehicle Accident Assessment for Mars Exploration Rover Missions", Proceedings of the 6th International Conference on Probabilistic Safety Assessment and Management (PSAM-6), San Juan, Puerto Rico, June 23-28, 2002.
10. "Orbital Reentry Breakup Analysis Report, P74-1 Payload System", Report D00604, TRW Systems Group, Redondo Beach, California, November 9, 1973.
11. "General Purpose Heat Source Radioisotope Thermoelectric Generator (GPHS-RTG) Final Design Review Data Package", General Electric Co., Space Systems Division, October 10, 1980.
12. Hemler, R., Kelly, C., and Braun, J., "Flight Performance of Galileo and Ulysses RTGs", AIP Conference Proceedings 246, Part One, pp. 171-176, Space Nuclear Power Systems Ninth Symposium, Albuquerque, NM 1992.
13. Matteo, D., Kugler, W., Kull, R., Bond, J., "Recent Achievements in Conductively Coupled Thermoelectric Cell Technology for the SP-100 Program", AIP Conference Proceedings 246, Part One, pp. 343-352, Space Nuclear Power Systems Ninth Symposium, Albuquerque, NM 1992.
14. Jaffe, P., McRonald, A., et al., "MJS Breakup Analysis", JPL Document 618-427, August 1976.
15. Jaffe, P., McRonald, A., et al., "Galileo & Ulysses Breakup Analysis: Powered Entry of Upper Stage Plus Spacecraft", JPL D-4660, January 1988.
16. McRonald, A., "V-Gamma Map for the Mars MER-A Launch", JPL IOM 312.01/E-3, February 26, 2001.

17. McRonald, A., "Entry of the Mars 03 Cruise Stage into Mars", JPL IOM 312/01.E-007, August 10, 2001.

18. McRonald, A., "Accidental Earth Reentry of the SIRTF Spacecraft", JPL IOM 312/01.E-006, May 18, 2001.

19. Salama, A., "Section 9.5 of the NH SAR Databook", September 2004.

20. Jaffe, P. et al, "Ulysses Breakup Analysis Final Report", JPL Document 1628-54, November 1984.

21. McRonald, A., "Release Conditions of the Two RTG's, Breakup Case 1: Steep Angle Entry of the Deployed Galileo Spacecraft", to L. T. Shaw, JPL IOM 3547-GLL-81-570, October 12, 1981.

22. McRonald, A., "Release Conditions of the Two RTG's, Galileo Breakup Case 2: Shallow Angle Entry of the Deployed Spacecraft", to L. T. Shaw, JPL IOM 3547-GLL-82-102, July 1, 1982.

23. McRonald, A., "Review of the Heat Source Module Release Conditions, Galileo Entry Breakup Cases 1 and 2", to L. T. Shaw, JPL IOM 3547-GLL-82-180, November 22, 1982.

24. McRonald, A., "Dynamic Motion of the Inboard Fuel Module Half-Stack Emerging from the RTG Case, Galileo Entry Breakup Cases 1 and 2", to L. T. Shaw, JPL IOM 3547-GLL-82-187, December 21, 1982.

25. McRonald, A., "Galileo Breakup Analysis Case 3 Release Conditions of the RTG Fuel Modules: Orbit Decay of the Cruise Spacecraft", to L. T. Shaw, JPL IOM 3547-GLL-83-018, March 7, 1983.

26. McRonald, A. and Jaffe, P., "Case 4 Powered Entry Breakup Analysis for Galileo and ISPM", to INSRP Committee, October 31, 1983.
27. McRonald, A., "Release Conditions of the LW RHU's Galileo Breakup Analysis", to L. T. Shaw, JPL IOM 3547-GLL-83-121, November 8, 1983.
28. Anderson, D. M., "Galileo Reentry Breakup, Stress Analysis: Case 1: Steep Angle Reentry of the Deployed Spacecraft", to A. D. McRonald, JPL IOM 354:81:1103, November 1981.
29. Ling, L., "Vehicle Breakup Analysis (VBA) Software Concept of Operations", Version 1.0, November 11, 2002.
30. Striepe, S., Powell, R., Desai, P., and Queen, E., "Utilization Manual for Program To Optimize Simulated Trajectories (POSTII)", Volume II, Version 1.1.6.G, NASA Langley Research Center, January 2004.
31. "User's Guide for AEPL", V4.15, Jet Propulsion Laboratory, September 2, 2003.
32. http://www.sinda.com
33. Cheatwood, F. and Gnoffo, P., "User's Manual for the Langley Aerothermodynamic Upwind Relaxation Algorithm (LAURA)", NASA Technical Memorandum 4674, Langley Research Center, April, 1996.
34. http://www.mscsoftware.com
35. http://www.ansys.com/
36. Grogan, R. and Laskin, R., "On Multidisciplinary Modeling of the Space Interferometry Mission", http://techreports.jpl.nasa.gov/1998/98-0407.pdf, Jet Propulsion Laboratory, 1998.

37. Kan, J., "Simulation of Aeroassisted Maneuvers in the Martian Atmosphere", Engineer's Thesis, Naval Postgraduate School, Monterey, CA, September 1999.
38. http://www.boeing.com/defense-space/space/delta/record.htm
39. Salama, A.; McRonald, A.; Ahmadi, R.; Ling, L.; Accad, E.; Kim, A.; "Application of the V-Gamma Map to Vehicle Breakup Analysis", 2003 Flight Mechanics Symposium at NASA Goddard Space Flight Center, Oct. 28-30, 2003.
40. "NASA Safety Standard – Guidelines and Assessment Procedures for Limiting Orbital Debris", NSS 1740.14, August 1995.
41. Ling, L., "Vehicle Breakup Analysis (VBA) Software Algorithm Description Document (ADD)", Version 1.0, January 24, 2003.
42. http://www.orbitaldebris.jsc.nasa.gov/index.html
43. http://www.arl.noaa.gov/ready.html
44. Regan, F. J., Anandakrishnan, S. M., "Dynamics of Atmospheric Re-Entry", AIAA Education Series, 1993.
45. Etkin, B., "Dynamics of Flight – Stability and Control", 2nd Edition, John Wiley & Sons, 1982.
46. Junkins, J. L., "Lectures on Space Vehicle Orbit and Attitude Dynamics", Texas A&M University, Fall 1987.
47. Ling, L., "Planetary Atmospheric Navigation and Mission Analysis (PANAMA) Algorithm Description Document", Version 1.0, May 31, 2002.
48. Murry, C. and Dermott, S., "Solar System Dynamics", Cambridge University Press, 1999.

49. Anderson, John, “Fundamentals of Aerodynamics”, Second Edition, McGraw-Hill, Inc, 1991.
50. Bonner, E., Clever, W., and Dunn, K., “Aerodynamic Preliminary Analysis System II Part I – Theory”, NASA Contractor Report 182076, April 1991.
51. Email from Peter Jaffe on August 19, 2002.
52. Sandia Corporation, “A Compilation of Longitudinal Aerodynamic Characteristics Including Pressure Information for Sharp- and Blunt-Nose Cones Having Flat and Modified Bases”, Sandia Corporation SC-R-64-1311, January 1965.
53. Oberkampf, W.; Aeschliman, D.; Walker, M., “Joint Computational and Experimental Aerodynamics Research on a Hypersonic Vehicle”, AGARD Symposium on Theoretical and Experimental Methods in Hypersonic Flows, Torino, Italy, May 4-8, 1992.
54. Bertin, J., “Hypersonic Aerothermodynamics”, ISBN 1-56347-036-5, AIAA Education Series, 1994.
55. McRonald, A., “Galileo RTG Reentry Breakup Analysis”, JPL D-1876, September 1984
56. “CEF_Template_020213.xls” Landing Stats Spreadsheet, Developed by John Michel, Provided by Phil Knocke.
57. “Mars Exploration Rover Project – 2003, Launch and Trajectory Information”, MER2003 SAR CD, December 20, 2002.
58. “MER – 2003 DTO Memo Files, For Planning Purposes Only”, MER2003 DTO Info CD, April 25, 2003.

59. Lee, D., Landry, C., Chen, L., "Mars Exploration Rover Spacecraft", JPL Mars Exploration Rover Structural Verification Review, March 21, 2003.

60. Willcockson, B., "MER Suborbital Failure.doc", Email attachment to Ahmed Salama, Subject: MER Inadvertent Earth Entry, July 10, 2003.

61. McRonald, A., "Accidental Earth Reentry of the MER-03 Lander; Release of RHUss", JPL Interoffice Memorandum 312.01.E-011, May 10, 2002.

62. McRonald, A., "Powered Earth Reentry of the MER-03 Spacecraft plus Stage III: Release of RHUs", JPL Interoffice Memorandum 312.01.E-013, May 10, 2002.

63. Sokolowski, W., "Physical & Thermal Data for Breakup Analysis", JPL Section 353, May 2003.

64. Thesinger, P., and Rutger, L., "Mars Exploration Rover – 2003 Mission Debris Impact Footprint Definition Plan For Suborbital And Orbital Reentry Contingencies", May 13, 2003.

65. Salama, A., Ling, L., McRonald, A., "Mars Exploration Rover (MER) Pre-Launch Vehicle Breakup Analysis", Aug. 27, 2003.

66. Email from Ahmed Salama to Lisa Ling, June 3, 2003.

67. http://mars7.jpl.nasa.gov/mro/spotlight/20050412.html

68. Perminov, V. G., "The Difficult Road to Mars, A Brief History of Mars Exploration in the Soviet Union", A Joint Publication of the NASA History Division Office of Policy and Plans and Office of Space Science, Monographs in Aerospace History, Number 15, NP-1999-06-251-HQ, July 1999.

69. http://mars.jpl.nasa.gov/mgs/msss/camera/images/12_99_MPLsearch/index.html

70. http://www.beagle2.com/index.htm

71. Burdick, A., “Seeding the Universe”, Discover Magazine, Vol. 25, No. 10, p. 57, October, 2004.

72. http://www.aero.org/capabilities/cords/index.html

73. http://www.cnn.com/SPECIALS/2001/mir/space.debris.html

74. http://history.nasa.gov/SP-4208/ch19.htm#t3

75. http://www.esa.int/SPECIALS/ESOC/SEMU2CW4QWD_0.html

76. http://www.jaxa.jp/missions/projects/engineering/space/debris/index_e.html

Appendix I. Acronyms

AEPL	Atmospheric-Entry, Powered-Landing simulator
AIC	Accident Initial Conditions
AL	Air Lit
ANSE	Aerospace Nuclear Safety Engineer
AOC	Accident Outcome Condition
ARL	Air Resources Laboratory
B/S	Backshell
CDS	Command Destruct System
CEM	Cruise Electronics Module
CFD	Computational Fluid Dynamics
c.g.	Center of Gravity
COD	Circular Orbit Decay
CORDS	Center for Orbital and Reentry Debris Studies
CS	Cruise Stage
CSLA	Cruise Shunt Limiter Assembly
DAS	Debris Assessment Software
DEL	Orbit Decay Reentry
DOF	Degree Of Freedom
DTO	Detailed Test Objectives
ECI	Earth-Centered Inertial
EDL	Entry, Descent, and Landing
EI	Entry Interface

EIS	Environmental Impact Statement
ELD	Delayed Reentry
ELP	Prompt Reentry
ESA	European Space Agency
ESOC	European Space Operations Centre
Fglass/E	Fiberglass / Epoxy
FS	Facesheet
FTS	Flight Termination System
GE	Graphite Epoxy
GEM	Graphite Epoxy Motors
GL	Ground Lit
GPHS	General Purpose Heat Source
GSFC	Goddard Space Flight Center
HES	Hyperbolic Escape
HP	Prompt Hyperbolic Reentry
HRS	Heat Rejection System
H/S	Heatshield
IAA	International Academy of Astronautics
IMOS	Integrated Modeling of Optical Systems
INSRP	Interagency Nuclear Safety Review Panel
IOM	InterOffice Memorandum
IPA	Integrated Pump Assembly
JAXA	Japan Aerospace Exploration Agency

JIMO	Jupiter Icy Moons Orbiter
JPL	Jet Propulsion Laboratory
LAURA	Langley Aerothermodynamic Upwind Relaxation Algorithm
LEM	Lunar Excursion Module
LMA	Lockheed Martin
LRE	Liquid Rocket Engine
LVA	Launch Vehicle Adapter
LWRHU	Light Weight Radioisotope Heater Unit
MECO	Main Engine Cutoff
MER	Mars Exploration Rover
MSL	Mars Science Laboratory
NASA	National Aeronautics and Space Administration
NASTRAN	NASA Structural Analysis computer program
NOAA	National Oceanic and Atmospheric Administration
NPS	Nuclear Power System
ORSAT	Object Reentry Survival Analysis Tool
PAF	Payload Attach Fitting
PDM	Propellant Distribution Module
PLF	Payload Fairing
POST	Program to Optimize Simulated Trajectories
PWE	Powered Reentry
REN	Radial, East, North
RTG	Radioisotope Thermoelectric Generator

SAR	Safety Analysis Report
SECO	Second Stage Engine Cutoff
SINDA/G	Systems Improved Numerical Differencing Analyzer/Gaski
SMB	Steady Misaligned Burn
S/S	Stainless Steel
SSE	Sun Sensor Electronics
TPS	Thermal Protection System

Appendix J. Symbols

a	Semi-major axis
A_{flow}	Surface area normal to flow
Al	Aluminum
A_{ref}	Reference area
α	Angle-of-attack
α_a	Angle-of-attack of the spacecraft relative to the aerodynamic velocity
β	Sideslip angle
β_a	Sideslip angle of the spacecraft relative to the aerodynamic velocity
c	Specific heat
C_a^b	Matrix to transform from a-frame to b-frame
C_B	Ballistic coefficient
C_{corr}	Correlation coefficient
C_D	Drag coefficient
C_L	Lift coefficient
C_l	Rolling moment coefficient
C_m	Pitching moment coefficient
C_n	Yawing moment coefficient
C_n^R	Matrix to transform from navigation frame to rotating frame
C_o^I	Matrix to transform from orbit-plane frame to inertial frame
C_R^I	Matrix to transform from rotating frame to inertial frame

C_v^b	Matrix to transform from velocity frame to body frame
C_v^I	Matrix to transform from velocity frame to inertial frame
C_v^n	Matrix to transform from velocity frame to navigation frame
c.g.	Center of Gravity
Cu	Copper
D	Drag force
d	Component thickness
$\Delta Q_{fail_B/S}$	Failure integrated heating for backshell
$\Delta Q_{fail_H/S}$	Failure integrated heating for heatshield
$\Delta Q_{fail_shoulder}$	Failure integrated heating for aeroshell shoulder
ΔQ_{heatup}	Heating to reach the melting point from room temperature
ΔQ_{melt}	Integrated heating to melt component
$\Delta\theta$	Longitude with respect to rotating frame x-axis (which is not necessarily the Greenwich meridian)
ΔT	Rise in temperature
δ	Bank angle
δ_a	Bank angle of the spacecraft relative to the aerodynamic velocity
e	Eccentricity
$\hat{e}_x^b,\ \hat{e}_y^b,\ \hat{e}_z^b$	Body frame unit vectors
$\hat{e}_x^G$	Earth-centered unit vector in the inertial x-y plane and through the Greenwich meridian

$\hat{e}_x^I,\ \hat{e}_y^I,\ \hat{e}_z^I$	Inertial frame unit vectors
$\hat{e}_x^m$	Earth-centered unit vector in the inertial x-y plane and through the local meridian of the spacecraft
$\hat{e}_r^n,\ \hat{e}_\theta^n,\ \hat{e}_\phi^n$	Navigation frame unit vectors
$\hat{e}_x^R,\ \hat{e}_y^R,\ \hat{e}_z^R$	Rotating frame unit vectors
$\hat{e}_x^v,\ \hat{e}_y^v,\ \hat{e}_z^v$	Velocity frame unit vectors
ε	Emissivity
f	True Anomaly
$\vec{F}_{aero}^{\,v}$	Aerodynamic force vector in velocity frame coordinates
$\vec{F}_{grav}^{\,v}$	Gravitational force vector in velocity frame coordinates
F_{thrust}	Thrust force
$\vec{F}_{thrust}^{\,v}$	Thrust force vector in velocity frame coordinates
ϕ	Latitude
$\overline{\phi}$	Mean latitude
$\dot{\phi}$	Rate of change of latitude
g_{Earth}	Earth's gravitational acceleration
γ_I	Inertial flight path angle
γ_R	Air-relative flight path angle
$\dot{\gamma}_R$	Rate of change of air-relative flight path angle
H	Angular momentum

He	Helium
h_{fg}	Enthalpy of vaporization
$\underline{\underline{I}}$	Moment of inertia tensor
i	Inclination
Isp	Engine specific impulse
J_2	2nd-order harmonic coefficient
J_3	3nd-order harmonic coefficient
L	Lift force
l	Reference length
L/D	Lift-to-Drag ratio
m	Mass
$\dot{m}$	Rate of change of mass due to fuel consumption or ablation
$\vec{M}^{b}_{aero}$	Aerodynamic torque vector in body frame coordinates
μ_E	Gravitational-mass constant for Earth
$\vec{M}^{b}_{thrust}$	Thrust torque vector in body frame coordinates
n	Mean orbit rate
N2H4	Hydrazine
P	Rolling velocity
p	Semi-latus rectum
$\dot{P}$	Roll acceleration
P_{burst}	Tank burst pressure
$P_{operating}$	Tank operating pressure

Q	Pitching velocity
$\dot{Q}$	Pitch acceleration
$q_{burnout}$	Tank burnout flux
Q_{fail}	Failure integrated heating
q_{fail}	Failure heating rate
Q_{nom}	Nominal integrated heating
Q_{ref}	Integrated reference stagnation point heating
q_{ref}	Reference stagnation point convective heating
Θ	Celestial longitude measured from inertial frame
θ	Terrestrial longitude measured from the Greenwich meridian
$\dot{\theta}$	Rate of change of longitude
θ_0	Initial terrestrial longitude at trajectory initiation (constant value)
R	Yawing velocity
r	Spacecraft position radius
$\dot{R}$	Yaw acceleration
$\dot{r}$	Rate of change of spacecraft position radius
$\vec{r}^{\,n}$	Spacecraft position vector in navigation frame coordinates
R_c	Radius of cylinder
Re	Reynolds number
$\dot{\vec{r}}_I^{\,n}$	Inertial velocity vector in navigation frame coordinates
$\dot{\vec{r}}_I^{\,v}$	Inertial velocity vector in velocity frame coordinates

$\ddot{\vec{r}}_I^{\,v}$	Inertial acceleration vector in velocity frame coordinates
r_{inner}	Inner radius of hollow cylinder
r_{outer}	Outer radius of hollow cylinder
$\dot{\vec{r}}_R^{\,n}$	Air-relative velocity vector in navigation frame coordinates
$\ddot{\vec{r}}_R^{\,n}$	Air-relative acceleration vector in navigation frame coordinates
$\dot{\vec{r}}_R^{\,v}$	Air-relative velocity vector in velocity frame coordinates
$\ddot{\vec{r}}_R^{\,v}$	Air-relative acceleration vector in velocity frame coordinates
R_s	Radius of sphere
ρ	Material density
ρ_l	Density of saturated liquid
ρ_v	Density of saturated vapor
ρ_∞	Freestream atmospheric density
sma	Semi-major axis
smi	Semi-minor axis
σ	Stefan-Boltzman constant = 5.67×10^{-12} W/(cm^2·K^4)
σ_{fg}	Surface tension of liquid-vapor
T	Thrust
t	Time
Ti	Titanium
T_{melt}	Melting temperature
$T_{operating}$	Tank operating temperature

T_{room}	Room temperature
U, V, W	Vehicle inertial velocity vector components in inertial frame
$\vec{v}_{aero}^{\,b}$	Aerodynamic velocity vector in body frame coordinates
$\vec{v}_{aero}^{\,v}$	Aerodynamic velocity vector in velocity frame coordinates
v_I	Inertial velocity
v_R	Air-relative velocity
$\dot{v}_R$	Rate of change of air-relative speed
v_{wind}	Wind speed
$\vec{v}_{wind}^{\,v}$	Wind velocity vector in velocity frame coordinates
Ω	Earth rate of rotation
Ω_{LAN}	Longitude of ascending node
ω_{AOP}	Argument of periapsis
$\vec{\omega}_{b/I}^{\,b}$	Angular velocity of the body frame relative to the inertial frame in body frame coordinates
$\vec{\omega}_{n/R}^{\,n}$	Angular velocity of the navigation frame relative to the rotating frame in navigation frame coordinates
$\vec{\omega}_{R/I}^{\,I}$	Angular velocity of the rotating frame relative to the inertial frame in inertial frame coordinates
$\vec{\omega}_{v/I}^{\,v}$	Angular velocity of the velocity frame relative to the inertial frame in velocity frame coordinates

$\vec{\omega}_{v/R}^{v}$	Angular velocity of the velocity frame relative to the rotating frame in velocity frame coordinates
X, Y, Z	Vehicle position vector components in inertial frame
$\dot{X},\dot{Y},\dot{Z}$	Vehicle inertial velocity vector components in inertial frame
$\vec{x}_{a}^{b}$	Vector x observed in a-frame and expressed in b-frame coordinates
ψ_I	Inertial azimuth angle
ψ_R	Air-relative azimuth angle
$\dot{\psi}_R$	Rate of change of air-relative azimuth